NAVAL POSTGRADUATE SCHOOL

MONTEREY, CALIFORNIA

THESIS

A NEW HIGH-RESOLUTION DIRECTION FINDING ARCHITECTURE USING PHOTONICS AND NEURAL NETWORK SIGNAL PROCESSING FOR MINIATURE AIR VEHICLE APPLICATIONS

by

Robert Humeur

September 2015

Thesis Advisor:	Phillip E. Pace
Second Reader:	Steven J. Iatrou

Approved for public release; distribution is unlimited

THIS PAGE INTENTIONALLY LEFT BLANK

REPORT DOCUMENTATION PAGE		*Form Approved OMB No. 0704–0188*

Public reporting burden for this collection of information is estimated to average 1 hour per response, including the time for reviewing instruction, searching existing data sources, gathering and maintaining the data needed, and completing and reviewing the collection of information. Send comments regarding this burden estimate or any other aspect of this collection of information, including suggestions for reducing this burden, to Washington headquarters Services, Directorate for Information Operations and Reports, 1215 Jefferson Davis Highway, Suite 1204, Arlington, VA 22202-4302, and to the Office of Management and Budget, Paperwork Reduction Project (0704-0188) Washington, DC 20503.

1. AGENCY USE ONLY *(Leave blank)*	**2. REPORT DATE** September 2015	**3. REPORT TYPE AND DATES COVERED** Master's thesis	
4. TITLE AND SUBTITLE A NEW HIGH-RESOLUTION DIRECTION FINDING ARCHITECTURE USING PHOTONICS AND NEURAL NETWORK SIGNAL PROCESSING FOR MINIATURE AIR VEHICLE APPLICATIONS		**5. FUNDING NUMBERS**	
6. AUTHOR(S) Robert Humeur			
7. PERFORMING ORGANIZATION NAME(S) AND ADDRESS(ES) Naval Postgraduate School, Center for Joint Services Electronic Warfare Monterey, CA 93943-5000		**8. PERFORMING ORGANIZATION REPORT NUMBER**	
9. SPONSORING /MONITORING AGENCY NAME(S) AND ADDRESS(ES) Consortium for Robotics and Unmanned Systems Education and Research (CRUSER)		**10. SPONSORING / MONITORING AGENCY REPORT NUMBER**	

11. SUPPLEMENTARY NOTES The views expressed in this thesis are those of the author and do not reflect the official policy or position of the Department of Defense or the U.S. Government. IRB Protocol number ____N/A____.

12a. DISTRIBUTION / AVAILABILITY STATEMENT Approved for public release; distribution is unlimited	**12b. DISTRIBUTION CODE**

13. ABSTRACT (maximum 200 words)

This paper investigates the design of an interferometric direction finding receiver using photonic components for signal mixing and a multi-layer perceptron for data analysis. The complete system was tested with a 2.4 GHz continuous signal in an anechoic chamber. Test results showed that the compact antenna and receiver design was capable of measuring direction of arrival with 1° resolution over a 180° field of view while keeping mean error below 0.5°. It was also demonstrated that the design is insensitive to phase alignment of receiver channels, thus simplifying future receiver design. Improvements were recommended for a design theoretically capable of providing 0.25° angle resolution.

14. SUBJECT TERMS direction finding, DF, artificial neural network, ANN, multi-layer perceptron, MLP, photonics, modulator, MZM, Mach-Zehnder, direction of arrival, DOA			**15. NUMBER OF PAGES** 155
			16. PRICE CODE
17. SECURITY CLASSIFICATION OF REPORT Unclassified	**18. SECURITY CLASSIFICATION OF THIS PAGE** Unclassified	**19. SECURITY CLASSIFICATION OF ABSTRACT** Unclassified	**20. LIMITATION OF ABSTRACT** UU

NSN 7540–01-280-5500

Standard Form 298 (Rev. 2–89)
Prescribed by ANSI Std. 239–18

THIS PAGE INTENTIONALLY LEFT BLANK

A NEW HIGH-RESOLUTION DIRECTION FINDING ARCHITECTURE USING PHOTONICS AND NEURAL NETWORK SIGNAL PROCESSING FOR MINIATURE AIR VEHICLE APPLICATIONS

Robert Humeur
Captain, Swedish Army
B.S., Swedish National Defense College, 2013

Submitted in partial fulfillment of the
requirements for the degree of

**MASTER OF SCIENCE IN INFORMATION WARFARE
SYSTEMS ENGINEERING**

from the

**NAVAL POSTGRADUATE SCHOOL
September 2015**

Approved by: Phillip E. Pace
                 Thesis Advisor

                 Steven J. Iatrou
                 Second Reader

                 Dan C. Boger
                 Chair, Department of Information Sciences

THIS PAGE INTENTIONALLY LEFT BLANK

ABSTRACT

This paper investigates the design of an interferometric direction finding receiver using photonic components for signal mixing and a multi-layer perceptron for data analysis. The complete system was tested with a 2.4 GHz continuous signal in an anechoic chamber. Test results showed that the compact antenna and receiver design was capable of measuring direction of arrival with 1° resolution over a 180° field of view while keeping mean error below 0.5°. It was also demonstrated that the design is insensitive to phase alignment of receiver channels, thus simplifying future receiver design. Improvements were recommended for a design theoretically capable of providing 0.25° angle resolution.

THIS PAGE INTENTIONALLY LEFT BLANK

TABLE OF CONTENTS

THIS PAGE INTENTIONALLY LEFT BLANK

LIST OF FIGURES

xiv

LIST OF TABLES

THIS PAGE INTENTIONALLY LEFT BLANK

LIST OF ACRONYMS AND ABBREVIATIONS

AOA	angle of arrival
COTS	commercial off-the-shelf
cRIO	National Instruments CompactRIO
CW	continuous wave
DC	direct current
DE-MZM	dual-electrode Mach-Zehnder modulator
DF	direction finding
DFB	distributed feedback laser
DOA	direction of arrival
ES	electronic support
ESPRIT	estimation of signal parameters via rotational invariance techniques
EW	electronic warfare
FOV	field of view
FPGA	field-programmable gated array
HF	high frequency
LNA	low-noise amplifier
MLP	multi-layer perceptron
MUSIC	multiple signal classification
MZM	Mach-Zehnder modulator
NPS	Naval Postgraduate School
OSNS	optimum symmetric number system
PCB	printed circuit board
PD	photodetector
PM	polarization maintaining
POI	probability of intercept
RF	radio frequency
RSNS	robust symmetric number system
SNS	symmetric number system
TPM	technical performance measures

THIS PAGE INTENTIONALLY LEFT BLANK

ACKNOWLEDGMENTS

As with all academic work, the results documented in this thesis could never have been achieved by one person. Many have contributed to the final result, but some stand out more than others.

First of all, I would like to thank Professor Phillip E. Pace for your unwavering support throughout the work. Your guidance and insightful comments have been fundamental to the final result, and your continuous enthusiasm for my work has been most inspiring.

I would also like to thank Dr. Thomas W. Tedesso for your initial work on the system design, clearing a path for us who followed in your steps. Many of the insights could only be made due to your previous efforts.

At times, the project seemed impossible and the obstacles insurmountable. When giving up seemed like the only option, Sascha Pauly was always there. Without our discussions and your hard work, I feel there would not have been a thesis like this one. We made it!

Dr. James Calusdian, thank you for your support throughout my thesis work. Your insights, comments, and all your practical aid helped me achieve great results.

Bob Broadston and Paul Buczynski, you were always there to support me, whether it was by supplying components or providing guidance, and I am most grateful for your patience.

There are, however, four that deserve special mention: my wife, Madeleine, and our children, Dora, August, and Bea. You, my wonderful family, have sacrificed a lot during these past two years but always stood by me. Your love and support have come in so many forms and shapes and have always been there. I am so proud of you all and so grateful for our journey together that is our life! Love you always!

THIS PAGE INTENTIONALLY LEFT BLANK

I. INTRODUCTION

A. DIRECTION OF ARRIVAL ESTIMATION TECHNIQUES

Direction finding (DF) methods are used to measure the direction of arrival (DOA) of an incident radio frequency wave and are sometimes referred to as radiolocation systems. They are often used to estimate the geographical direction or true bearing of an emitter and have applications in navigation, targeting, law enforcement, and wildlife management. Other applications include electronic signal intelligence, electronic warfare, signal identification, search & rescue, propagation analysis, and ionospheric research. DF may be accomplished using a separate subsystem that is not involved in the signal acquisition process (tasked DF). Another approach is to perform the DF as part of the signal acquisition process. By today's standards, a high-performance DF array should have high angular (spatial) resolution, wide frequency bandwidth, wide field of view, a minimum number of array elements, and a minimum baseline length.

1. Amplitude

To estimate the DOA, a set of spatially separated signal *amplitude samples* can be collected. An amplitude-comparison monopulse determines the emitter's DOA by comparing the received amplitudes in two or more adjacent receiver channels. Field of view can approach 360° with a DF accuracy of 2°–12° depending on the number of antenna elements used. The accuracy of a wideband (8–18 GHz) circular DF array that uses only amplitude comparison was considered in [1].

Rotating a high gain antenna with a small instantaneous field of view (e.g., 1°–15°) over a total field of view of 360° can also be used to compute the emitter's DOA. These rotating (spinning) DF techniques have good sensitivity over a large bandwidth and have an accuracy <1°.

2. Phase

Linear [2] or circular [3] DF phase interferometry uses phase sampling of the intercepted signal at each spatially distributed array element. The phase difference

between adjacent pairs of antenna elements with baseline spacing greater than a half-wavelength results in a known DOA ambiguity problem. The problem extends from the fact that the phase difference is in the form of a periodic saw-tooth folding waveform as a function of the DOA. Consequently, the DOA estimate from a single baseline phase difference is ambiguous since it corresponds to several DOAs. Typically, a third element is added to the baseline with an inter-element spacing designed to successfully resolve the ambiguity [4].

Considering a direct relationship between the saw-tooth folding waveform a residue number system modulus, the Chinese Remainder Theorem is typically used to solve the congruence equations. Correlation between the theoretical and measured phase differences can also be used to estimate the DOA. For a correlation interferometer, DOA is obtained from the phase measurements for which the correlation is at a maximum [5], [6] Significant improvement in the DOA estimate can be realized using both the phase difference method and the phase difference rate measurements as presented in [7].

Linear or circular phase interferometry techniques have good DF accuracy (0.5°–3°), but are fairly complex to implement since the saw-tooth folding waveform period is a function of frequency. In [8], two identical interferometer arrays consisting of three spiral antennas (short and long baseline) were tested in an anechoic chamber to quantify the sources of phase error. Practical error sources identified include phase slope errors as a result of baseline length or frequency errors, misalignment of the phase center and center of pedestal rotation, and coupling of the signals between receiver channels.

An exact expression for the phase error probability density function for a digital interferometer was reported in [9] and [10]. As the frequency of the emitter changes or the bandwidth becomes wider, more antenna elements and baselines are required for ambiguity resolution. This is because the phase slopes are frequency dependent. Development of a frequency-independent phase comparison interferometer was reported in [11].

In [12], a preprocessing technique based on the optimum symmetrical number system and the robust symmetrical number system was investigated to provide a high

resolution, small baseline array. The spatial filtering operation was reduced into several parallel suboperations (moduli) through this preprocessing technique in order to reduce computational demands. When these different moduli were recombined, a significantly higher spatial resolution was achieved.

3.   Combined Phase and Amplitude

Amplitude information can also be combined with the phase interferometer for a more efficient estimation of the DOA. A DF system consisting of two squinted antennas that function both as a phase interferometer and as an amplitude comparison monopulse system was reported in [13]. By retaining the amplitude information at each antenna element, an extended cost function was developed in [14] that incorporated the measured array amplitude response data by appropriately weighting the square of the baseline phase differences with the antenna gains.

DF high frequency (HF) signals has been of interest for over forty years and present several antenna design problems due to the size of the aperture required. In [15], a wide aperture seven-element antenna array in a V formation (294 m wide) was reported to collect the amplitude and phase measurements of an ionospherically propagated HF sky wave signal (9–15 MHz). The location of the remote transmitter could be estimated at distances up to 1400 km by combining these DOA measurements with the knowledge of the ionosphere.

4.   Probability of Intercept

The phase comparison and amplitude comparison techniques result in a 100% probability of intercept (POI). A rotating DF, however, results in less than a 100% POI. For a rotating DF system intercepting a rotating radar system, the longest intercept range comes from a main beam to main beam intercept. The mean-time-to-intercept for the rotating DF, however, can be many minutes due to the alignment required. The shortest intercept range comes from a side lobe to side lobe intercept. This alignment gives the shortest mean-time-to-intercept and can be less than one second.

5.   **Superresolution**

For single signals, conventional DF techniques can be used and typically involve a linear or circular interferometer to measure the incident wave's phase and/or amplitude at each antenna element. For multiple signals, superresolution DF techniques are often used. These techniques can be broken down into beamforming superresolution (maximum likelihood methods, adaptive angular response, thermal noise algorithm) and eigen-based superresolution (multiple signal classification [MUSIC], Root-MUSIC, estimation of signal parameters via rotational invariance techniques [ESPRIT]). A DF algorithm for multiple wideband signals was developed in [16].

The amplitude and phase measurement system is the method of choice since it is easier to implement and has good resolution capabilities. For the amplitude and phase measurement system, the multiple signal problem is sometimes solved by down-converting the intercepted signal into a small bandwidth where the probability of there being just one emitter present is quite high. These techniques have the drawbacks of being limited in resolution and also requiring a large baseline. Superresolution techniques are computationally complex and can determine DOA with a high degree of accuracy for multiple signals. Drawbacks for superresolution techniques are due mostly to incorrect estimate of the model order (number of signals present) and inaccurate characterization of antenna array response. In addition, the element matching requirement is difficult to realize in a cluttered environment. Coherent signals (multipath) also lead to poor DF results. Also, a matched receiver channel for each antenna is required to support simultaneous sampling. Expensive receivers and the need for their calibration make superresolution methods unattractive for radio frequency (RF) DF with array antennas [17].

6.   **Neural Networks in DOA Estimation**

Recently, various approaches using multi-layer perceptrons (MLP) in DOA estimation have been demonstrated. In [18], the performance of several neural network structures was compared in determining DOA for multiple, simultaneous sources. Many of the recently proposed MLP approaches treat DOA estimation as a regression problem,

but [19] described a classification approach using 64 sectors (5.625° resolution) with an average success rate of 96.85% and in [20], the benefits of applying an MLP compared to using MUSIC or similar correlation techniques was discussed. Several simulations of MLP in DOA scenarios can be found in literature, but very little is written on practical demonstrations.

B.   NEURAL NETWORKS

When dealing with regression problems, several approaches are possible; one simple approach is linear curve fitting. As the regression gets more complicated in terms of dimensions and interrelations between the input parameters, other approaches might be necessary.

Artificial neural networks, or MLP, take their inspiration from the functionality of the human brain. A human brain is constructed from a large number of interconnected neurons operating in parallel. The connections between the neurons are called synapses, and each neuron is connected to about 10^4 other neurons. This intricate network of connections between the neurons is what gives the MLP its computational power.

The processing element in the neuron is the perceptron. A perceptron can have one or many inputs, where each input can come from either the environment through a sensor or from the output of another perceptron. Each of these input connections is given a different weight, and the output is a sum based on these weighted inputs, defining a decision plane in the space of the input vectors. Training of the perceptron is the process of calculating these weights in order to span the decision plane for the neuron and is conducted until the learning factor, the gradient, approaches zero. Generally, additional criteria for training termination are defined, such as maximum number of iterations or a pre-determined error rate. One training iteration is referred to as an epoch [21].

Training can be conducted offline or online. In offline training, all training data are available at the beginning and weight values can be computed in advance. This has the benefit of providing instantaneous predictions with minimal errors. However, having a full training sample available might not be feasible, and in some cases, it might be necessary for the perceptron to learn after each sample. In online training, the instances of

the sample are given one by one, and the perceptron is trained and weights updated after each instance, giving it the ability to make decisions and learn over time. Initial decisions might have large errors, but these will decrease as more samples are processed.

When several perceptrons are interconnected, the resulting network is regarded as a number of layers with a certain number of neurons in each layer. A network with one layer can only solve linear decision problems and is unable to perform nonlinear regression or make nonlinear Boolean decisions, such as exclusive-or. This limitation does not exist for MLP with one or several hidden layers.

In the training of an MLP, the process is similar to training a single perceptron, with the exception that the output now is a non-linear function of the inputs. This causes the error from different layers to backpropagate from the output to the input layer, thus the name backpropagation algorithm.

Outputs from the network can be determined in several ways depending on whether they are used for regression or classification, where softmax is the most common for classification problems. Softmax uses exponentiation and normalization in order to make the weighted output sum for the correct class significantly higher than the others, ideally close to one while others approach zero [21] and the sum of all outputs equals one.

C.   PRINCIPAL CONTRIBUTIONS

Initial work consisted of a thorough investigation of the system used for demonstration in [22] in order to become familiar with system functions and construction. It was discovered that several components were less than optimal for future work, which is why it was decided to completely redesign the system. The added functionality of a receiving antenna array was another driving factor in this decision, since it put new demands on system performance and capabilities.

A receiving antenna array was added to low-noise amplifiers to achieve reasonable signal amplitude for later processing stages. Correct signal amplitude was achieved through adding a voltage controlled attenuator in each signal path. In order to

6

make phase alignment of the channels possible, voltage controlled phase shifters were introduced. The two latter components were carefully characterized in order to determine necessary control considerations for them.

This design used a higher drive voltage for the laser modulator inputs than previous designs, facilitating a higher output signal and thus less need for amplification of signals after passing through photodetectors. Previously used active envelope detectors were replaced with more robust passive detectors, resulting in a more stable system with less complex power supply demands.

The first major contribution in this work is the demonstration of phase and amplitude balancing of a Mach-Zehnder optical modulator used for analog phase interferometry applications. Design considerations for the dual drive electrode signal paths are described and verified by experimental testing.

The second major contribution is the investigation of MLP for DOA estimation in a phase interferometry system and the experimental testing of this system. Performance is experimentally tested and system degradation over time is quantified in order to provide guidance on recalibration intervals and future design considerations.

The third major contribution is the demonstration that an MLP post-processing approach eliminates all necessary phase balancing of the interferometric receiver, yielding substantial benefits in minimizing construction complexity of the receiving front-end.

D.   THESIS OUTLINE

This thesis was initiated as a development of an existing test system. In Chapter II, this previous system is described, and its possibilities and limitations are discussed. In the same chapter, necessary additional capabilities and modifications are proposed. Chapter III discusses the Mach-Zehnder interferometric modulator (MZM), since this component is driving much of the design considerations for the entire system. Another driving factor in the system design is the testing environment, which is described, quantified, and analyzed in Chapter IV. Inputs from previous chapters are used in the

7

theoretical system design performed in Chapter V, and this theoretical design is transformed into a realizable system of physical commercial off-the-shelf (COTS) components in Chapter VI, which contains a detailed description of the design implementation.

Test procedures, data collection, and output data formatting are described in Chapter VII together with system calibration procedures and verification of receiver electrical performance calculations. This chapter also discusses processing of the output data and considerations for the design of system post-processing algorithms.

Results from training of post-processing networks are shown together with system performance test results in Chapter VIII. These results are discussed in Chapter IX together with proposals for some areas of this research where future work is needed.

II. PREVIOUS BENCH TEST DESIGN AND NECESSARY MODIFICATIONS

This chapter provides an overview of the design previously used for bench testing and discusses major necessary system modification based on findings in previous research as well as new discoveries and assumptions.

A. PREVIOUS DESIGN

Experimental testing of a photonic DF array with robust symmetric number system (RSNS) preprocessing was performed by [22] using a configuration as pictured in Figure 1. An HP 83711B signal generator provided a 2.4 GHz CW signal at 6 dBm to the test system. This signal was supplied to each MZM as a reference at one of their dual inputs. The CW signal was also routed through manual phase shifters in order to generate three individual channels with phase shifts emulating those from a real antenna array. These three individually phase shifted signals were supplied to each MZM's second electrode.

Optical input to the three MZMs was generated by a high-power 1550 nm DFB laser and was split and routed to the modulators through a three-way optical fiber splitter. In each MZM, the optical intensity of the laser was modulated by the combination of the reference signal at one electrode and one of the phase shifted signals at the other. Each of the three modulated laser signals was converted back to an electrical signal using indium gallium arsenide (InGaAs) photodetectors (PDs).

Since only the amplitude of the modulation on these three signals was of interest, a direct current (DC) blocking capacitor was used to remove any DC components in the PD output signals. Each of the signals was amplified by two cascaded low-noise amplifiers (LNA) in order to achieve sufficient signal amplitude for the envelope detector to operate properly. The maximum detected envelope output was determined by adjusting the gain of an instrumentation amplifier operating on the output from the previous envelope detector. Outputs from these three amplifiers were connected to a CompactRIO (cRIO) real-time controller and fed through a comparator network implemented on the

field-programmable gated array (FPGA) in the controller. The RSNS-to-binary algorithm converted these inputs to DOA through a look-up table as described by [23].

Figure 1.   Block Diagram of Previous System Design [from 22]
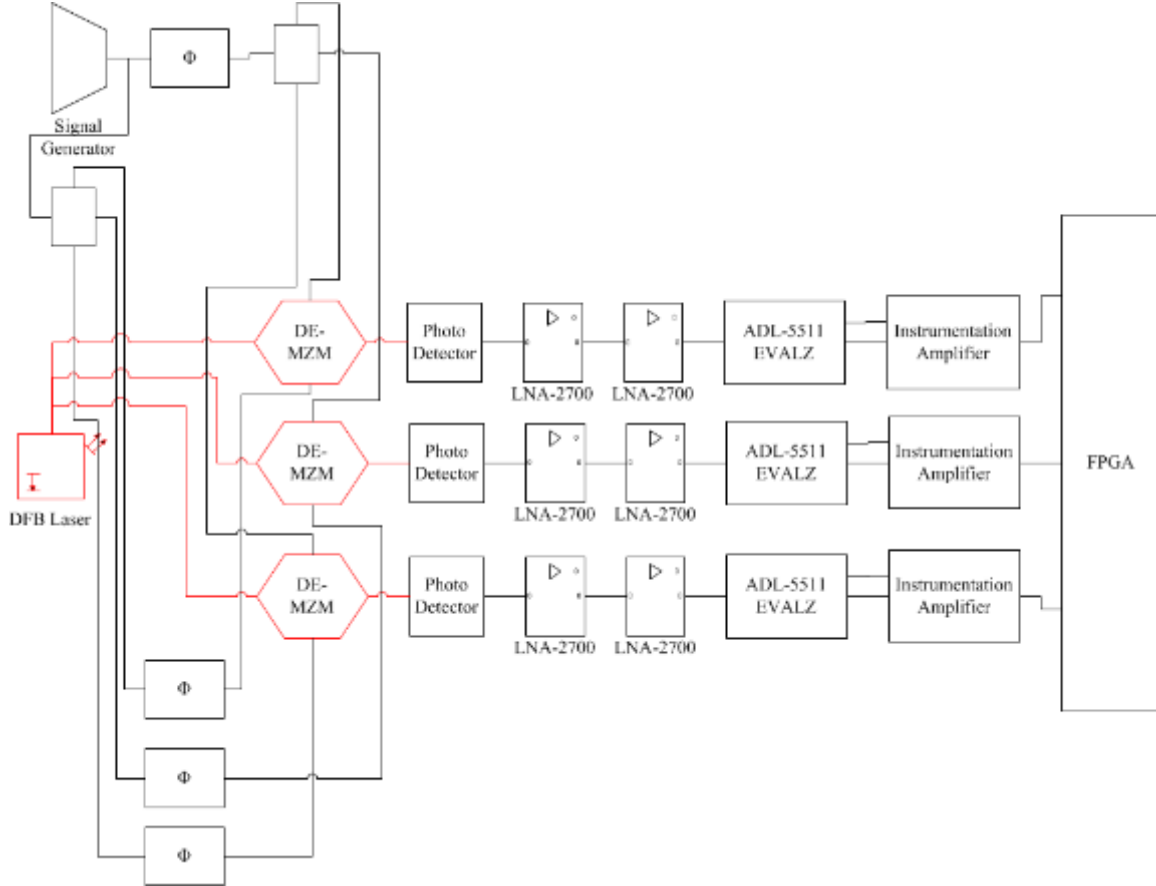
Bench testing of the system showed that DOA measurement should be possible using RSNS preprocessing. Some errors were found, however, and these were suspected to be attributable to drifting modulator bias point and change in amplifier gain due to temperature shift. To mitigate the bias drift, which is a common problem in the MZM, constant calibration had to be performed during each test cycle. Minimizing drifting due to temperature shift was achieved through performing the test cycles in the evenings, when temperatures in the lab environment were expected to be more stable [22].

Suggested improvements to the design included bias control circuits for the modulators, amplifiers with increased stability, and adaptive gain control. Another approach suggested but not documented was temperature stabilization through various modes of cooling.

During the initial investigation of the system, additional factors possibly contributing to system instability were found. Several components were determined to have poor performance at the frequency used, and therefore were replaced with parts designed for operation at 2.4 GHz. Some of these components, most notably the Bias-Tees and the DC blocking capacitors, most certainly contributed to the instabilities described by [22]. The plastic boards used for mounting of equipment possessed very poor electric and thermic conductivity, possibly resulting in voltage differences between what was supposed to constitute common ground at different parts of the system. The poor thermal performance might have contributed to temperature differences in the system, further increasing the impact on system stability as previously described.

Generally, receiving RF systems are very sensitive to noise, and minimizing all sources of internal noise is an important part of the engineering of such systems. Amplifiers need to be added as early as possible in the system, so as to amplify as little as possible of this internally generated noise. In the previously described design, 48 dB of gain was added after the PD, amplifying noise related to laser instability, RF interference, MZM anomalies, and PD dark current. This amplification approach was necessary due to the low modulation voltages at the MZM electrodes, resulting in very low modulation on the laser output.

B.   SYSTEM MODIFICATIONS

Most notably, the hardware used in [22] needed the addition of a design for receiving and adapting signals for the assembly to be useful in the detecting and processing systems. The reason for this need stemmed from the fact that future testing of the concept would be performed with aerially conveyed electromagnetic signals in an anechoic chamber. This move from a lab bench environment toward a more realistic scenario was part of the system maturity process aimed at finding a system for field use.

The receiving system needed to be interoperable with systems described in Figure 1. The antenna sub-system was defined and under construction when the design was initiated why some requirements were derived from the antenna design.

The primary functions for the receiving system were to

- amplify signals from antenna outputs (#0–3 in Figure 1) to a signal level useful for driving the MZM, depicted as red irregular hexagons in Figure 1

- split signals from the reference antenna (#0 in Figure 1)

These primary functions needed to be sustained continuously for as long as one testing in the anechoic chamber was performed, most probably a few hours at a time. The testing might need to be repeated 10 times or more. Due to the fact that all testing was to be performed in a relatively clean, dry, and temperature-controlled lab environment, the need for extensive environmental requirements was assumed to be low. Performance focus was on signal quality and stable, predictable output to the MZM.

In order to calibrate the system, as well as increase testing capabilities and future development, some analogue signal manipulation functions were needed. These were considered secondary to the two functions listed previously.

- apply phase shift to signals

- control DC bias levels

- provide signal measurement locations without disrupting the signal path

In addition to these added functionalities, several of the described stability and noise problems needed to be addressed:

- thermal stability

- reliable common ground

- increased signal levels

- verified performance at 2.4 GHz

This chapter provided a brief overview of previous work on a photonic DF receiver, and its identified limitations were also described. From these limitations, a number of added functionalities were derived, together with some other improvements

that were deemed necessary after investigation of the previous system design. Before proceeding to a more detailed design of the system used for this research, the MZM needs to be discussed since it is at the heart of the system analysis. This is done in the following chapter.

THIS PAGE INTENTIONALLY LEFT BLANK

III. PHOTONIC COMPONENTS USED IN THE DESIGN: MACH-ZEHNDER OPTICAL MODULATOR

Early work by Mach [24] and Zehnder [25] led to them, separately and unknowing of each other's efforts, discovering novel interferometric effects in light. The Mach-Zehnder interferometer was devised in 1891–1892 [26] based on their findings and allows a light source to be modulated by splitting its light into two separate beams. These light beams are sent through paths of different length, thus creating a relative phase difference between them. When the two beams are merged back together, the intensity of the resultant merged light beam is a function of the beams' relative phase difference. The extreme cases occur at zero and π phase difference. In the first case, the merged light beams are in phase and add together without destructive interference, yielding output intensity equal to the input. In the latter case, the two separate beams are inverse and cause a perfect destructive interference with a theoretical output intensity equal to zero.

Another finding from the same time is the linear electro-optic effect. Sometimes referred to as Pockels effect, it laid the foundation for the Mach-Zehnder modulator (MZM). In this device, the incoming laser beam is split into two paths. These two paths are produced from a material with appropriate electro-optic characteristics, causing a delay in each path relative to a voltage supplied to electrodes affecting the individual paths. Different versions of the MZM exist, but the two most common are the single-electrode and the dual-electrode (DE-MZM); the latter is also referred to as the dual-drive MZM, as shown in Figure 2.

Figure 2.   Schematic Picture of Dual-Electrode MZM
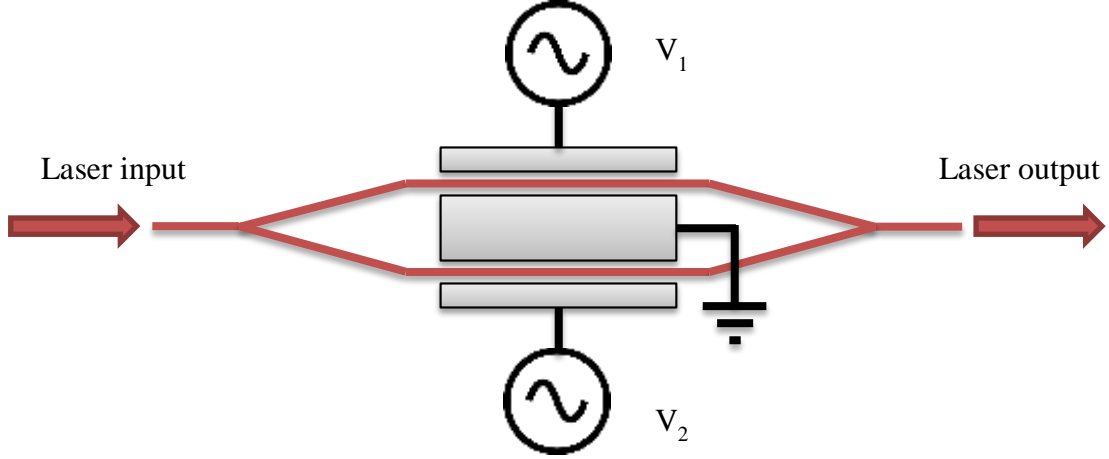
The voltage required to change the optical phase π radians is referred to as V_π, or the switching voltage of the MZM. Applying voltages to the electrodes of a DE-MZM with a relative difference of V_π changes the state of the modulator output from totally constructive to totally destructive interference, thus the term switching voltage. The transfer function of the DE-MZM transmission factor T_E as a function of the drive voltages has been formulated as [27]:

$$T_E(t) = \exp\left(j\pi\left[V_1(t) + V_2(t)\right]/\left(2V_\pi\right)\right)\cos\left(\pi\left[V_1(t) - V_2(t)\right]/\left(2V_\pi\right)\right) \tag{1}$$

where $V_1(t)$ and $V_2(t)$ are the drive voltages at the two input electrodes. By adding a bias voltage V_{bias}, the operating point of the MZM can be shifted to suit the needs for the specific application in which the modulator is used.

$$T_E(t) = \exp\left(j\pi\left[V_1(t) + V_2(t) + V_{bias}\right]/\left(2V_\pi\right)\right)\cos\left(\pi\left[V_1(t) - V_2(t) + V_{bias}\right]/\left(2V_\pi\right)\right) \tag{2}$$

When optical fiber communication links were introduced, it was commonly believed that direct modulation of the laser diode would be the prevalent technique for data transfer. Problems with chirp in this construction limits the practical use of direct modulation to about 10 Gb/s, but due to its low cost and small size, it is widely used for low data rates over short distances. Development of the MZM for laser applications has

been driven by the data communication community, and its importance increases with the ever higher demands for high data rate communication over long distances.

The most common material for MZM manufacturing is titanium-indiffused lithium niobate (Ti:LiNbO$_3$) [26]. It is used due to its Pockel's effect, low insertion loss, and the availability of LiNbO$_3$ wafers for production of components. Ti:LiNbO$_3$ modulators have very low chirp if used in dual drive mode and have a high extinction ratio (typically 20 dB) paired with a low insertion loss (typically 5 dB). These characteristics are desirable for laser modulation, especially at high data rates (typically 40 Gb/s) and long distances.

The electro-optic characteristic in lithium niobate poses some challenges for design and manufacturing. Applying a voltage to the electrodes of the MZM results in an electric field along a specific crystal axis but will affect the refractive index along one or more of the three crystal axes. Due to this, the MZM is sensitive to the polarization of the light entering the structure and the alignment of the voltage across the lithium niobate substrate [26]. The polarization sensitivity of the MZM demands the use of polarization-maintaining fiber from the laser source all the way through the modulator; otherwise the device and its operation will be unstable.

Since the modulator is ferroelectric, its electric-dipole moment is temperature dependent. This causes its bias point to shift proportionally to the temperature change. This can be mitigated either by keeping the temperature at a controlled level or through constant monitoring of the bias voltage [26], [28], [29].

Another challenge in a design using a Ti:LiNbO$_3$ modulator is its relatively high switching voltage (typically 4V). The switching voltage is dependent on the length of the structure; the longer the lithium niobate structure, the lower the switching voltage. There is also an inverse relationship between structure length and bandwidth, resulting in the length of the MZM being a trade-off between low switching voltage and high bandwidth. To achieve 40 Gb/s of bandwidth, the maximum possible length corresponds to a switching voltage between 3V and 5V. These longer structure lengths needs to have matched propagation speeds along the optical path and the electrical, assuring that the

17

waves propagate at equal speed. Several MZM designs target this issue with the electrodes forming a transmission line along the optical path [26].

The high switching voltage needed to drive the MZM is generally manageable when the modulator is used for transmitting data, since the voltages needed are of the same order as electrical digital signals. When an MZM is used in an RF receiver system, it poses more of a challenge. For an electronic support (ES) receiver, a sensitivity of – 80dBm is not uncommon. Amplifying such a low signal level to the typical +25 dBm needed to drive the MZM optimally demands a total system gain of more than 100 dB.

Due to the piezoelectric properties of lithium niobate, there exist acoustic effects due to the drive frequency used in the MZM. Most of these effects are only present at frequencies below 1 GHz, but they may also affect performance at higher frequencies [26].

This chapter described the basic construction and characteristics of the dual port MZM. The understanding of voltage biasing and drive voltage in relation to output intensity is adamant in the system design of the front-end receiving layout. This is discussed in Chapter V, but the test environment must first be defined, since this puts some important restrictions on receiver design. The following chapter describes the fundamental parameters of the planned test environment.

IV. DESCRIPTION OF TEST ENVIRONMENT

The RSNS receiver system is designed for anechoic chamber tests at Naval Postgraduate School (NPS) in Spanagel Hall, Room Sp-604. This room is electrically shielded, and the floor, walls, and ceiling are clad with RF absorbent material. A rotating pedestal is used for mounting the receiver system in the chamber, and the distance r from the transmit antenna to the center of the pedestal is 5.7 m. The test environment is depicted in Figure 3.

Figure 3.   Transmission Antenna and Anechoic Chamber as Seen From
Receiver Antenna Array

For the measurements to be considered performed in the far-field, the following criteria needs to be met [30]:

$$r > \frac{2D^2}{\lambda}$$
$$r > 5D$$
$$r > 1.6\lambda \tag{3}$$

where D is the aperture size of the transmission antenna. A Tecom 201302 log-periodic antenna (shown in Figure 4) with a baseline of 20 cm was used for transmission and it is clear that the measurements were performed in the far-field since

$$5.7 > \frac{2D^2}{\lambda} = 0.64$$
$$5.7 > 5D = 1.0$$
$$5.7 > 1.6\lambda = 0.2 \tag{4}$$

The transmission antenna was fed with a 2.4 GHz continuous wave (CW) signal generated by an HP 83711B signal generator, amplified by a HP 8348A amplifier to 25 dBm at the antenna input. Transmission polarization can be selected as vertical or horizontal depending on what input is used on the Tecom antenna. Since vertically polarized dipole antennas need to be used as receivers, a vertical polarization was selected for the transmission antenna.

Figure 4.   Transmission Antenna (Tecom 201302) Used for Emission of Test Signal

The test environment has been specified in this chapter, providing necessary data for designing the receiver system. Test environment data, together with an understanding of the MZM function, were used to derive specifications for the receiver design described in the following chapter.

V. SYSTEM DESIGN

This chapter provides a system design analysis of the DF receiver.

A. SYSTEM FEASIBILITY ANALYSIS

There were some restrictions imposed on the design. First of all, there were already some interfaces in place, and those must be addressed. Secondly, the budget for the construction was limited by the amount allowed by the Department of Defense without the need for involving the slower and more extensive acquisition process.

The primary and secondary functions performed by the system were typical for most RF front-ends, and the technology is mature and widespread. Economic factors needed to be considered, since high performance RF components in general are costly. Due to the fact that the budget was limited, price was a driving factor in the design of the system.

All primary and secondary functions could be performed by commercially available off-the-shelf (COTS) components. A brief survey showed that there were innumerable providers of RF components for laboratory use. This yielded the conclusion that two approaches should be feasible:

- a system consisting of sub-components interconnected by cables

- a system consisting of surface-mounted components interconnected by a circuit board

B. SYSTEM OPERATIONAL REQUIREMENTS

In this section, the necessary requirements for proper system operations are described.

1. Distribution and Deployment

The system was used in a lab environment for testing and evaluation purposes. Personnel operating the system were expected to have extensive knowledge of the system construction and function. The surrounding environment was expected to be at room temperature and have low impact on system performance. The only environmental factor

that might affect system performance was circular motion due to the rotating pedestal the system was mounted to in the anechoic chamber.

Since the system was used for confirming results in [22] and was not meant for extended use, endurance and long-term performance played a minor part in the design.

2. Performance Parameters

As mentioned previously, signal quality and economy were at the core of the design. This is reflected in the following list of performance parameters:

- input sensitivity

- output voltage

- noise figure

- frequency

- voltage standing wave radio (VSWR)

- impedance

- price

3. Interfaces and Interoperability

The pedestal in the anechoic chamber had a pattern of holes meant for attaching equipment to its top. An appropriate number of these holes needed to be used to fix the receiver system to the pedestal, and corresponding holes were needed in the receiver assembly.

In order to minimize temperature differences between the components in the receiver, all components needed to be mounted on a common surface with high thermal conductivity.

Electrical connections in the signal path must all comply with International Electrotechnical Commission (IEC) 60169-15 (SMA connector, 50Ω).

Input sensitivity had to be matched to the expected output signal level from the antenna elements, and output signal level had to be sufficient to drive the MZM. Control

voltage levels were restricted by available output voltages for the National Instruments (NI) cRIO real-time computer used for measurement and control.

4.   Environment

The receiver system was expected to be operational for a limited amount of time. In order to minimize environmental impact, reusability of the components was considered. If there was a choice between similar components where one could only be used for this system and the other might be reused for other experiments in the laboratory, the latter was chosen.

5.   Maintenance and Support Concept

Due to the expected short life span of the system and its very limited experimental use, maintenance and support concepts were not considered in the design.

6.   Technical Performance Measures

Generally, the deriving of technical performance measures (TPMs) is an iterative process based on breaking down the system step by step into smaller detail (Blanchard, 2008). In this design, due to the fairly well-specified demands, interfaces, and interactions of the system, the TPMs were derived in a very detailed way based on the requirements and performance of adjacent systems. This is illustrated in Table 1.

Table 1.   System TPMs

Parameter	Value	Unit
Input sensitivity	<1	dBm
Output voltage	0-4	Vpp
Noise figure	<5	dB
Frequency	2.4	GHz
VSWR	<5	:1
Impedance	50	Ω
Control voltage	0-10	V
Phase shift	0-360	degrees

C.   FUNCTIONAL ANALYSIS

This section describes a functional breakdown of system functionalities.

1.   Amplification

The amplification function received the signal from the antenna as its input. The purpose was to amplify the signal to a level that could drive the MZMs almost to their V_π levels. The output needed to take into consideration varying input levels and provide some form of gain control to keep the output voltage at correct levels. It also needed to compensate for potential losses in other components in the signal path.

2.   Signal Split

Signal splitting needed to be performed for the reference signal in order to distribute it to all three MZMs. Due to the behavior of the modulators and the principle for mixing signals in them, it was very important that the splitting function distributed the power equally between the output channels and did not introduce phase differences between the outputs. Since this function was passive, low loss was essential to the overall performance of the entire system.

3. Phase Shift

The phase shifting function needed to be able to act individually on all three measurement channels, possibly on the reference channel as well. It had to be able to perform phase shifts of up to one full period for the frequencies used in the receiver. Low loss was important in this component just as it was for all passive components in the signal path.

4. DC Voltage Control

Since MZM operation depended on where the input signals were biased, some form of DC voltage control was needed. The DC control function had to be able to change the bias voltage over at least one V_π.

5. Signal Measurement

This function was needed for two reasons. First and foremost, it was needed for gain control of the amplifying function, but it would also provide necessary points for error tracking if diagnostics needed to be performed on the system in case of malfunction. Ideally this function allows for signal sampling without disruption of the main signal path; this was needed to be able to observe the system while operational.

The relative importance of the five main functions is shown by their size in the diagram depicted in Figure 5.

Figure 5.   System Functions
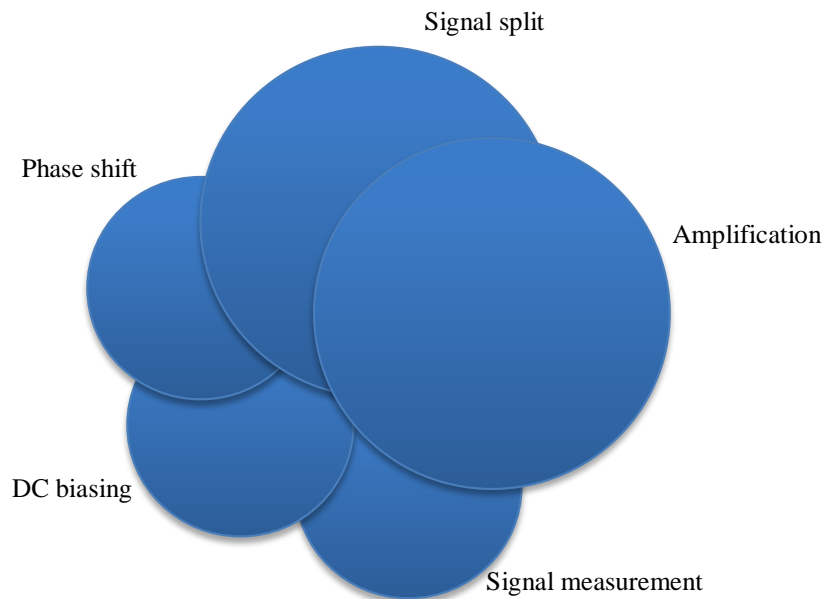
D.   REQUIREMENTS ALLOCATION

Having the environment requirements in mind, a modular approach to the design was deemed most suitable. The concept of surface mounting all components on a circuit board was discarded, since this approach would disrupt the reusability of system components. A circuit board solution would most probably be the favored solution for a mass-produced system yielding substantial economic advantages compared to connectorized modules. In this case, however, a single system meant for limited use was designed.

The five main functions listed previously were all translated fairly easily into connectorized sub-components available as COTS items. Due to the TPMs listed previously, the following translation of function into sub-component was made:

- Amplification: Low noise amplifiers (LNA)

- Signal split: Power divider

- Phase shift: Voltage controlled phase shifter

- DC voltage control: Bias-T

- Signal measurement: Directional coupler

E.   ANALYSIS AND DESIGN OPTIMIZATION

In RF design, especially when low noise is important, amplification should be done as close as possible to the incoming signal interface, in this case, as close to the antennas as possible. Generally, voltage-controlled LNAs have poorer performance and are more expensive compared to fixed gain LNAs. The problem with using fixed gain LNAs is that the design requires the system to be able to vary the overall system gain. This can be accomplished using a voltage-controlled attenuator connected in series after a fixed gain LNA.

Phase-shifting and DC-biasing components were added after the initial amplification was done, mainly because this reduced their noise contribution. Signal splitting was the final stage in the reference channel, and since four-channel power dividers are more common than three-channel ones, there was a fourth port available for signal measurement. The other three channels had the directional coupler in line with the output to the MZM.

In this chapter, the functional design of a photonic DF system was discussed. The described system functions need to be translated into a component design able to meet the TPMs previously stated while requiring as little economic means as possible. In the following chapter, these system components are described and analyzed.

THIS PAGE INTENTIONALLY LEFT BLANK

VI. SYSTEM DESIGN IMPLEMENTATION

This chapter includes a detailed description of the system design, starting with a schematic description as shown in Figure 6.

Figure 6.   System Block Diagram
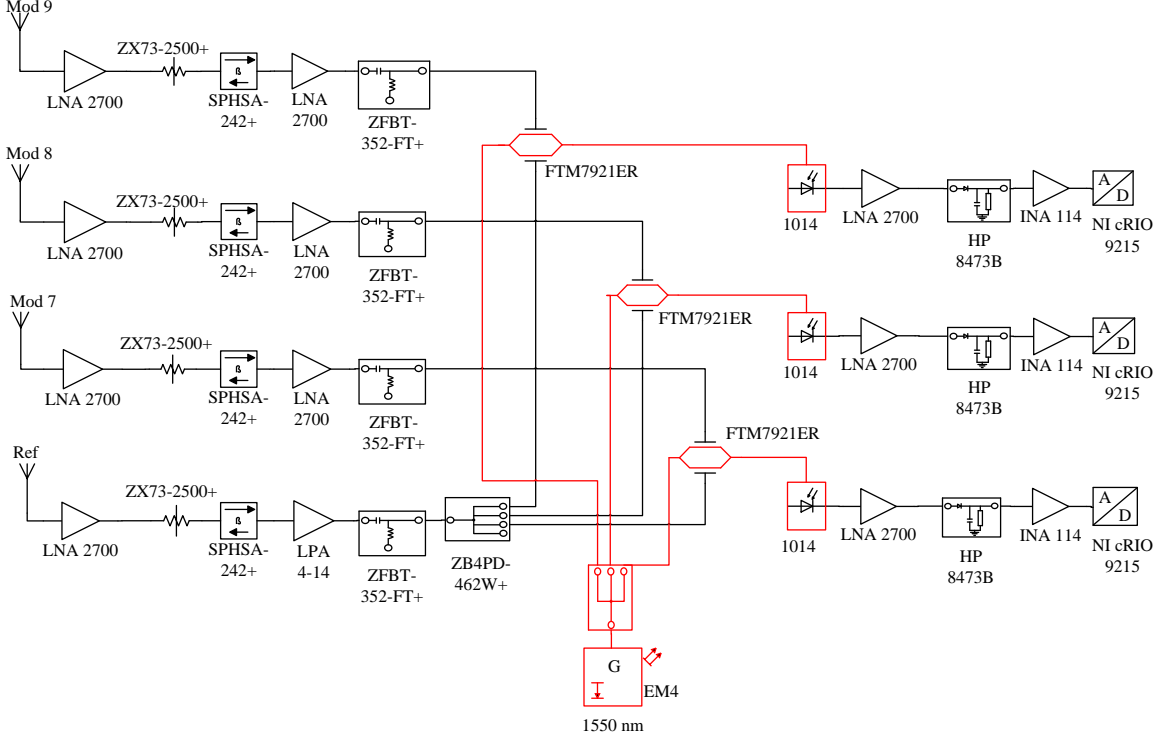
A.   ANTENNA ARRAY

Restrictions in prototype manufacturing limited the choice of antenna elements to dipole antennas. Four half-wave dipole elements, etched on individual printed circuit boards (PCB), were used. The antenna elements had an individual relative gain of 5.15 dBi [30].

The distance d_i between measurement antenna elements and the reference antenna were given by [22].

$$d_i = \frac{\lambda \widehat{M}_{RSNS}}{4 m_i N} \xi$$

(5)

29

where λ is the RF wavelength, $\widehat{M}_{RSNS}$ is the dynamic range of the desired RSNS system, and N is the number of sequences. Previous work examining RSNS preprocessing in a DF receiver was performed using a right-shifted RSNS with $m_i = \{7,8,9\}$ and $\widehat{M}_{RSNS} = 133$[22]. For ease of comparison of results, the same values were used in this system design. The scaling factor is reduced if the field of view (FOV) is decreased from 180° and is determined by [32]:

$$\xi = \frac{1}{\sin(FOV/2)}$$

(6)

Reducing the FOV to 120° yielded a scaling factor of 1.1547, and the computation of the element distances resulted in

$$d_7 = 228.5\,mm$$
$$d_8 = 200\,mm$$
$$d_9 = 177.7\,mm$$

The antenna array was fixed through an aluminum sheet with outer measurements 30×60 cm, providing a ground plane for the array.

The direct-ray propagation is described by the Friis equation, also known as the one-way link equation [33]. Received power P_r at the receiving antenna is computed as

$$P_r = \frac{\lambda^2 G_r G_t P_t}{(4\pi)^2 d^2}$$

(7)

Gains for transmit and receive antennas G_t and G_r should be given in relative numbers, transmit power P_t in watts, and the distance between antenna elements d in meters. For the conditions given by the testing environment and the selected receiving antenna elements, the theoretical power at the output of the receiving antenna element was calculated to -17.8 dBm.

The antenna array setup is shown in Figures 7 and 8.

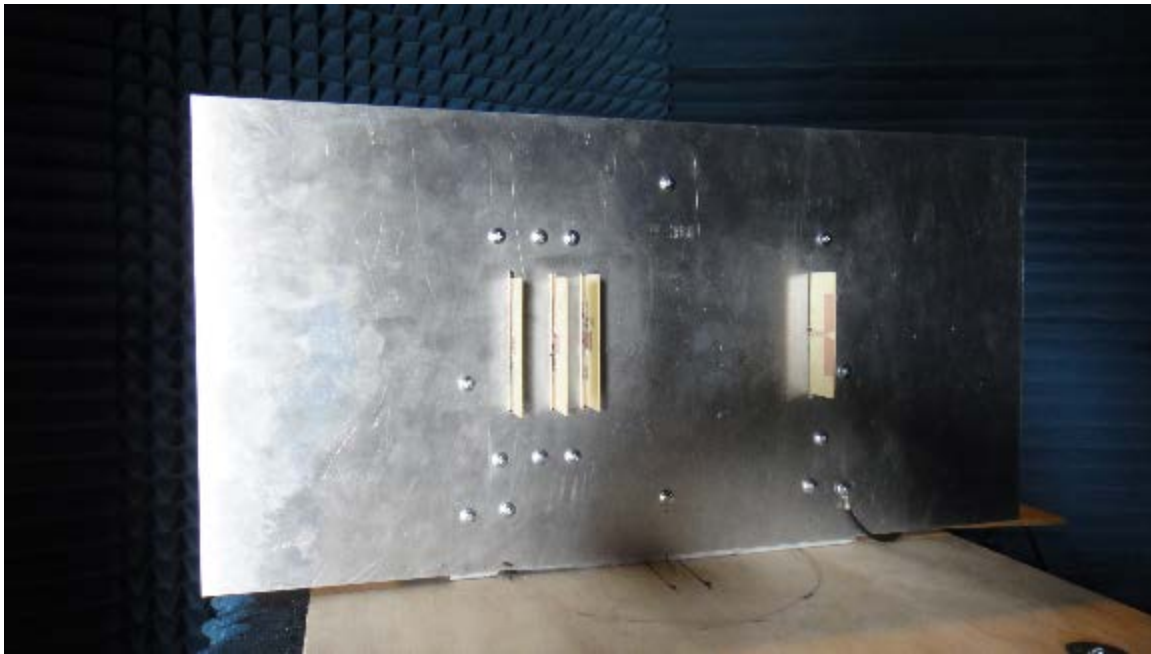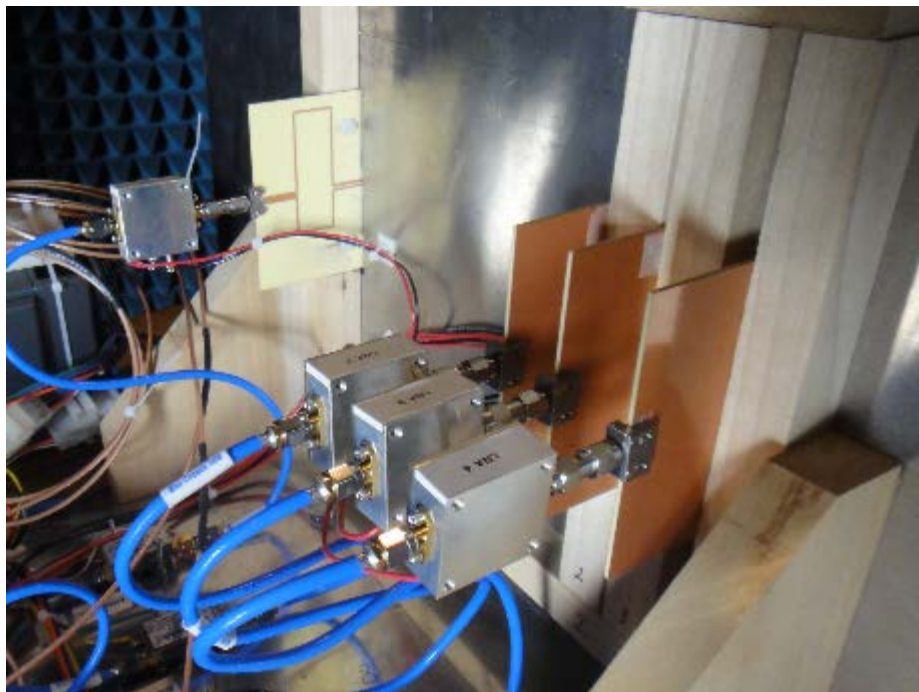Figure 7.   Antenna Array Pictured From the Front

Figure 8.   Antenna Array Pictured From the Back

Note: LNA shown attached directly to the output of receiver dipoles

B.   BOARD MOUNTING (5052 H32 ALUMINUM, 0.1875IN)

The physical layout of components on the board should have made signal measurements in various places easily accessible. To minimize reflections from the mounted components, a width smaller than that of the antenna array was chosen. A board size of 12 in x 36 in was used because it was the largest standard size pre-cut aluminum sheet that could fit on the pedestal behind the antenna array.

1.   Mechanical Considerations

The board was mounted to the antenna pedestal at one end while the main part was extended out behind it. This could lead to the free part of the board flexing during movement, which in turn could impact the electrical characteristics of the system. To mitigate this, a light and strong enough material was used.

5052 aluminum is commonly used in the industry for electronics casings and other applications where a combination of strength, conductivity, and low weight is desired. Another beneficial characteristic is its high corrosion resistance.

2.   Electrical Conductivity

Vagabonding currents in small-signal systems can decrease performance or, in the worst case, destroy components. To mitigate these problems, a common ground with low overall impedance between parts in the system needed to be achieved.

Pure aluminum has a resistivity of 2.826×10^{-8} ohms/m [34]. The 5052 aluminum alloy has a higher resistivity of 4.843×10^{-8} ohms/m, but is still lower than most other possible construction materials for the design, such as various iron alloys like stainless steel [35].

3.   Thermal Conductivity

Previous attempts to design a DF system based on RSNS processing and optical modulation indicated that temperature differences in the system might have been a cause to signal instability [22]. To mitigate extreme local temperature swings, resulting in differences in component operating temperatures, the construction material must have

good thermal conductivity. Aluminum alloys meet this requirement, and the low corrosion in the 5052 alloy means that surface conductivity does not degrade with time.

4.   Mounting Paste (MG Chemicals 847)

Mounting paste for electrical components is generally designed for high thermal conductivity and very low electrical conductivity. As stated previously, good electrical and thermal connections between the mounting board and the components were both desired. Very few products with these properties were available on the market, and they generally had lower thermal performance than the electrically insulating and more common types. Mounting paste with exceptional performance both thermally and electrically was available, but could not be used for economic reasons. A paste with balanced characteristics in all aspects was chosen for the system.

Figure 9 shows the completed board setup.

Figure 9.   Receiver Components and MZM Mounted on Board
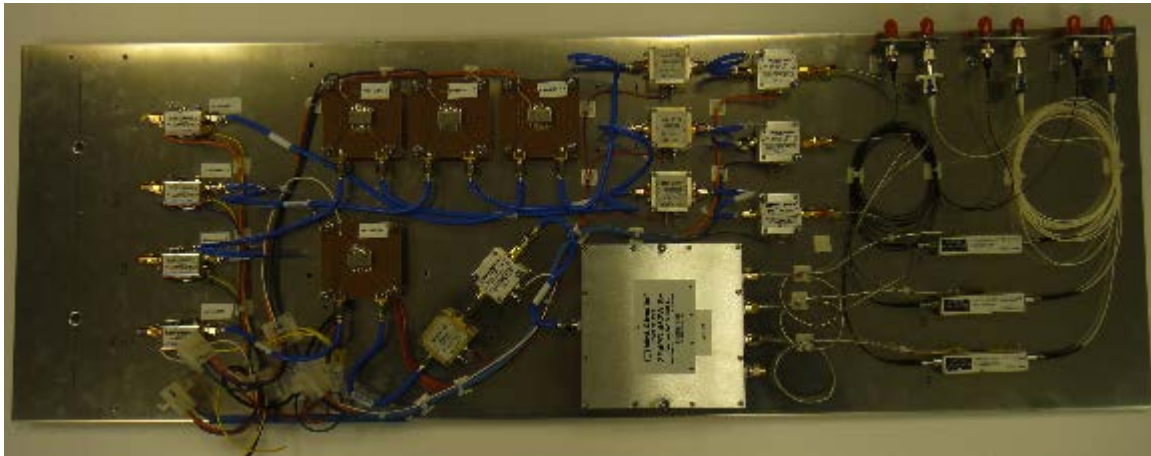
Note: The directional couplers are not shown in this picture, but were installed later.

C.   RF RECEIVER AND MZM DRIVER

Electrical components in the receiving and signal conditioning part of the design are described in this section.

1.   **Low Noise Amplifier (RF BAY LNA-2700)**

The combination of high gain, low noise, and competitive pricing [36] made the LNA-2700 the amplifier of choice in the system. The only limitation the amplifier brought to the design was its maximum output power of +10 dBm. This was enough for driving the three measurement channels, but not sufficient for the signal splitting needed in the reference channel, so a different amplifier had to be used in the final stage of that channel. Performance of every LNA was individually tested and found to be well within the manufacturer specifications [36].

2.   **RF Cables (Minicircuits 141-xSM+)**

The system components had little or no movement in relation to each other, and a semi-rigid type of coaxial cable could be used. To accommodate possible rearrangements of components and changes to the prototype during the construction, hand bendable cables were deemed to be most suitable. These can be re-used and rearranged several times without negative effects on performance, but still provide low loss and good noise characteristics. The cable type chosen for the design possessed all of these characteristics while being very affordable compared to equivalent alternatives [37]. SMA connectors were used for all RF connections throughout the system.

3.   **Voltage Variable Attenuator (Minicircuits ZX73-2500)**

Variable-gain amplifiers were initially considered for the design, but poor performance paired with economic considerations deemed them less feasible for the system. To be able to regulate the overall system gain, a design with variable attenuators was chosen. In order to be able to alter gain and phase through computer control, the control voltage needed to be in the range of available outputs from the NI cRIO computer.

Gain and phase control were critical in the design of this system, which is why a considerable amount of time was spent measuring these characteristics. The manufacturer supplied performance measurements at +3V and +5V supply voltage [38], but since

performance at 0V was considered more suitable for the design, measurements were performed to characterize the component at this supply voltage.

Transfer functions for gain and phase in relation to control voltage was measured at two conditions: 0V supply voltage and +5V supply voltage. This is illustrated in Figure 10.

Figure 10.   Measured Attenuation Transfer Function for Voltage Variable Attenuator
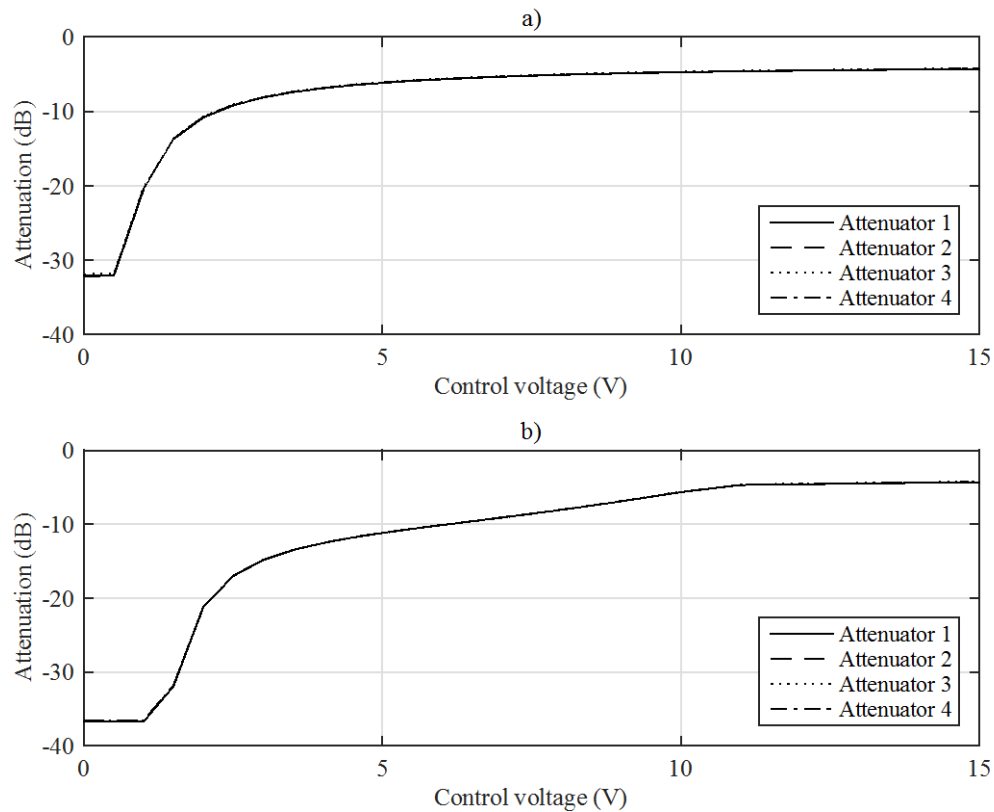
Note: a) @ 0V supply voltage, b) @ +5V supply voltage

As shown in Figure 10, attenuation was not a linear function of the control voltage. The design was expected to require attenuations between –20 dB and 0 dB; the attenuation curve for 0V supply voltage provided the desired attenuation range while having a more favorable and predictable behavior. Minimum insertion loss at 0V supply voltage was –5 dB and was achieved at control voltages exceeding 7V.

Unfortunately, variable attenuators also affect the phase of the signal. The phase shift was a function of the control voltage, as seen in Figure 11.

Figure 11.   Measured Phase Shift Transfer Function for Voltage Variable Attenuators
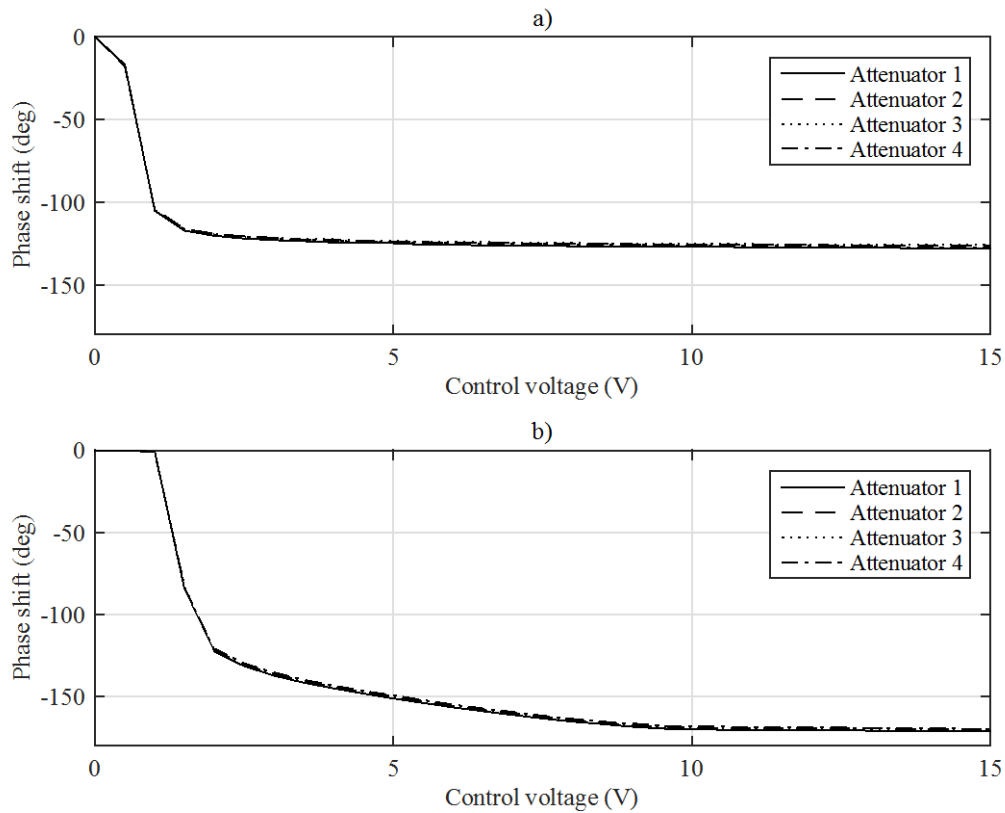
Note: a) @ 0V supply voltage, b) @ +5V supply voltage

From Figure 11, it is obvious that the phase shift was different for 0V and +5V supply voltage. The linked relationship between control voltage, attenuation, and phase shift was a complicating factor when calibrating the system.

4.   Phase Shifter (Minicircuits SPHSA-242)

As previously discussed, the phase in each channel needed to be adjustable. A thorough survey of the market showed that there were very few connectorized products

available with the desired characteristic and none at a unit price below $1500. An approach with a surface mounted phase shifter was decided on and designed, as shown in Figure 12. The chosen component [39] matched all necessary characteristics at a unit price below $100, which included the necessary components for PCB fabrication. Due to the unknown performance of the PCB, a thorough characterization of the four phase shifters was performed.

Figure 12.   Phase Shifter Mounted on PCB
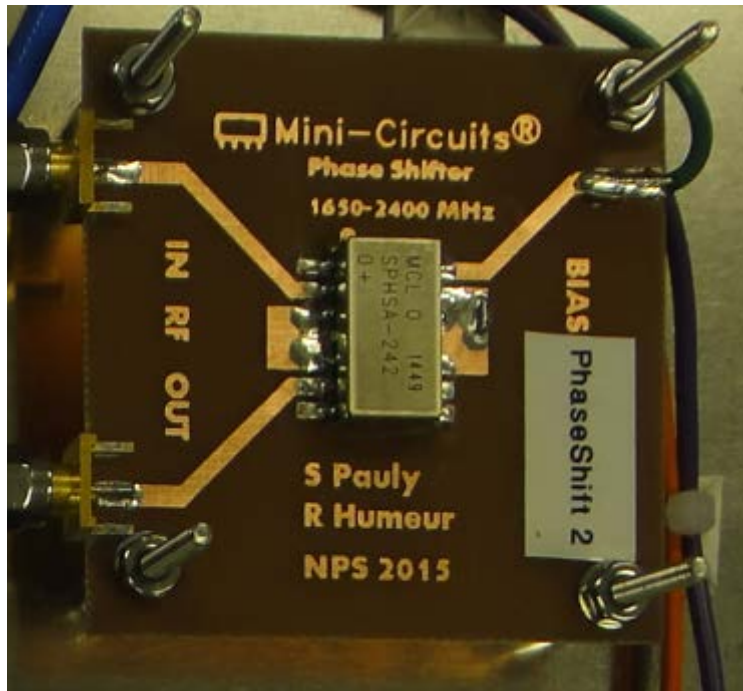
From Figure 13, it is clear that the assembled units could provide a full period phase shift for a control voltage range between 0V and +10V, thus meeting the functional needs of the component.

Figure 13.   Measured Phase Shift Transfer Function for Phase Shifters
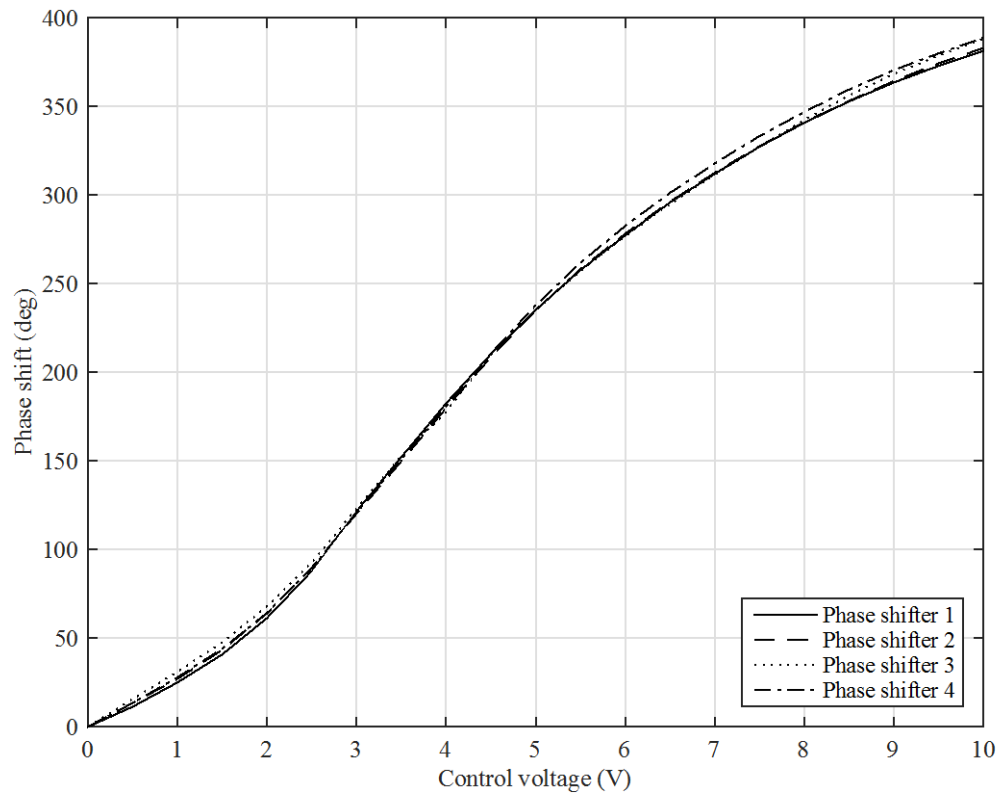
As was previously shown for the attenuators, both phase and attenuation were functions of the control voltage. This was also the case with the voltage variable phase shifters, as seen in Figure 14.

Figure 14.   Measured Attenuation Transfer Function for Phase Shifters
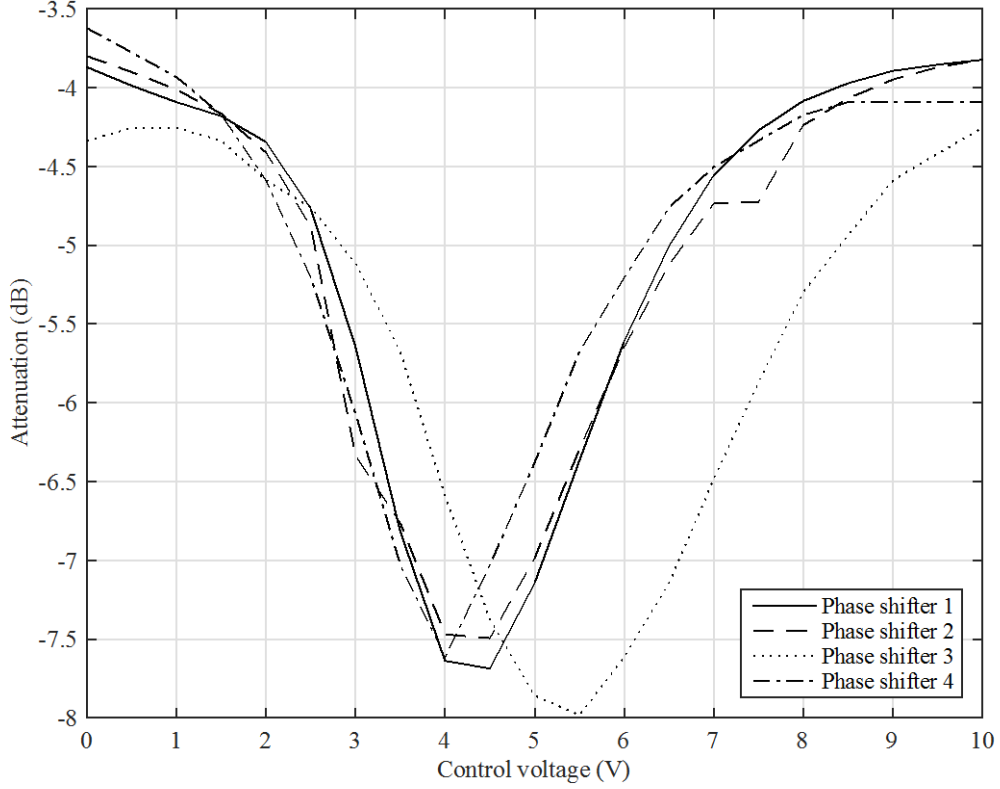
The attenuation in each phase shifter was related to the control voltage as pictured in Figure 14. Maximum insertion loss was determined to occur at approximately a half period phase shift for all four phase shifters with some variations. Component insertion loss was found to be in the range between –3.5 dB and –8 dB.

5.   RF Amplifier (RF BAY LPA-4-14)

It was previously mentioned that the LNA-2700 was unable to provide enough output power to drive all three MZM inputs through the splitter. Maximum output from the LNA-2700 was +10 dBm [36], and the four-way splitter constituted a –7 dBm attenuation [40], yielding a maximum output per port of +3 dBm if used together with the splitter to drive all reference inputs for the three MZMs. The LPA-4-14 could deliver +20 dBm [41] on the output port, resulting in +13 dBm per MZM input after splitting.

6.   Bias-Tee (Minicircuits ZFBT-352-FT)

In order to control the operating point of each MZM, a DC bias voltage might be needed. Several MZMs have a separate input port for the bias voltage, but unfortunately not the Fujitsu FTM7921ER used in this system. A bias-tee was thus needed in each of the four channels of the system to provide an input for biasing of the signal. Since amplifiers generally operate optimally with a signal biased at 0V, the bias-tee had to be inserted after all amplification was done. The possible addition of a bias voltage in the reference channel before splitting demanded a four-way splitter with DC pass-through.

The bias-tee chosen for the system had low insertion loss and excellent standing-wave performance [42].

7.   Four-way Power Splitter (Minicircuits ZB4PD-462W)

The reference channel needed to be distributed to all three MZMs, assuring that the signals at all three MZM inputs had identical phase and amplitude. For measurement and calibration purposes, an additional fourth output port was deemed necessary for the reference channel providing trigger signals to external instruments. The need for matched phase and amplitude at all four outputs was a driving criteria in component selection. Thorough analysis of available products with desired performance and comparison of price per unit resulted in the choice of [40]. The component was characterized and found to exceed manufacturer-provided specifications. The total loss per channel in the splitter was typically –7 dBm, out of which –6 dBm is the theoretical loss due to dividing the signal power by 4.

8.   Directional Coupler (narda microline 4202B-10)

Four −10 dB couplers were available for the experiments. If possible, −20 dB or −30 dB would have been preferred to maximize signal level to the MZM, but since the –10 dB couplers were provided at no cost and performed reasonably well, they were used in the system.

D. OPTICAL SIGNAL PATH

This section describes functionalities in optical components used in the design.

1. Laser Diode (EM4 EM253-080-053)

An EM4 laser with maximum optical output power of 80 mW was used. The laser diode was mounted in a Newport 744 butterfly mount with integrated cooling and controlled by a Thorlabs ITC 510 laser diode combi controller.

2. Optic Fiber

Performance of an interferometric modulator is strongly dependent on the polarization of the laser input. For stable performance of the modulator, it is absolutely necessary to maintain stable light polarization at the MZM input over time. This demands polarization maintaining (PM) optical fiber and connectors.

Initial problems with system stability were thoroughly investigated and found to depend on the three-way laser splitter provided from previous research. The splitter and its connectors were not constructed to be PM, so the splitter had to be redesigned and modified. New connectors in the optical path were used, allowing for polarization alignment adjusting. Performance of the splitter was tested and verified after assembly using a Thor Labs PM300 optical power meter and a S144A sensor.

3. Mach-Zehnder Modulator (Fujitsu FTM7921ER)

The MZM was provided from previous research with a photonic RSNS DF system implementation. Due to economic reasons, no further investigation into replacing it with other modulators was done. Since this modulator was designed for differential drive, it employed dual input ports with a 180° relative phase shift between the two inputs. This meant that constructive interference, and thus maximum transmission, occurred when signals at the two inputs were exactly out of phase. Destructive interference, yielding minimum transmission, occurred at 0° relative phase shift between the inputs. Figures 15 and 16 demonstrate 0° and 180° relative phase shifts, respectively.

Figure 15.   Simulation of Fujitsu FTM7921ER at 0° Phase Shift
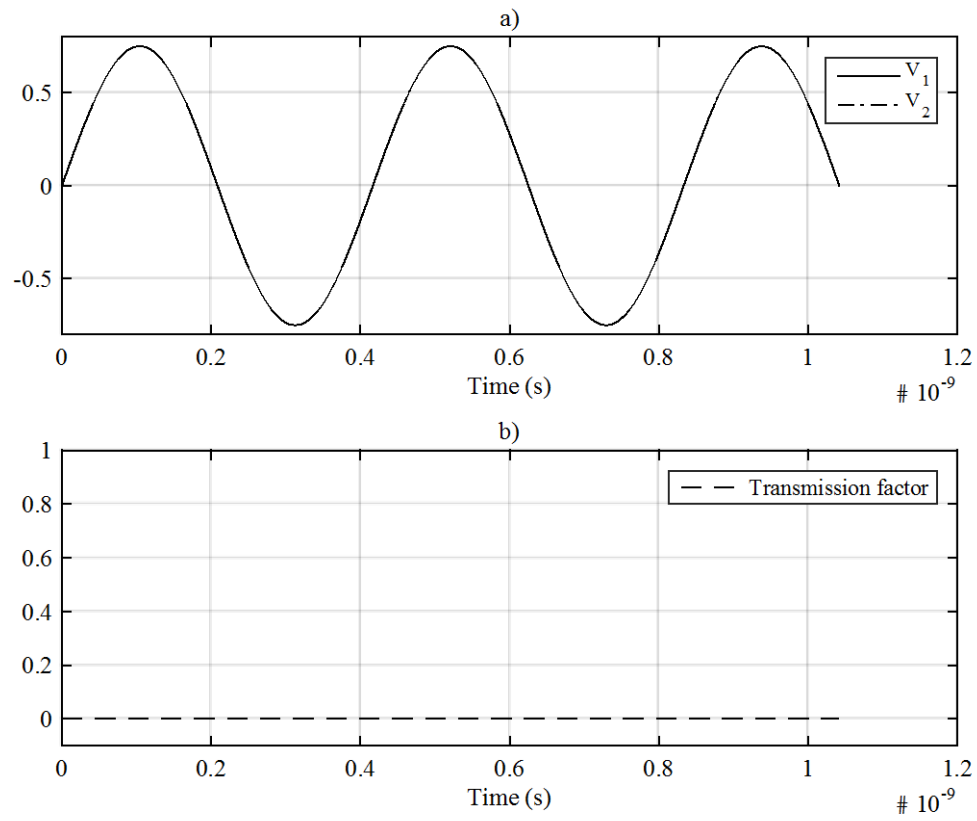
Note: Simulated at 2.4 GHz with 1.5 V_{pp} drive voltages. The drive voltages are shown in a), and the resulting transmission factor is shown in b).
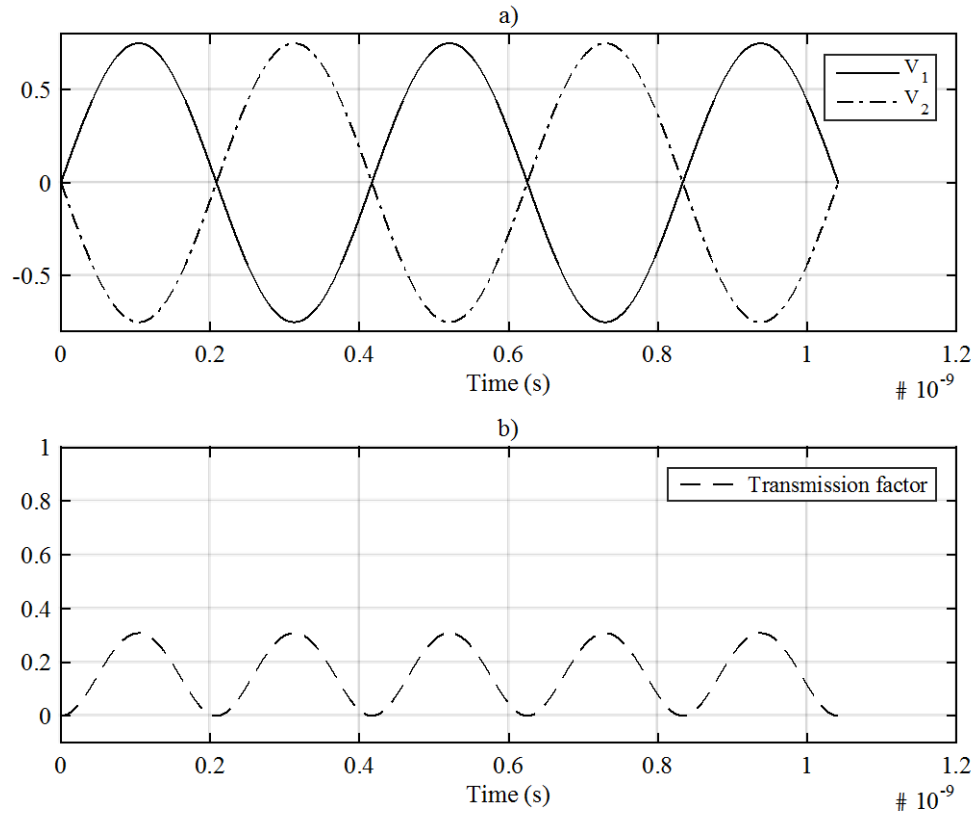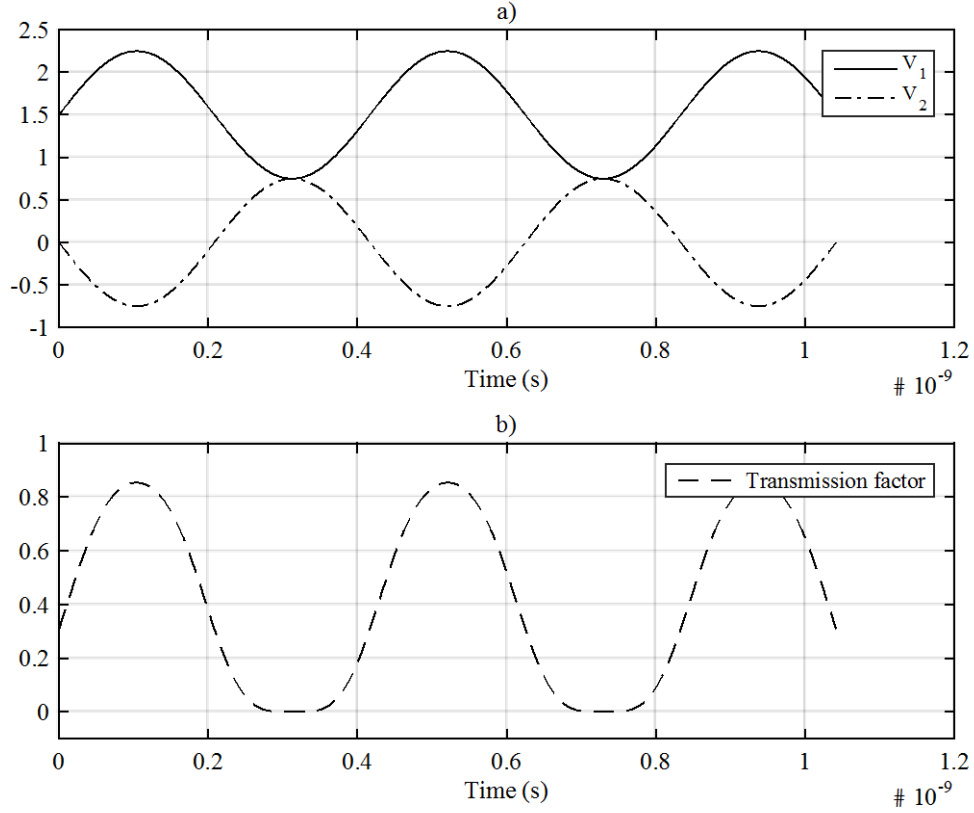
Figure 16.   Simulation of Fujitsu FTM7921ER at 180° Phase Shift

Simulated at 2.4 GHz with 1.5 V_{pp} drive voltages. Drive voltages are shown in a), and the resulting transmission factor is shown in b).

The effect of adding a bias voltage is shown in Figure 17.

Figure 17.   Simulation of Fujitsu FTM7921ER at 180° Phase Shift With
Added Bias Voltage

Note: Simulated at 2.4 GHz with 1.5 V_{pp} drive voltages and 1.5V bias added. The drive
voltages are shown in a), and the resulting transmission factor is shown in b).

Insertion loss was measured to range between 5–7 dB, which was consistent with specifications. During construction and bench testing, the MZM dependency on stable polarization of the input laser was found to play a significant role in modulator output stability. Temperature instability and bias voltage drift was also observed.

44

4.   Photo Detector (New Focus Model 1014)

Conversion from the optical to the electrical domain was performed in a battery-powered 45 GHz PD. Due to the low output levels from the PD, an LNA was deemed necessary before an envelope detector could be employed.

E.   BACK END ELECTRICAL SIGNAL PATH

This section describes the functionalities of components appearing after the optical signal had been converted back to the electrical domain.

1.   DC Blocker (Minicircuits BLK-18-S+)

The selected DC block was specified for operating up to 18 GHz with low insertion loss. Removing the DC bias in the output signal served the purpose of feeding the LNA with a signal biased at 0V for optimal performance.

2.   Envelope Detector (HP 8473B)

In previous research, an active envelope detector was used, employing a slight gain to the detected envelope. Since the approach used in the design of this system yielded a significantly higher output level, a simpler and more robust envelope detector was used. The HP 8473B is a passive device capable of operating at 0.01–18 GHz.

3.   Instrumentation Amplifier (INA114)

To optimize system output levels for sampling, a final stage of amplification was performed. The amplifier was adjustable and capable of bringing peak output voltages to 8V. The board and amplifier were reused from previous work, but resistor values were modified to achieve a correct adjustment range.

F.   REAL-TIME COMPUTER (NATIONAL INSTRUMENTS CRIO-9012)

The cRIO is a real-time computer with an FPGA array optimized for being programmed and controlled in LabView.

1. Output Modules (NI 9269)

Three four-port output modules were installed in the cRIO chassis used in this system. All output ports were fully isolated, so the negative output for each port had to be electrically connected to ground. Each port was capable of providing output voltages between −10V and +10V with a resolution of 16 bits. Maximum output current per port was 10 mA and max total output per module was 20 mA.

2. Input Module (NI 9215)

One four-port input module was installed in the cRIO capable of sampling voltages between −10V and +10V with a resolution of 16 bits.

3. Control Voltage Amplifier (TCA0372)

Initial trials with the system showed that the cRIO was unable to provide enough current to the output control ports. This was mitigated by adding operational amplifiers to each output port of the cRIO, designed to operate as voltage following amplifiers with a 1:1 input-output voltage relation, as shown in Figure 18. To ensure correct operation at 0V control voltage, the amplifiers were designed to be supplied with ±12V. The design was able to provide control voltages between 0V and 10V with a maximum current of 1A per output.

Figure 18.   Control Voltage Amplifier Installation
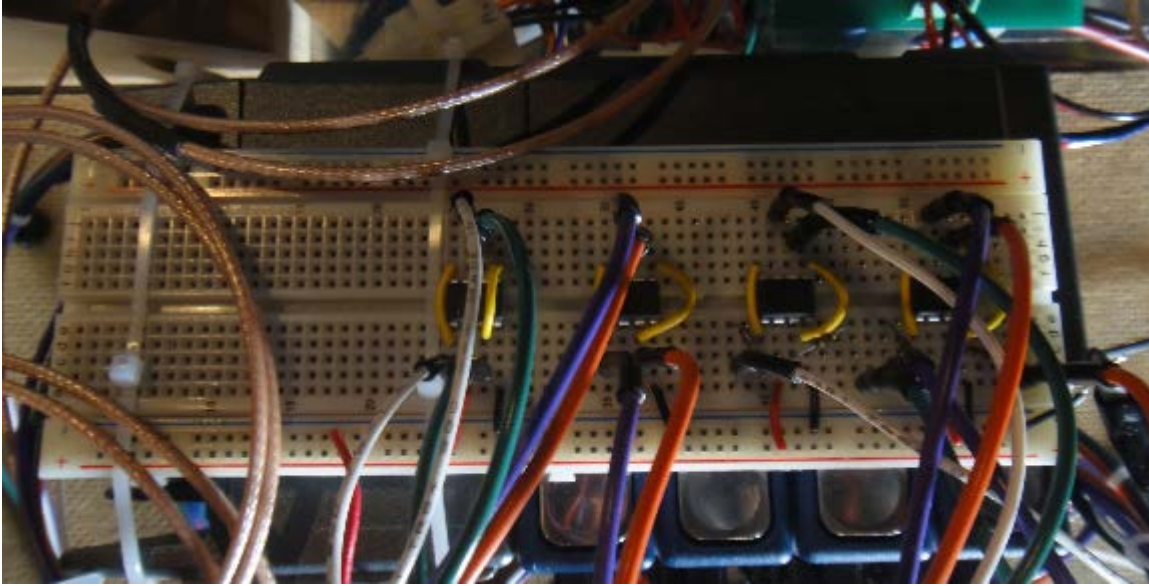
4.   LabView 2009 Applications

Two separate LabView program instances were used in the system design. One program was implemented in the cRIO with functions for controlling output module voltages and sampling of voltages at the input module ports. A graphical user interface for user interaction and control of the cRIO was running at a desktop computer communicating with the cRIO through a twisted-pair LAN, as shown in Figure 19.

Figure 20 depicts the second program, which was run completely on the desktop computer and had functions for grabbing the output data from the previous program and writing it to a local file. These files constituted the raw test data from the system.

Figure 19.   Block Diagram of LabView Application Running on cRIO Real-
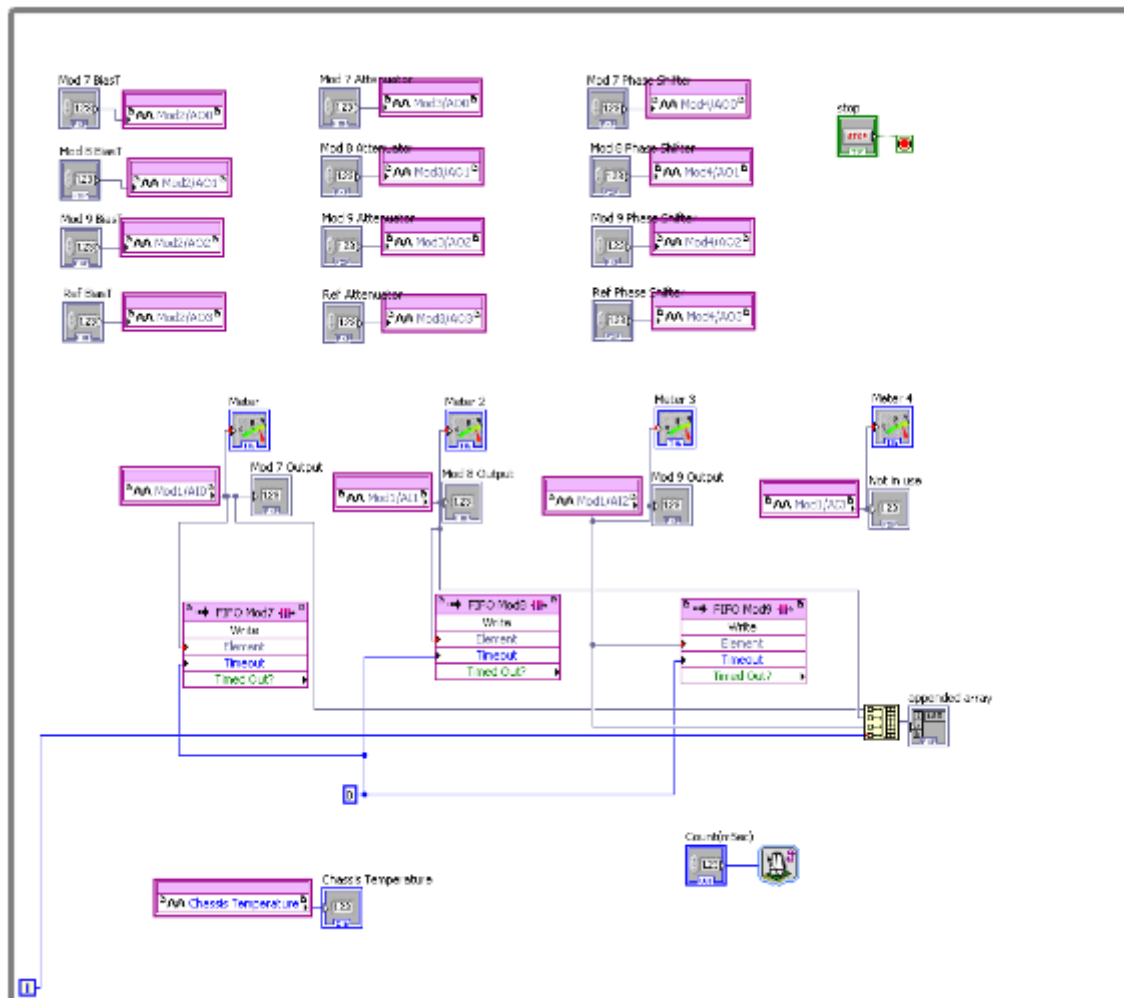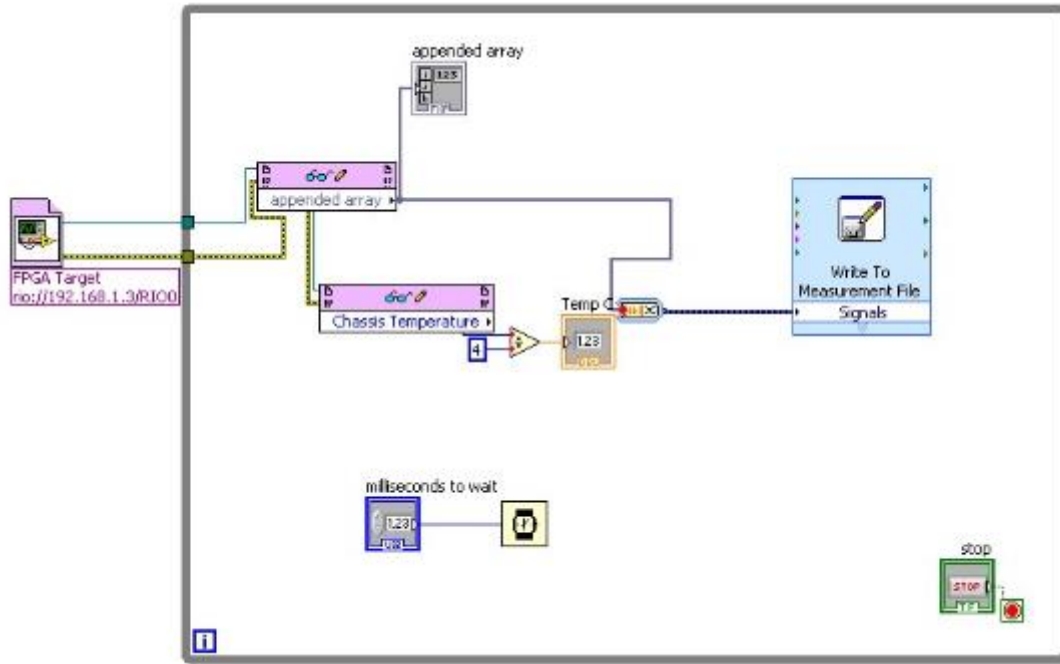Time Computer

Figure 20.   Block Diagram of LabView Application on Host Computer

G.   GAIN CALCULATIONS

Total receiver gain was calculated for best and worst insertion loss in the phase shifters. The maximum and minimum gain values were then applied a maximum attenuation in the attenuator. Results from these calculations are shown in Table 2 and Table 3. It was shown that the measurement channels had a relative gain between +8 dB and +39.5 dB, while the reference channels had a gain between −5 dB and +26.5 dB.

Table 2.   Gain Calculations for Measurement Channels (mod7, mod8, and mod9)

Component	Maximum gain	Minimum gain
LNA-2700	24	24
ZX73-2500	−5	−5
SPHSA-242	−3.5	−8
LNA-2700	24	24
Total gain	**39.5**	**35**
Max attenuated	**12,5**	**8**

Table 3.   Gain Calculations for Reference Channel

Component	Maximum gain	Minimum gain
LNA-2700	24	24
ZX73-2500	−5	−5
SPHSA-242	−3.5	−8
LPA-4-14	18	18
ZB4PD-462W	−7	−7
Total gain	**26.5**	**22**
Max attenuated	**−0.5**	**−5**

The theoretical input signal level was previously computed to −17.8 dBm. Applying the gains computed in Table 2 and Table 3 yielded the dynamic ranges for the channels shown in Table 4.

Table 4.   MZM Drive Input Power Control Range

	Minimum	Maximum
Measurement channels	−9.8 dBm (0.20 V$_{pp}$)	21.7 dBm (7.69 V$_{pp}$)
Reference channels	−22.8 dBm (46 mV$_{pp}$)	8.7 dBm (1.72 V$_{pp}$)

The values computed in Table 4 describe the MZM drive range available for the system. The moduli channels were able to drive the MZM well over V_π, and the reference channels were able to drive the MZM to about a half V_π.

This chapter described the conversion of system functionalities into physical components and some important measures to apply during the construction of the test system. The test assembly was built during the spring of 2015 and was installed in the anechoic test chamber in June 2015. In the following chapter, the test procedure and collection of test data are discussed.

THIS PAGE INTENTIONALLY LEFT BLANK

VII. TEST DESCRIPTION AND DATA COLLECTION

This chapter includes a review of the testing and data collection methods.

A. EQUIPMENT

Tests were performed at NPS in Monterey, CA. An anechoic chamber located in Spanagel Hall, Room Sp-604, was used throughout the entire test procedure, and all doors to the chamber were kept closed during each test cycle to ensure consistent signal environment and maximum shielding from potential interfering signals.

A 2.4 GHz continuous signal was generated by an HP 83711B Synthesized CW Generator with an output power of 1 dBm and amplified by an HP 8348A amplifier to 25 dBm. The signal was fed to a Tecom 201302 log-periodic antenna connected for vertical polarization.

Measurements during calibration were done with a Tektronix DSA8200 Digital Signal Analyzer containing two optical input modules (80C10B), one electrical input module (80E03), and one phase reference module (82A04-60G). Each optical module had two input ports, one for 1290–1330 nm (not used in this test) and one for 1520–1620 nm. The electrical module had two 20 GHz electrical inputs. The phase reference module was not used in this test.

B. PROCEDURE

This section describes system calibration and testing procedures.

1. System Input Verification

Theoretical system input from receiving dipole antennas was previously computed to −17.8 dBm. As shown in Figure 21, true antenna received power was slightly higher, measured to −17 dBm. This shows that previous system gain calculations in Table 2 to Table 4 were applicable and the receiver front end should have been able to operate as expected.

Figure 21.   Dipole Output Signal at 5.7m, 1 dBm Signal Generator Power
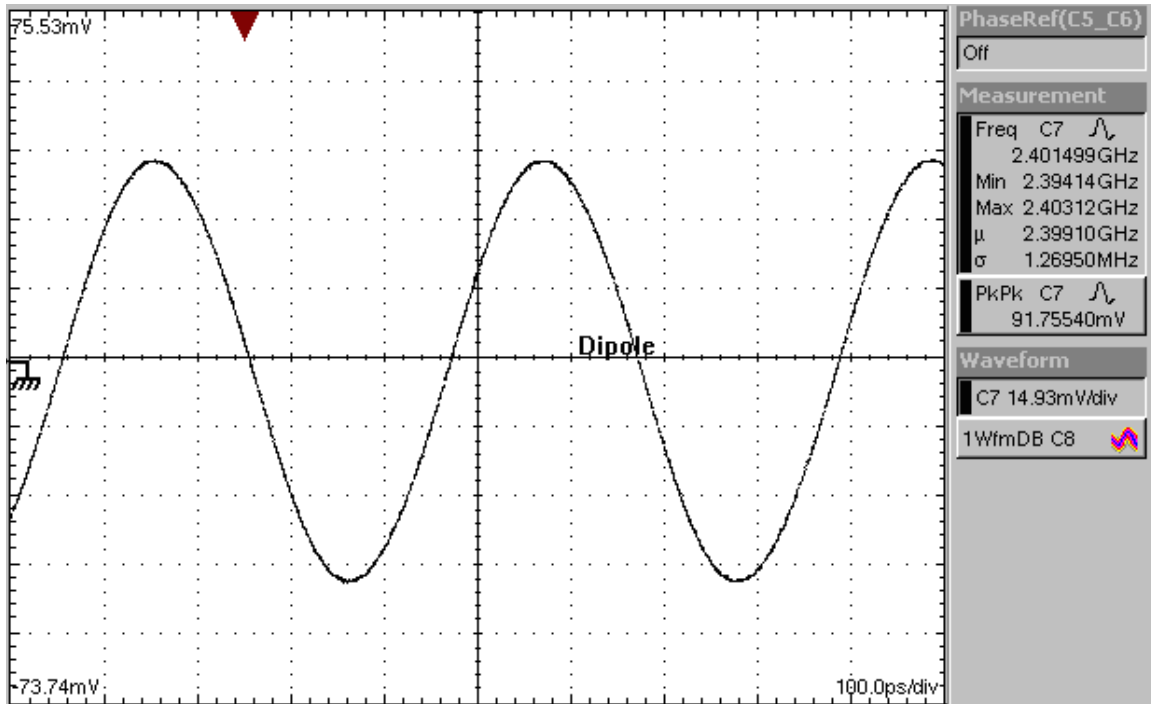
Note: Output from dipole antenna measured to 91.76 mV$_{pp}$ or −17 dBm

2.   Calibration

Identical peak-to-peak voltages on both input ports of the MZM were necessary for correct operation. With no control voltages applied to attenuators and phase shifters and all bias voltages set to 0V, MZM drive voltages typically appeared as in Figure 22.

Figure 22.   MZM Drive Signals With all Control Voltages at 0V
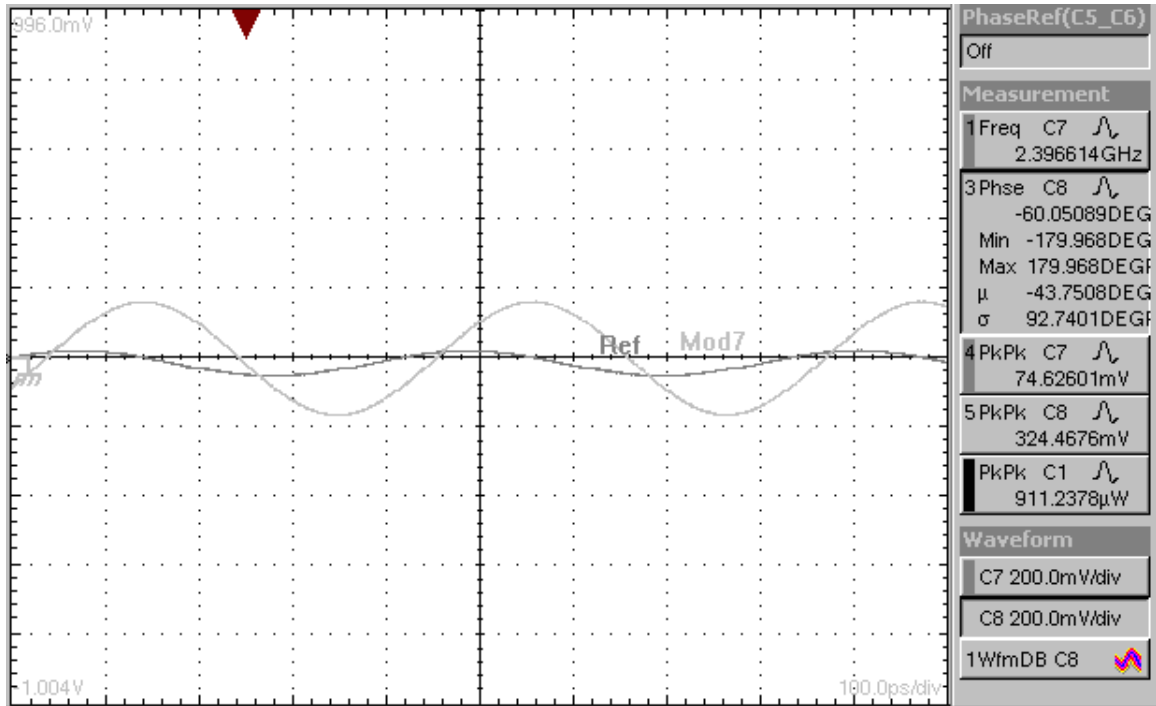
The initial step in calibrating the system was determining optimal reference channel output level. In theory, the receiver reference channel should be able to drive the MZM at 1.72 V_{pp}, but to ensure stable performance, the output was set slightly lower at 1.52 V_{pp}. This same amplitude was also used for the three measurement channels. Amplitude calibrated MZM inputs are shown in Figure 23.

Figure 23.   MZM Drive Voltage Set to Equal Amplitude
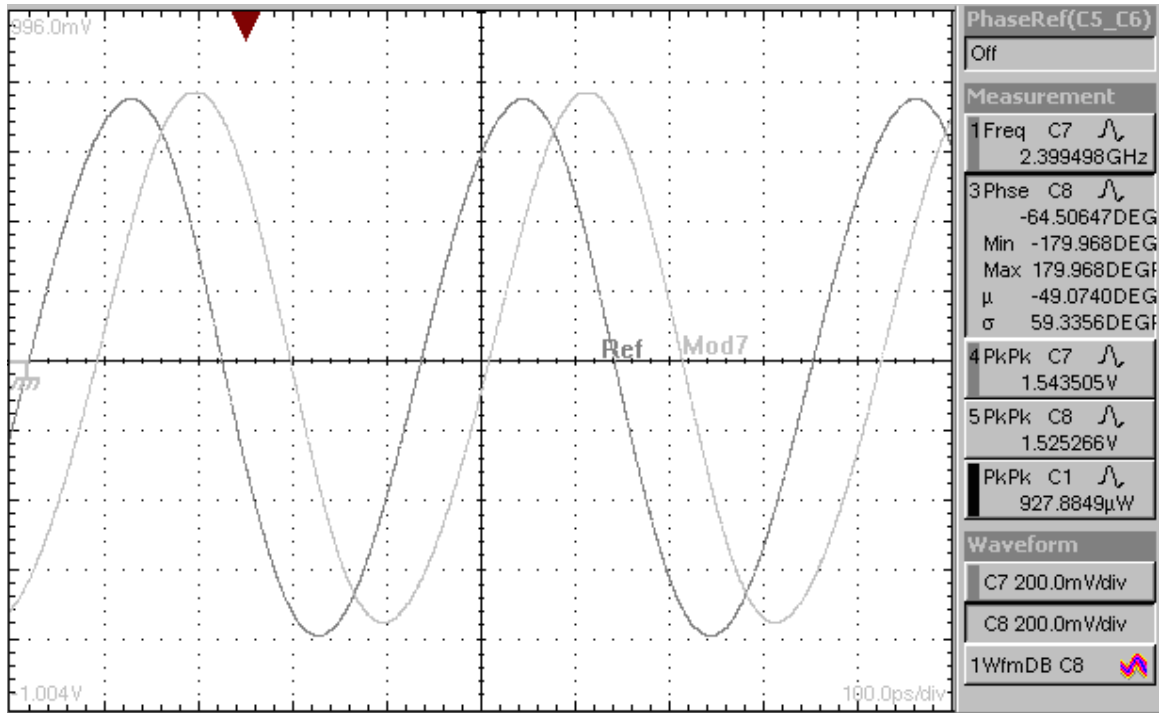
As shown in Figure 24, applying a phase change with the phase shifter also affected signal amplitude, so several iterations of increasingly smaller adjustments needed to be performed to achieve signals as shown in Figure 25.

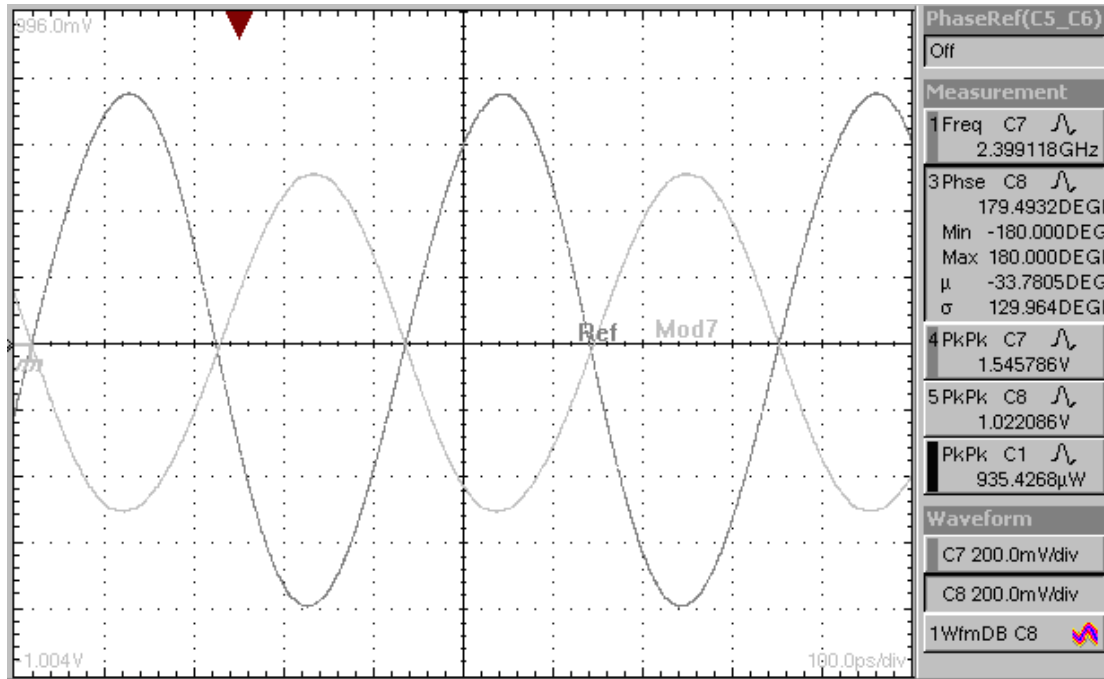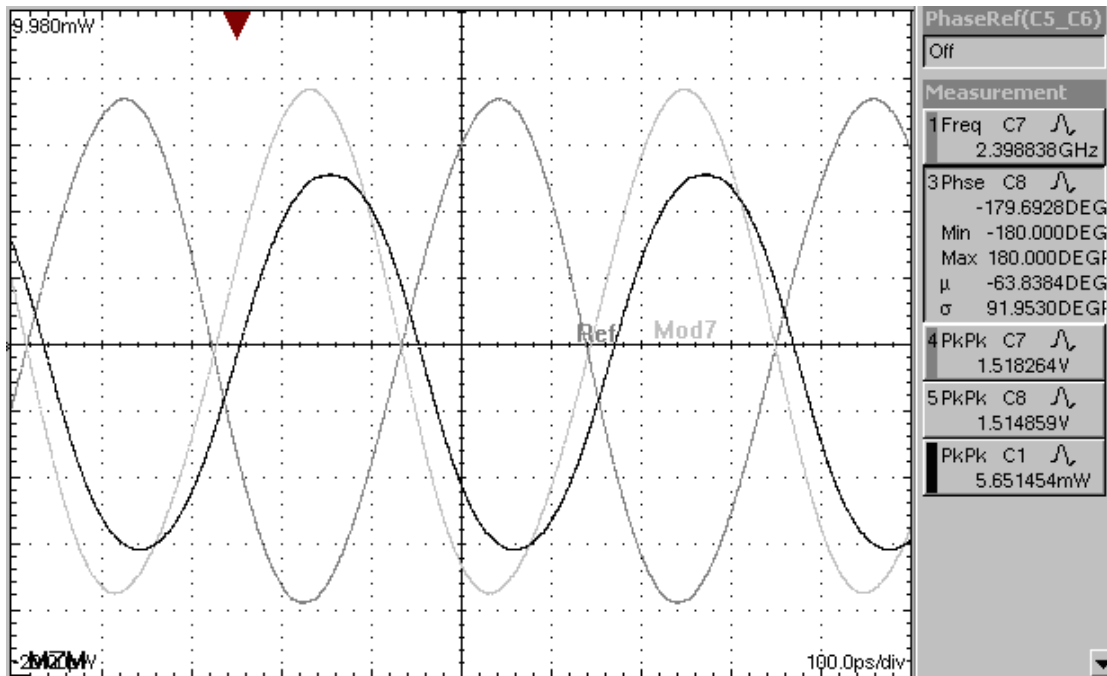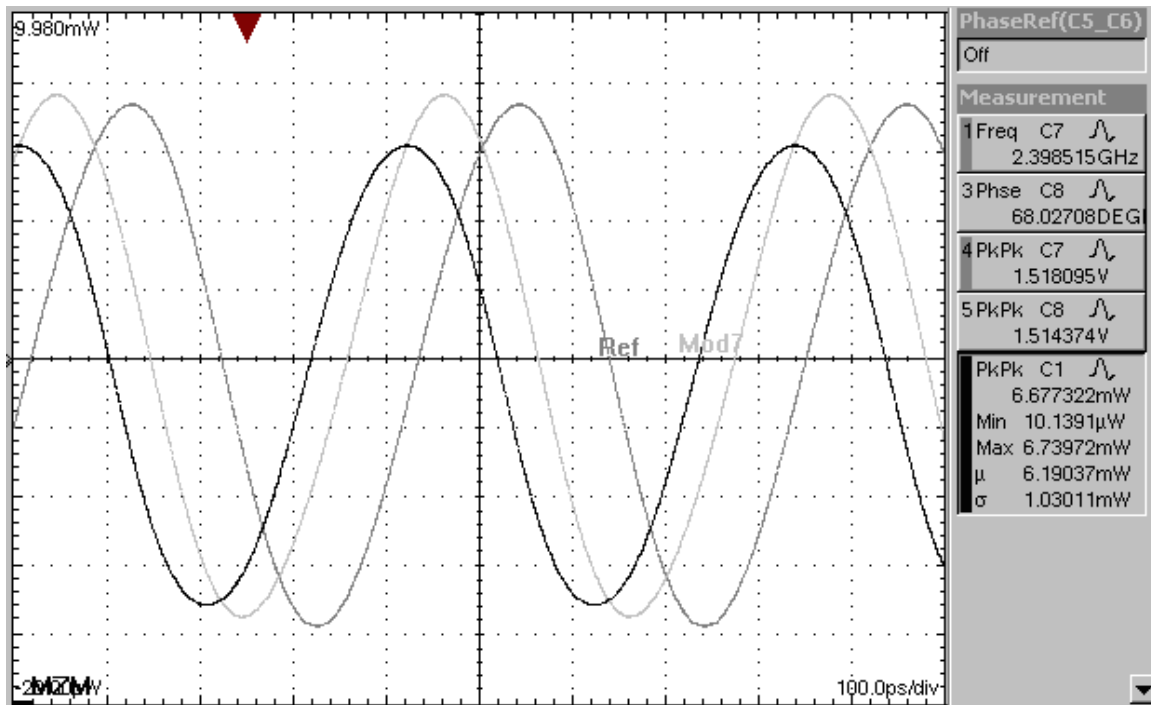Figure 24.   MZM Drive Voltages Measured Relative Phase Shift Set to 180°

Figure 25.   MZM Drive Voltages Measured Relative Phase Shift Set to 180°
and Equal Amplitude

Note: Optical output (C1) is also shown in this plot.

Since the measured phase shift was not compensated for differences in cable length, etc., true phase shift of 180° needed to be determined by finding maximum optical amplitude modulation at the MZM output. Comparing the values for C1 in Figure 25 with those in Figure 26, it is clear that the higher modulation was achieved at a different point. Measured phase shift represented a true phase shift of 180° at the MZM and could be used as a reference for computing the RSNS channel shifts for mod8 and mod9.

Figure 26.   MZM Drive Voltages True Relative Phase Shift Set to 180° and
Equal Amplitude

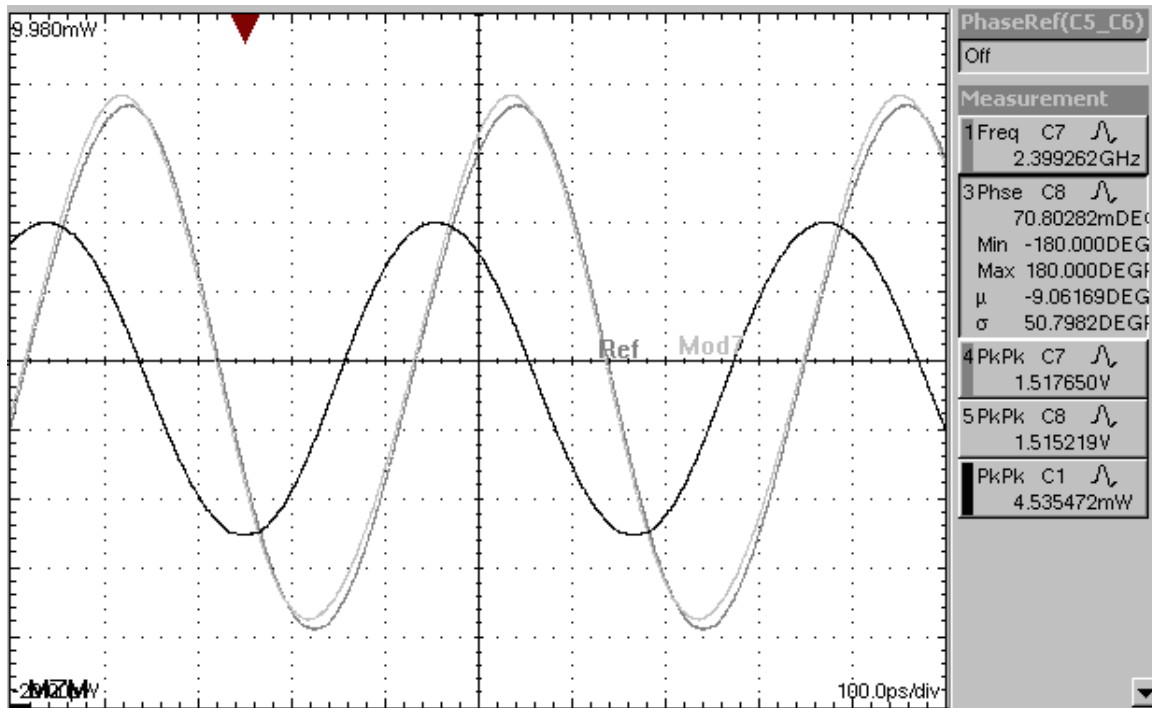Note: Maximum peak-to-peak optical output (C1) used for determining true 180° phase shift

A similar approach was used to find the true 0° phase shift between input ports of the MZM, as shown in Figure 27 and Figure 28.

Figure 27.   MZM Drive Voltages Measured Relative Phase Shift Set to 0° and
Equal Amplitude

Note: The MZM output (C1) shown in this picture had an obviously high envelope. This
envelope should be minimal for true 0° phase shift between input ports since the MZM is
designed for complementary drive.

Figure 28.   MZM Drive Voltages True Relative Phase Shift Set to 0° and
Equal Amplitude
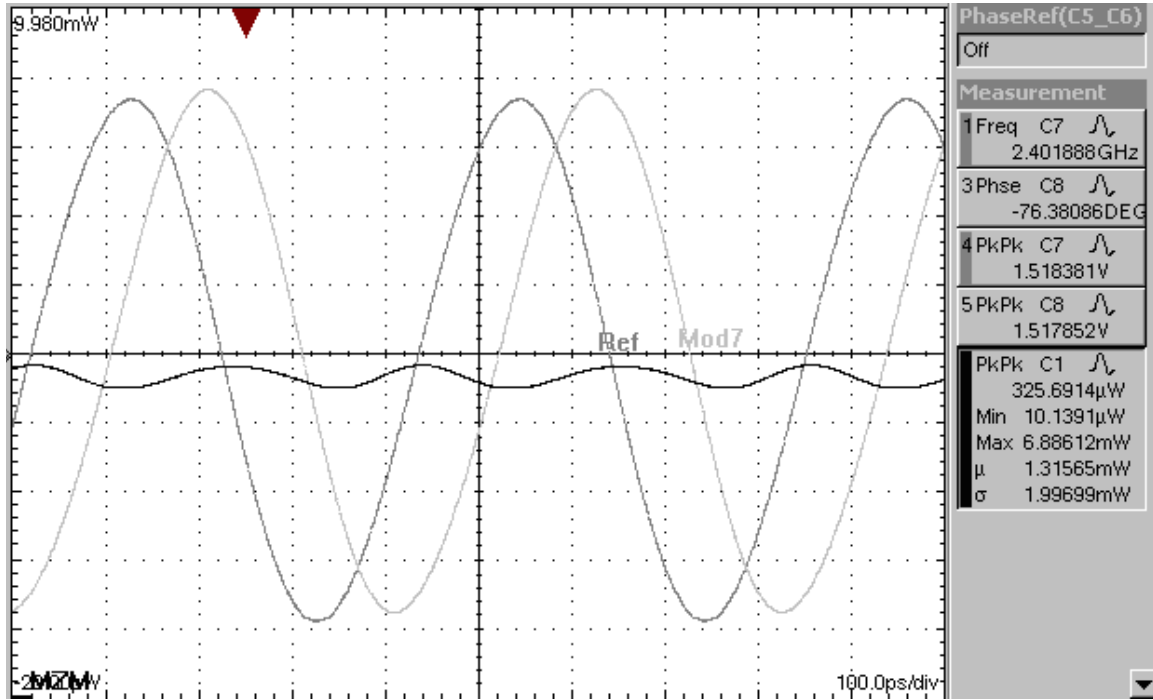
Note: Minimum peak-to-peak optical output (C1) used for determining true 0° phase shift

In order to avoid the signal from modulating the MZM around its maximum or minimum transmission point as shown in Figure 29, each MZM was biased in between the maximum and minimum transmission point.

Figure 29.   Example of Ill-Biased System, True Phase Difference 180°
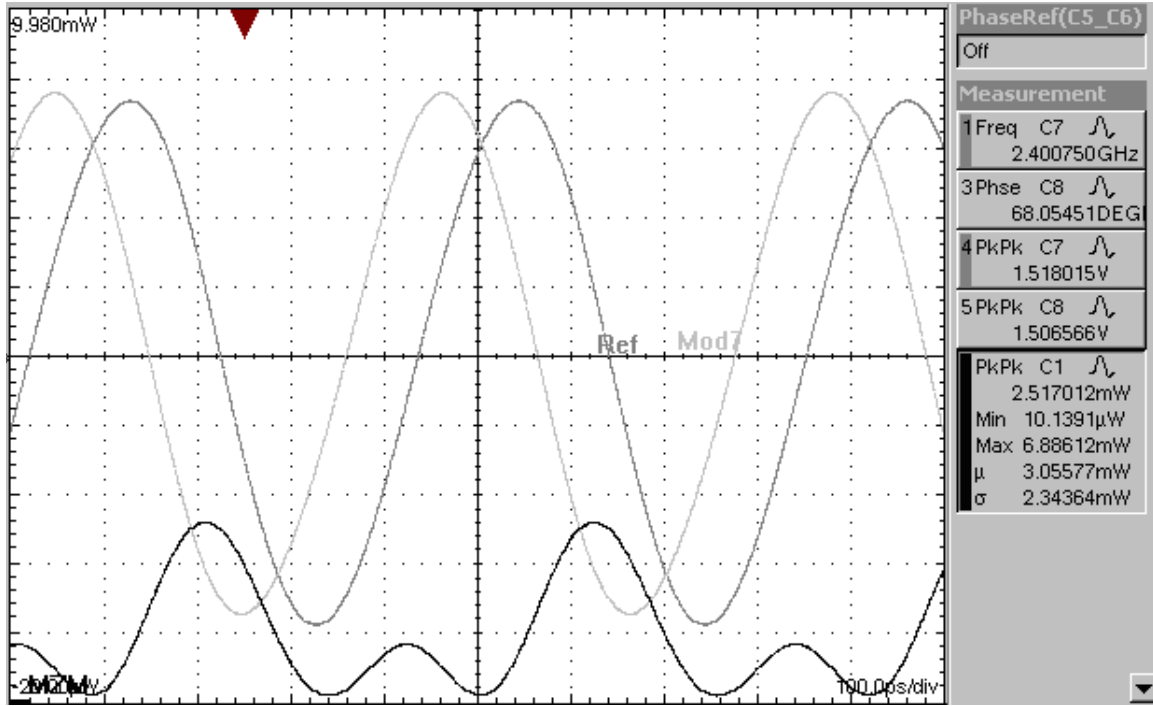
Note: The plot shows distorted output intensity due to input signals driving the MZM
over V_π.

Once the reference points for 0° and 180° phase shifts were established, the mod8
and mod9 channels were adjusted to align their phase shifts with the RSNS code [22] as

$$m_7 = 0°$$
$$m_8 = -52.5°$$
$$m_9 = -293.33°$$

The last step of calibrating the system consisted of setting the output
instrumentation amplifier to deliver a maximum signal output amplitude of about 8V.

3.   Test Procedure

All data were gathered from the inputs of the cRIO and transferred to tab-
separated text files using a separate LabView program running on a PC. The cRIO and
the computer were interconnected through a small, wired Internet protocol network. The
complete setup is shown in Figures 30 and 31.

Figure 30.   Assembled System as Used During Testing
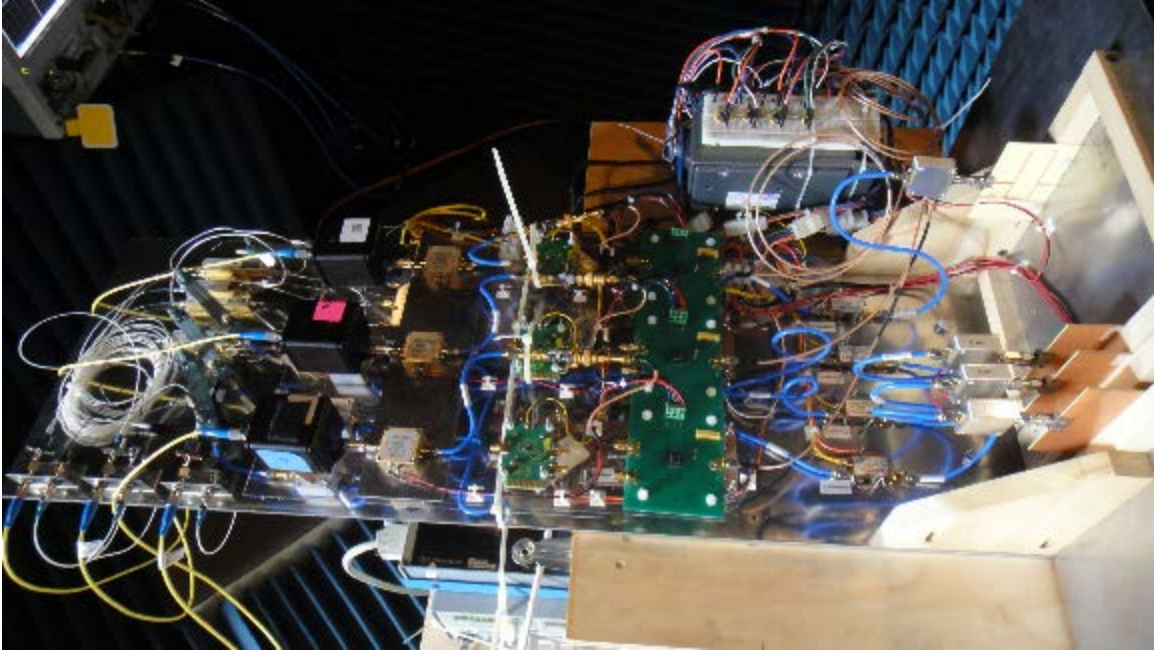


Two procedures for generating data were used: stepped and continuous. Stepped data were gathered over antenna sweeps from −90° to +90° in 1° increments. The sampling speed of the training data was set to 10 Hz and with an approximate dwell time per step of 3.5 seconds, generating about 30 samples per angle increment.

Recording of continuous data was done over antenna sweeps between −90° and +90° and was sampled at 1000 Hz. The higher sampling rate was necessary due to the fact that the antenna sweep speed was not configurable, where one full sweep took in the order of 1–2 seconds. These sweeps were performed in both directions (+90° to −90° and −90° to +90°), and 10 such sweeps were recorded in each data file.

Figure 31.   System in Test Chamber, DOA 0°
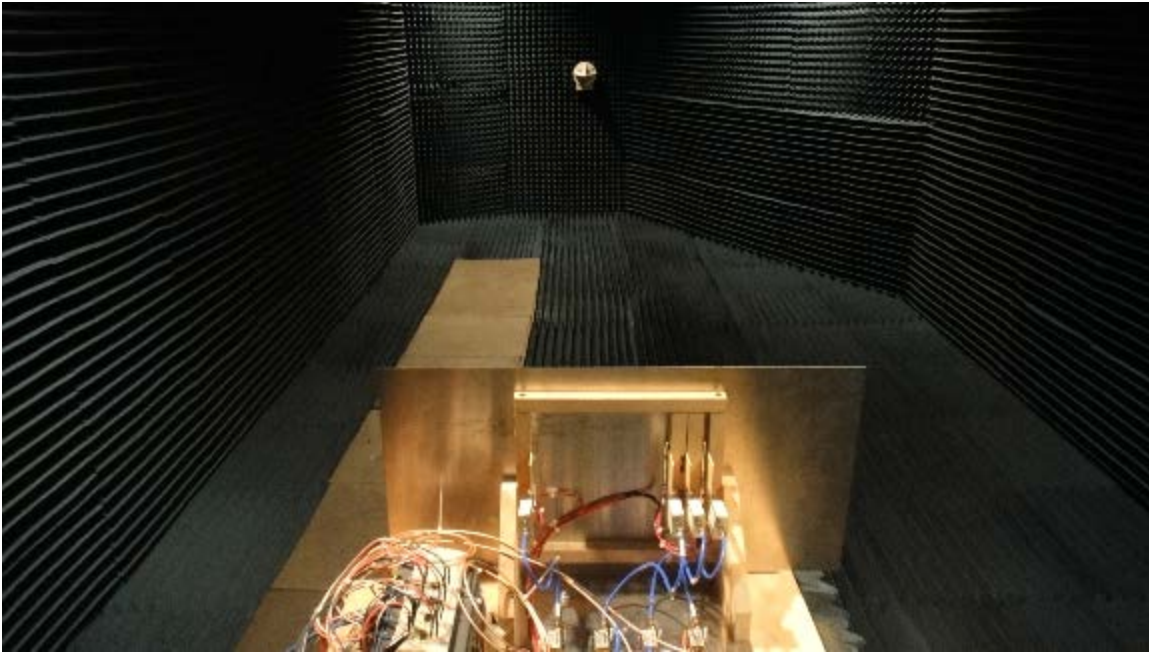
C.   DATA

This section describes how test data were gathered during anechoic testing.

1.   Reference Data

Due to the construction of the test chamber, true pedestal angle outputs were not available. The only reference data available for the measurements were the outer limits for pedestal movement; −90° and +90°. The incremental stepping in 1° steps when gathering data made it possible to map measurements to a reference angle by resolving these steps.

2.   System Output Data

As described previously, data for two distinct types of antenna sweep patterns, stepped and continuous, were gathered. The stepped data were collected for 181 steps, representing 1° increments from −90° to +90°, and the total test cycle lasted for approximately 10–15 minutes and generated 6000–7000 data points per cycle. An example of the stepped output data is shown in Figure 32.

Figure 32.   Example Training Data
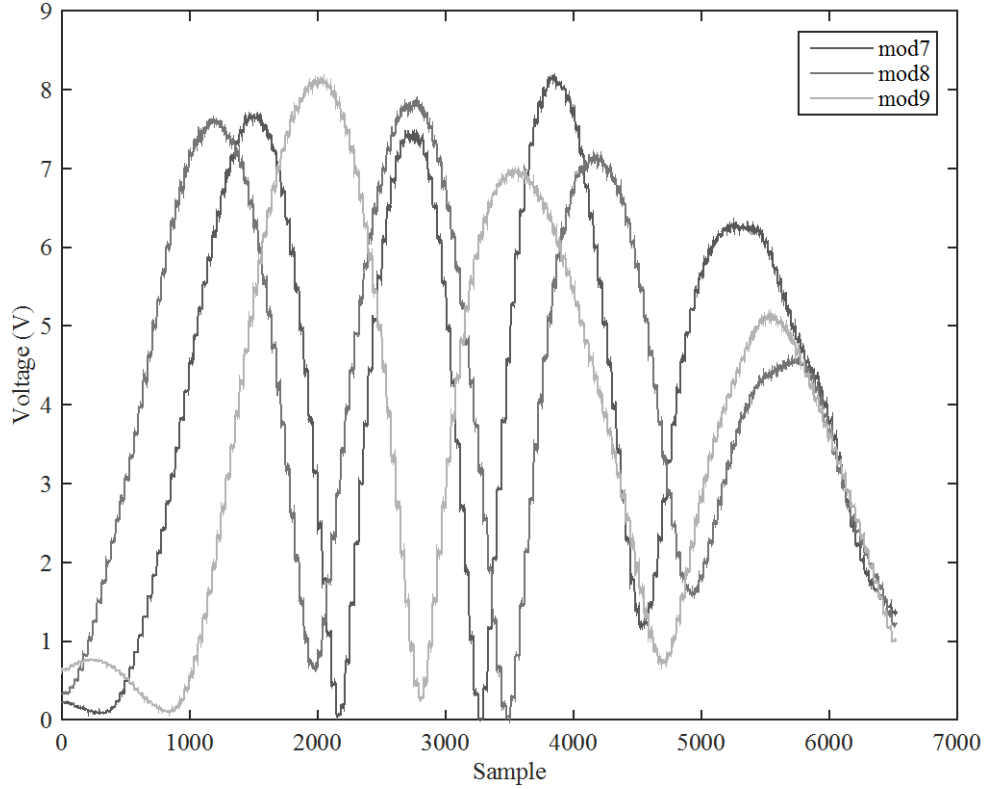
These stepped data were collected primarily for testing the RSNS-to-DOA approach described by [23], but were also found to be very useful for training an MLP for determining DOA, as described later. For the RSNS case, the reason for stepping was to be able to determine true DOA as described previously through mapping of steps over the full 180° antenna sweep, as shown in Figure 33.

Continuous data were gathered in order to investigate RSNS performance and possibilities to apply an interpolating approach to RSNS-to-DOA, but these data were instead used for testing performance of the MLPs.

Figure 33.   Example of Test Data for One Antenna Sweep
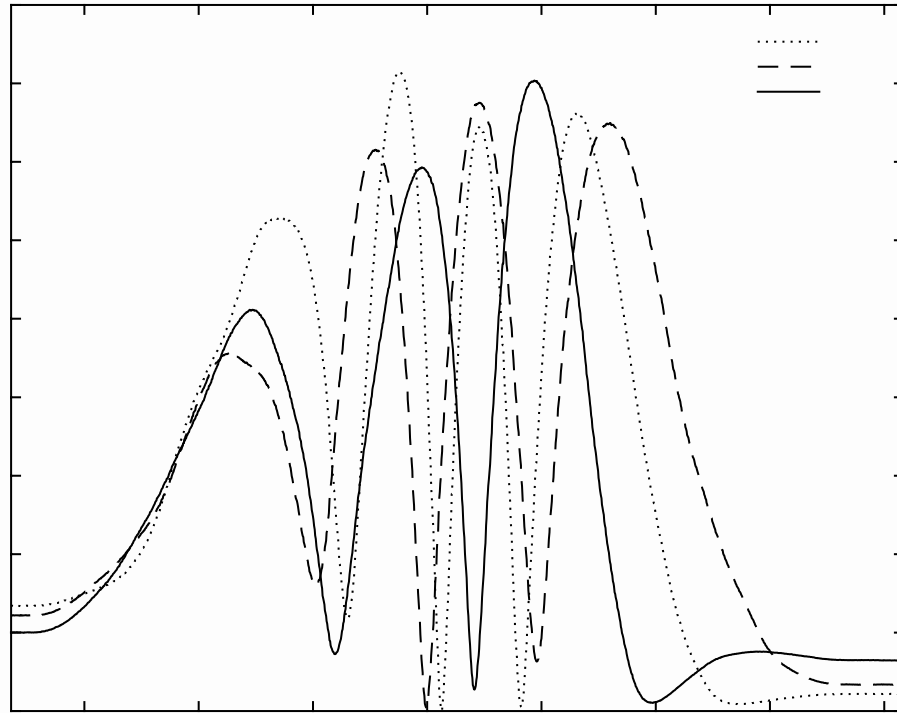
Since the RSNS code is inherently amplitude sensitive, the recorded data needed to be preprocessed in order to compensate for the different peak values. For the RSNS code to work properly, all peaks in the individual moduli channels needed to be adjusted to have the same amplitude. Since signal amplitude depended on DOA, each channel was individually processed by interpolating the peak values over the entire data set and using the interpolated values for normalization of the channel at each time sample. An example of resulting normalized channel output is depicted in Figure 34.

Figure 34.　Example of Normalization of Recorded Test Data
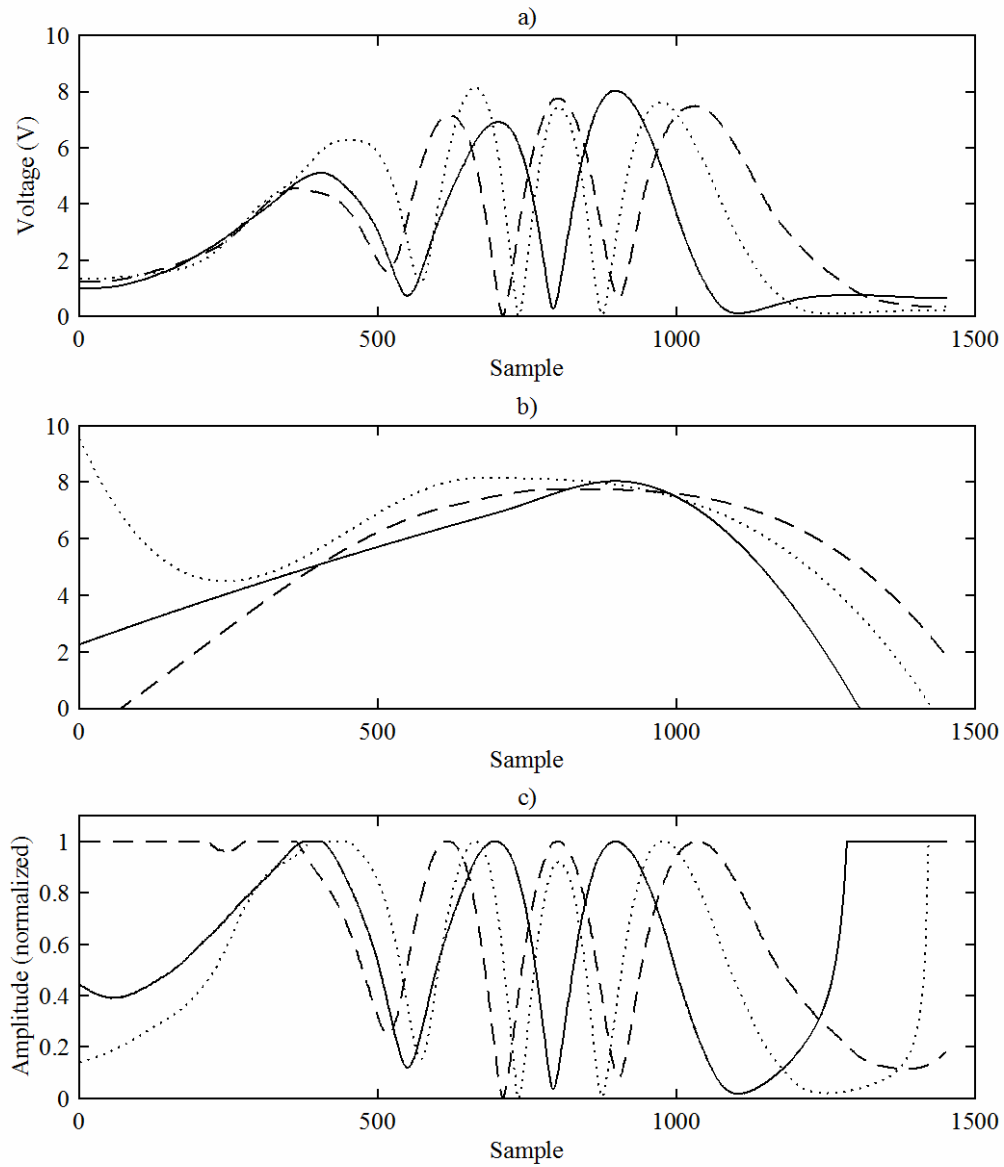
Note: a) Recorded test data from one antenna sweep, b) computed normalization
coefficients, and c) normalized test data

As shown in Figure 34, the attempted normalization procedure failed to fully
compensate for the varying peak amplitudes but greatly improved the peak amplitude

uniformity in all channels. This had implications on the conversion from sampled raw data to RSNS coded data as discussed in the following section.

3.   RSNS Thresholding

The normalized raw data were converted to RSNS coded data through thresholding, emulating the comparators in the RSNS-to-DOA design in [23]. Values for RSNS thresholds were calculated after [23] as

$$T(k,m_i) = \cos^2\left[\frac{\pi}{2} - \left(\frac{\pi(kN+1)}{2Nm_i} + \frac{\pi}{4Nm_i}\right)\right] \tag{8}$$

where m_i is the moduli for the channel, $k = 0, 1, \ldots, m_i - 1$, and N is the total number of channels in the RSNS system. In Figure 35, it is shown how the attempted RSNS code after thresholding appears to resemble an RSNS sequence. The RSNS sequence in the center part of the mentioned figure should be identical to what is shown in Figure 79. Left and right flanks in Figure 35 should be different since the RSNS code is only expected to be useful for $\pm 60°$, but the center part should be identical for the RSNS decoding of DOA to work.

Figure 35.   Attempted Reconstruction of RSNS Sequence
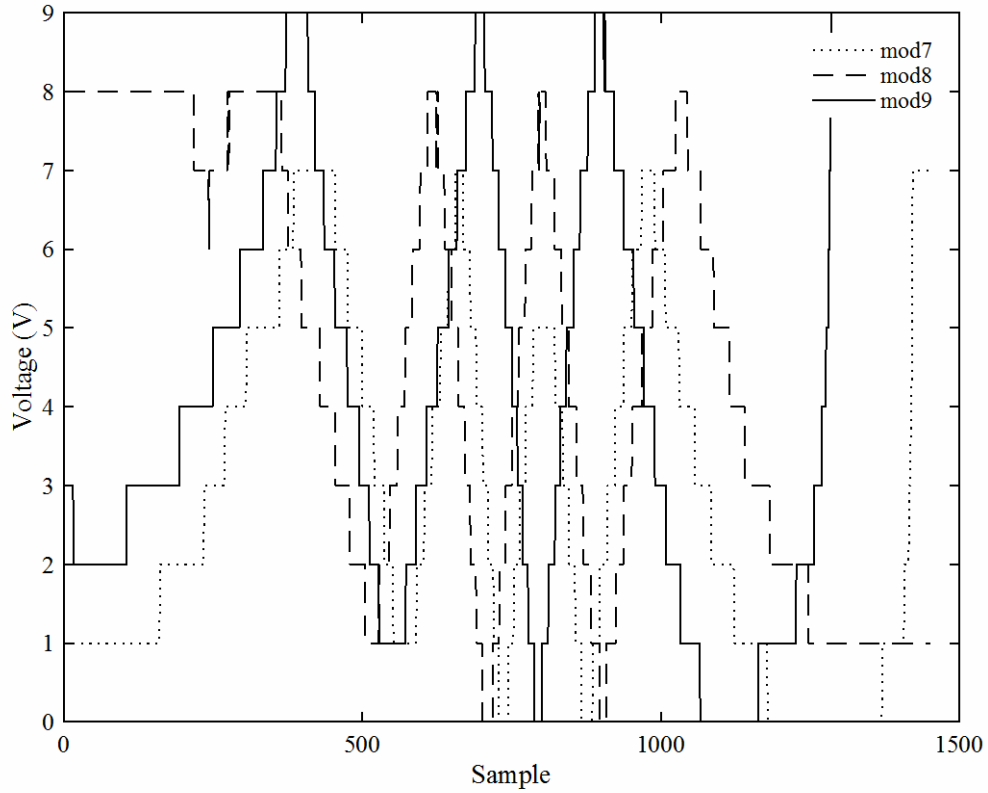
However, the relatively small difference in the upper thresholds combined with previously described signal amplitude instability and variations with DOA resulted in errors in the attempted RSNS output and prevented proper interpretation of the RSNS code. Several attempts to recalibrate the system were made, but the behavior was found to be unrelated to calibration and rather to the previously discussed DOA-dependent amplitude variations. It should also be noted that the compensation for different peak amplitude was done as a function of DOA. This can be done when DOA is known during calibration, but when the equipment operates as a DOA measuring system, this angle is the unknown variable. This makes the RSNS approach infeasible to apply in a real environment since the compensation factor will never be known.

Comparing the resolution in Figure 33 and Figure 35 revealed that much of the high-resolution information in the first figure was lost in the conversion to the lower

resolution of the latter one. This fact initiated another approach to resolve DOA from the raw data: the use of pattern recognition by employing MLPs.

D.   NEURAL NETWORK

Resolving DOA from the combination of the states of the three measurement channels can be approached in several ways, either as a classification problem similar to pattern recognition or as a regression problem. The classification approach classifies a specific combination of input values to belong to a certain class, in this case a discrete representation of DOA. An MLP for regression analysis was tentatively tried in the initial design of the data processing, but was deemed unfit due to performance problems.

1.   MLP Structuring

Experience from previous work on similar classification problems suggested that the numerical DOA values needed to be translated into a unary code representing discrete angles. The angular resolution of the system is determined by the resolution of the unary code used, which in turn is based on the properties of the training data. For this system, a resolution of $1°$ was chosen to demonstrate the functionality, and numeric angular values were represented by a string of 181 bits as

$$-90° = \{100000...0\}$$
$$-89° = \{010000...0\}$$
$$-88° = \{001000...0\}$$
$$\vdots$$
$$88° = \{0...000100\}$$
$$89° = \{0...000010\}$$
$$90° = \{0...000001\}$$

Using the neural pattern recognition app in MATLAB, several different network structures were tentatively tested in an attempt to find the least complex network that still had acceptable performance. Vectors can be sufficiently well classified using a two-layer feed-forward network with tan-sigmoid hidden and softmax output neurons if the hidden

layer consists of a sufficient amount of neurons. A constructive approach was used to find that a hidden layer with 90 neurons had acceptable training time and reasonable performance, as shown in Figure 36. An increased number of neurons generally improves convergence, but too many may result in overfitting and poor performance. The network was trained with scaled conjugate gradient backpropagation.

Figure 36.   Two-Layer MLP Used for DOA Estimation
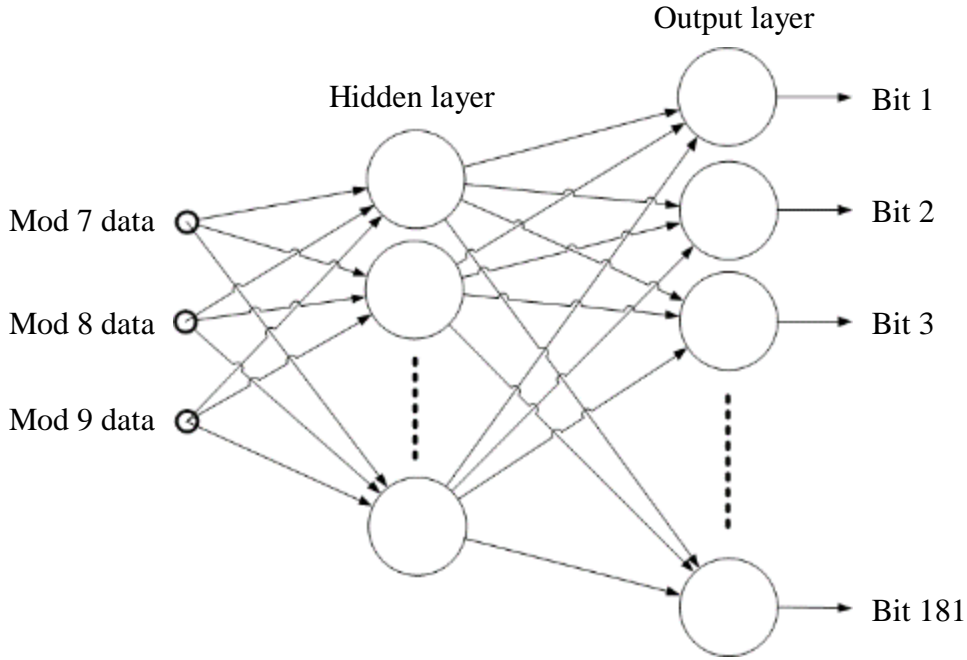
Outputs y_i^t for $i = \{1, 2, ..., 181\}$ from the network were determined using softmax

$$y_i^t = \frac{\exp o_i^t}{\sum \exp o_i^t}$$

(9)

where the outputs o_i^t from the output layer to the softmax function were calculated as

$$o_i^t = \sum_{h=1}^{90} v_{ih} z_h^t + v_{i0}$$

(10)

70

in which v_{ih} are the individual weights, v_{i0} are the bias units, and z_h^t are the outputs from the hidden layer. These two functions were considered to constitute a single layer. Outputs from the hidden layer can be denoted as

$$z_h = sigmoid\left(\sum_{j=1}^{3} w_{hj} x_j + w_{h0} \right)$$ (11)

for $h = \{1, 2, ..., 90\}$ using weights w_{hj} with inputs x_j and adding bias units w_{h0}. In this case, the sigmoid function used was tan-sigmoid:

$$sigmoid(n) = \frac{2}{1 + \exp(-2n)} - 1$$ (12)

The softmax function generates posterior probabilities for selection, and the output with the highest posterior probability was set to one while all other outputs were set to zero.

2. Data Pre-processing

As previously described, training data consisted of time samples of each of the outputs from the photonic receiver. The data were imported to MATLAB and saved as a $Q \times 3$ matrix where each row represented one time sample and the columns represented the individual receiver outputs.

Since no true pedestal angle data were available, the discrete angles had to be determined from the data itself. The data recorded during antenna movement had to be removed, since the network needed to be trained only with data for which there existed a target value for comparison. During antenna movement, the exact antenna angle was not known. Training data preparation was done in three steps:

- Detection of approximate transition between discrete angle increments

- Removal of data points during antenna transition

- Detection of exact angle increment timing

Absolute differences in amplitude between adjacent time samples for each channel were computed and summed. Through peak detection, the location of these transitions could be determined, and sample data during transitions, as shown in Figure

71

37, was removed. Once the data were cleaned of inconsistencies, another iteration of difference summing and peak detection was performed and the corresponding angles labeled to the data. Output from the preparation was a $Q' \times 4$ matrix, where $Q' < Q$ since transition data was removed and the fourth column represented true DOA.

Figure 37.   Example of Intermediate Data Points During Antenna Movement
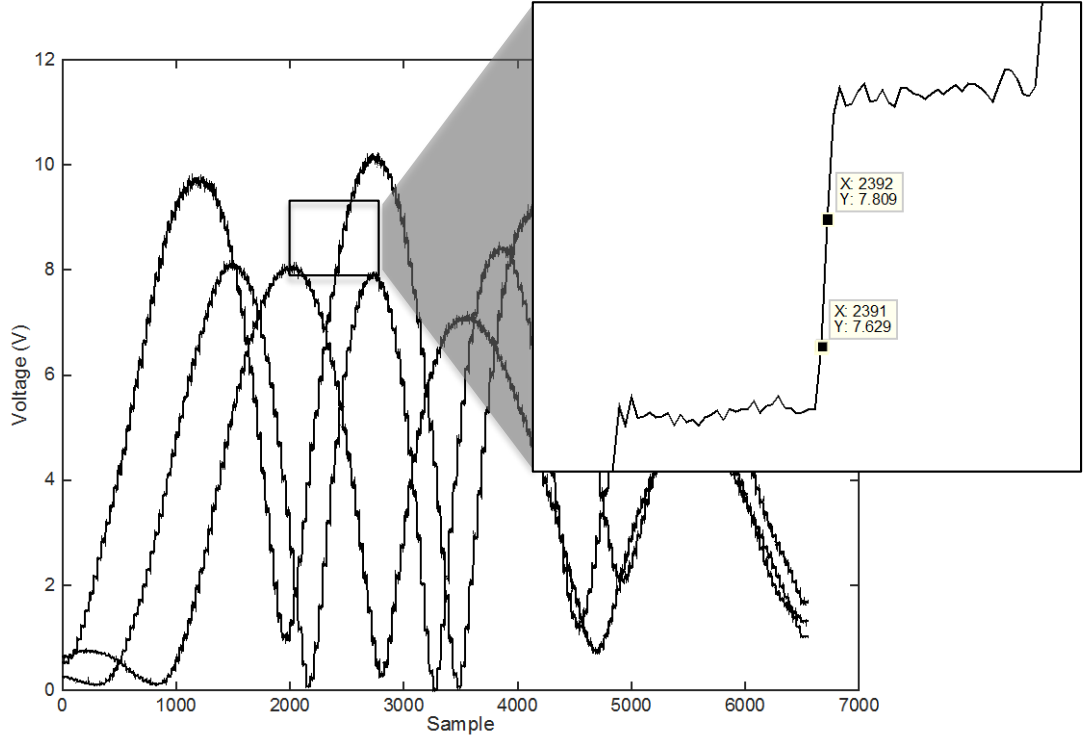
The next step was to adapt the DOA data to a 181-bit unary coding. For ease of programming and training of the network, the $Q' \times 181$ matrix representing DOA was separated from the $Q' \times 3$ matrix representing time samples of voltage outputs from the receiver. These two matrices were used as input and target for the training of the MLP, and training performance was recorded. Training was done using 64-bit MATLAB R2014b in MacOS X 10.10.5 on a 2010 MacBook Pro with Intel Core i7 processor at 2.66 GHz and 8 GB of 1067 MHz DDR3 RAM. The trained networks were stored as MATLAB matrix-only functions in order to be able to apply the networks to test data for performance evaluation.

3.   Data Post-processing

Recorded test data were imported in MATLAB and saved as an $R \times 3$ matrix with each row representing a time sample and the columns representing each of the receiver outputs. Each data set contained 10 continuous full antenna sweeps in each direction. The previously trained networks were applied to each test data set and the resulting $R \times 181$ matrix was converted to a $R \times 1$ vector containing the numerical representations of the angular outputs from the network.

Since there was no true DOA data to compare the output to, the pedestal angle was interpolated from the angle classification results from the network. Because of this approach, the computed errors were not fully comparable to true DOA but were well suited for comparison of performance between different data sets in this system.

The test procedure, gathering of test data, and formatting of these data were described in this chapter. These methods were employed on the system mounted in the anechoic chamber at NPS during July and August 2015, and the results are discussed in the following chapter.

THIS PAGE INTENTIONALLY LEFT BLANK

VIII. EXPERIMENTAL TESTING RESULTS

This chapter contains results from experimental testing in the anechoic chamber with data processed as described in Chapter VII.

A.   NETWORK TRAINING

Networks were trained for a maximum of 1000 iterations until either the validation error was 0 or the gradient of improvement became less than 1×10^{-6}. Training statistics for all networks except the unaligned system are listed in Table 5. Training time and resulting validation error was approximately the same for the unaligned system, but unfortunately were never documented.

Table 5.   MLP Training Statistics

Dataset	Training time (s)	Number of iterations	Validation error
04AUG	196	231	0.91×10^{-6}
05AUG network1	284	332	1.51×10^{-6}
05AUG network2	412	401	2.82×10^{-6}
06AUG network1	281	309	1.44×10^{-6}
06AUG network2	215	261	1.84×10^{-6}

Note: Training was stopped due to a gradient of improvement below 1×10^{-6} in all cases.

The differences in training time may be related to the quality of the training data. By inspection, some of the training data sets appeared slightly noisier than others, and this might have been the reason for the differing number of iterations needed to achieve necessary network performance. Using a faster computer for training should reduce the training time considerably.

B.   TRAINING DATA AND TEST DATA FROM SAME DAY

This section contains results from test data and networks trained on data recorded within one or a few hours of each other, as shown in Figures 38–62. Results show how the system performed when fairly recently bias calibrated and trained. The complete output consisted of results for 20 continuous antenna sweeps, 10 in either direction. For each test set, one antenna sweep in either direction was further analyzed. Sweeps analyzed in detail were those considered worst cases; this was done in order to determine maximum angle error for the system.

Each test result consisted of five plots, the first showing the full resulting dataset, the second and third showing performance for a positive antenna sweep, and the fourth and fifth showing performance for a negative antenna sweep. As described earlier, true DOA was not available but interpolated. Residues with errors greater than 10° were considered as outliers and removed from mean error calculations. The number of removed outliers and absolute mean error is shown in each residue plot, and these outliers are shown as circles in the curve fit plots. A total number of 1310 samples were used for each detailed analysis.
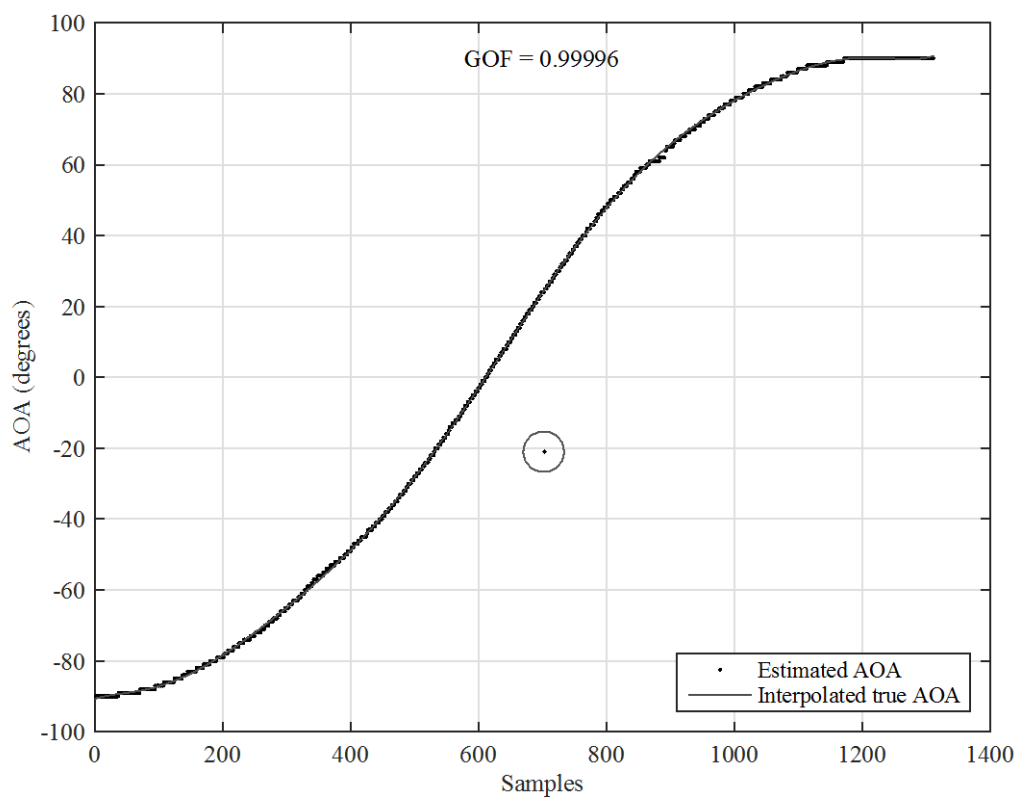
Figure 38.   Complete Network Output Data for 10 Continuous Antenna
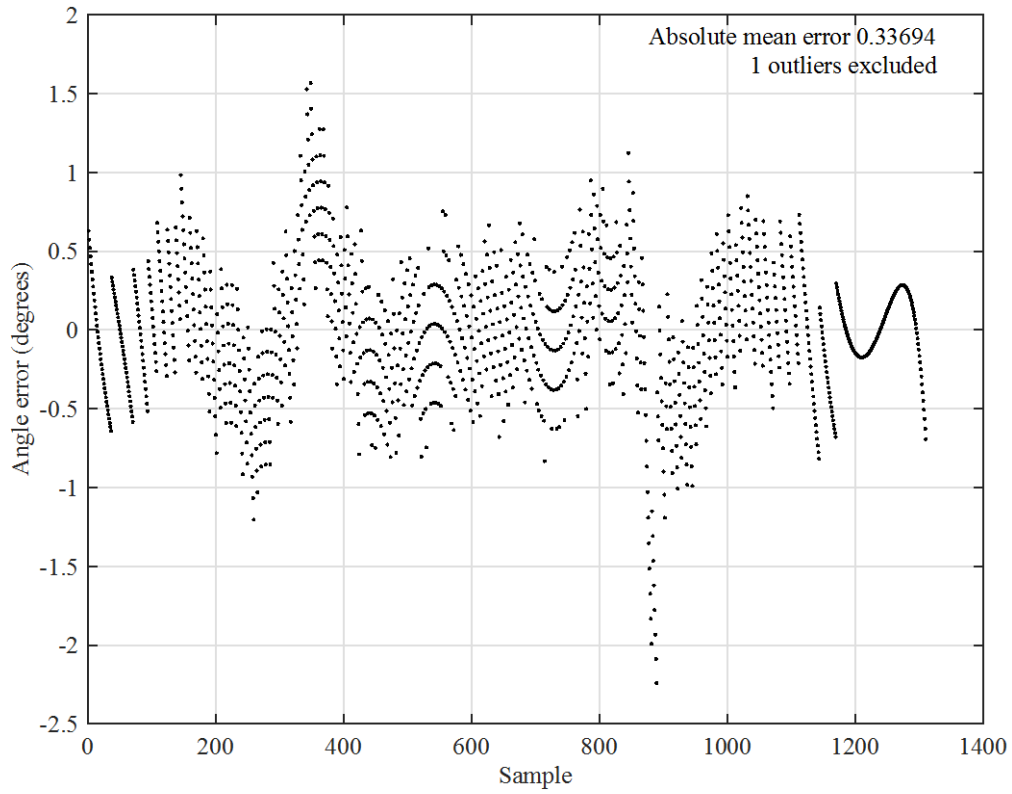Sweeps in Both Directions, Aug. 4, 2015
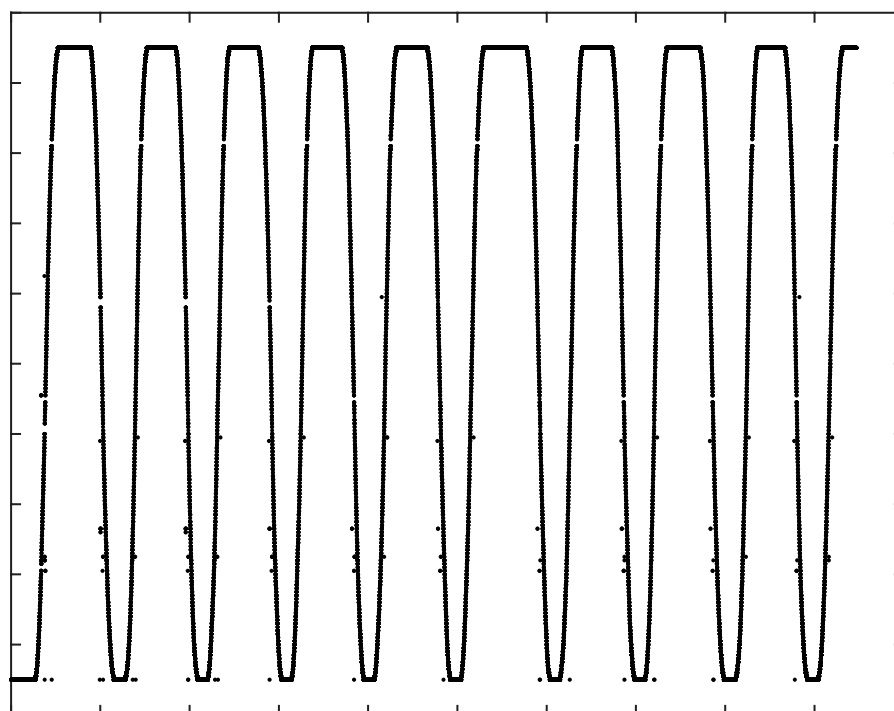
Note: Test data recorded Aug. 4, 2015, analyzed in network trained with data recorded
Aug. 4, 2015

Figure 39.   Curve Fit of One Positive Antenna Sweep (−90° – +90°), Aug. 4, 2015

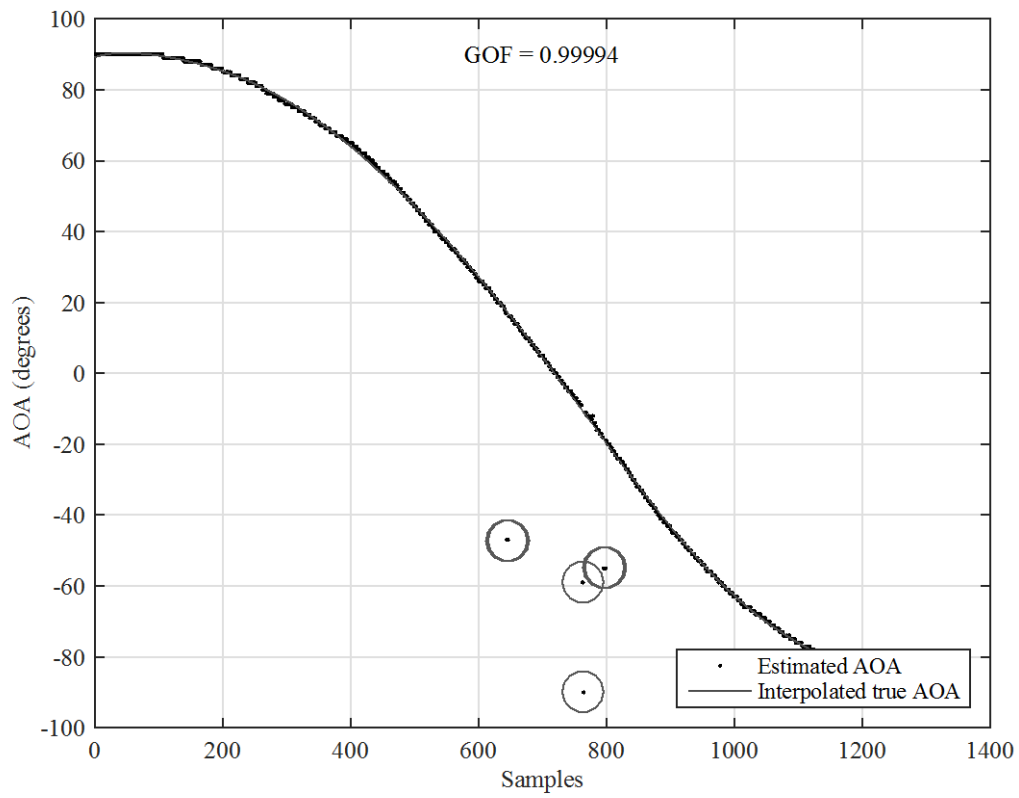Note: Test data recorded Aug. 4, 2015, analyzed in network trained with data recorded Aug. 4, 2015

Figure 40.   Residues for One Positive Antenna Sweep ($-90°$ – $+90°$), Aug. 4, 2015

Note: Test data recorded Aug. 4, 2015, analyzed in network trained with data recorded
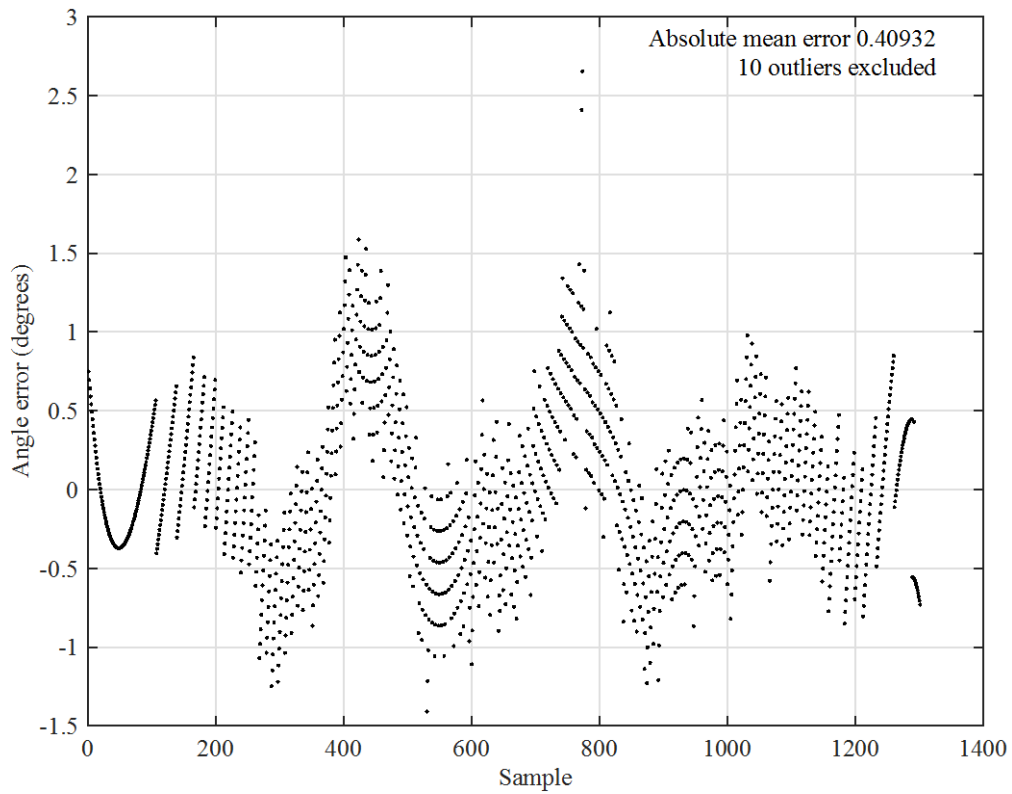Aug. 4, 2015. Curve fitted to estimate true DOA.

Misclassification was detected in one sample out of 1310 total samples, yielding a misclassification rate of 7.6336×10^{-4}. The mean angle error after this outlier was removed was computed to $0.33694°$.

Figure 41.   Curve Fit of One Negative Antenna Sweep (+90° – −90°), Aug. 4, 2015

Note: Test data recorded Aug. 4, 2015, analyzed in network trained with data recorded Aug. 4, 2015
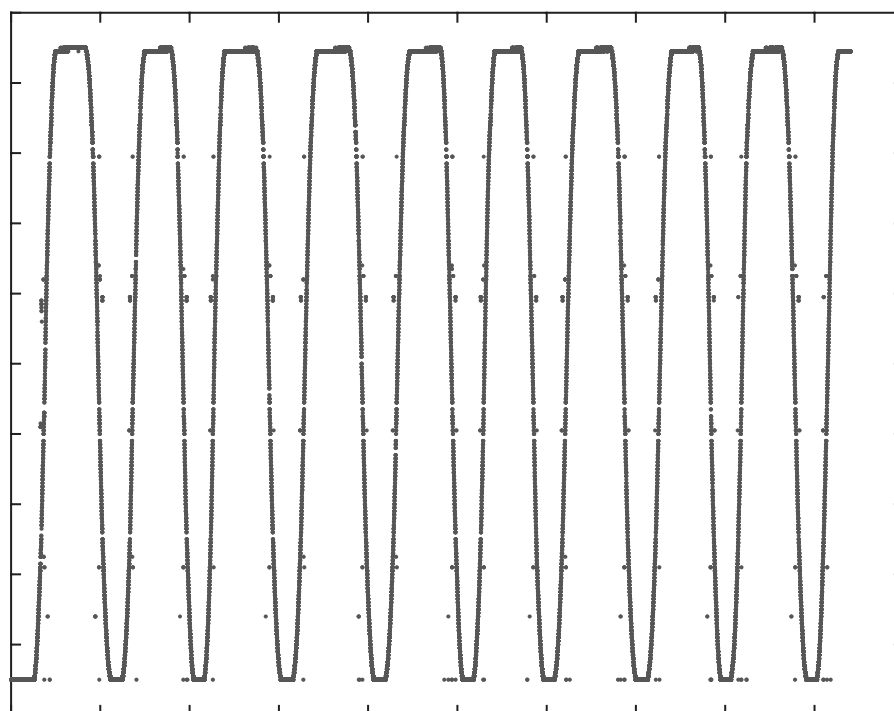
Figure 42.   Residues for One Negative Antenna Sweep (+90° – −90°), Aug. 4, 2015

Note: Test data recorded Aug. 4, 2015, analyzed in network trained with data recorded Aug. 4, 2015. Curve fitted to estimate true DOA.

Misclassification was detected in 10 samples out of 1310 total samples, yielding a misclassification rate of 0.0076. The mean angle error after these outliers were removed was computed to 0.40932°.

Figure 43. Complete Network Output Data for 10 Continuous Antenna
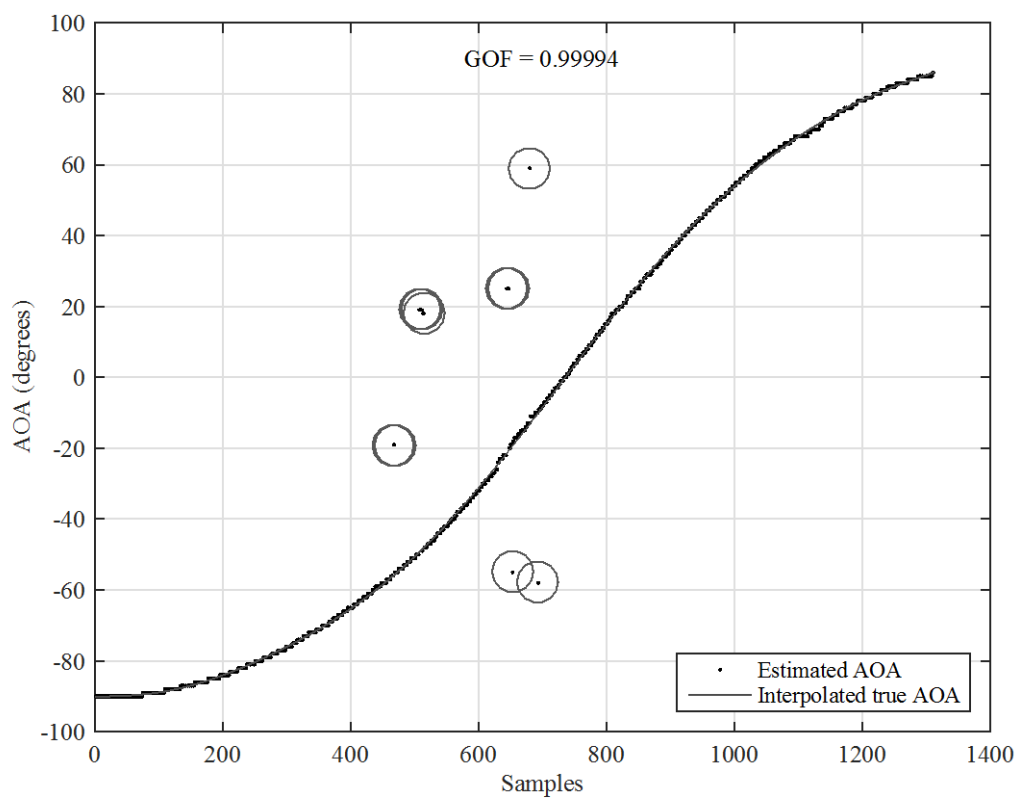Sweeps in Both Directions, Aug. 5, 2015 (network 1)

Note: Test data recorded Aug. 5, 2015, analyzed in network trained with data recorded
Aug. 5, 2015 (network 1)
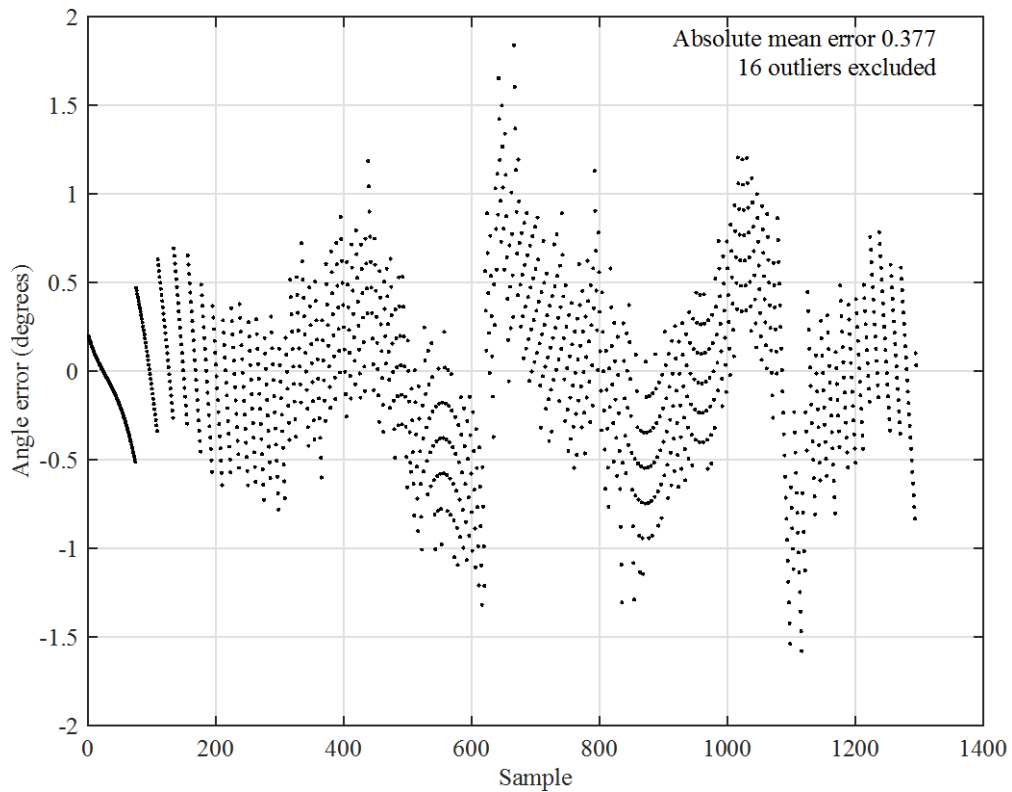
Figure 44.   Curve Fit of One Positive Antenna Sweep (−90° – +90°), Aug. 5, 2015 (network 1)

Note: Test data recorded Aug. 5, 2015, analyzed in network trained with data recorded Aug. 5, 2015 (network 1)

Figure 45.   Residues for One Positive Antenna Sweep (−90° – +90°), Aug. 5, 2015 (network 1)

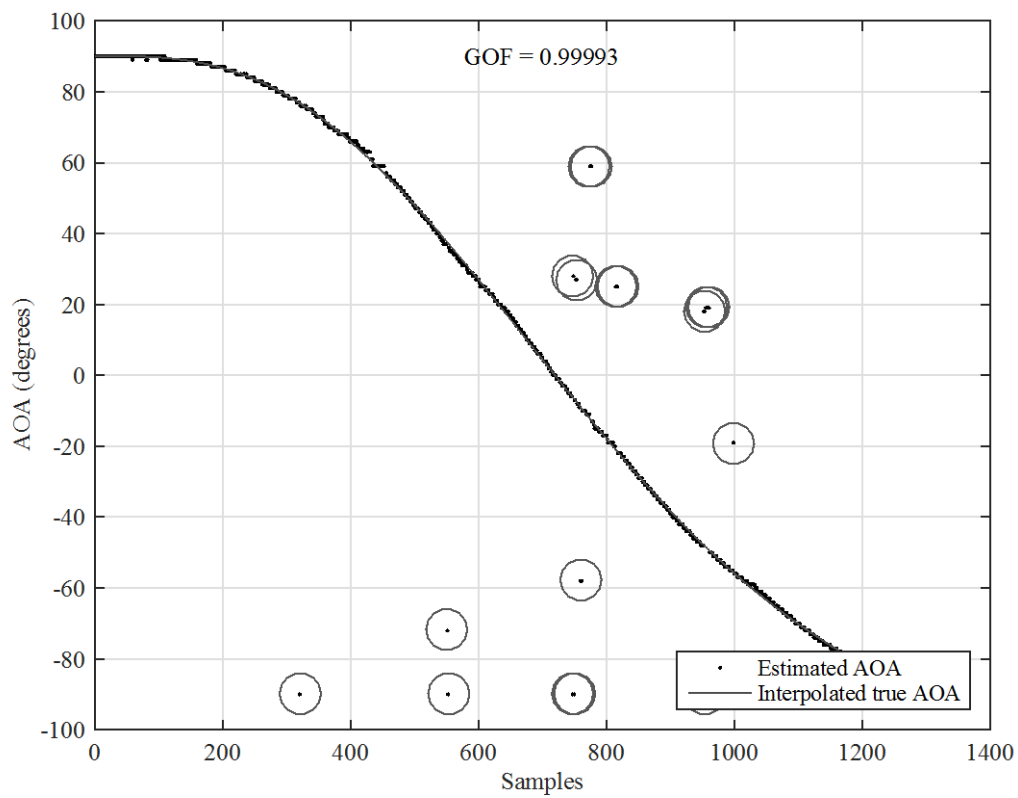Note: Test data recorded Aug. 5, 2015, analyzed in network trained with data recorded Aug. 5, 2015 (network 1). Curve fitted to estimate true DOA.
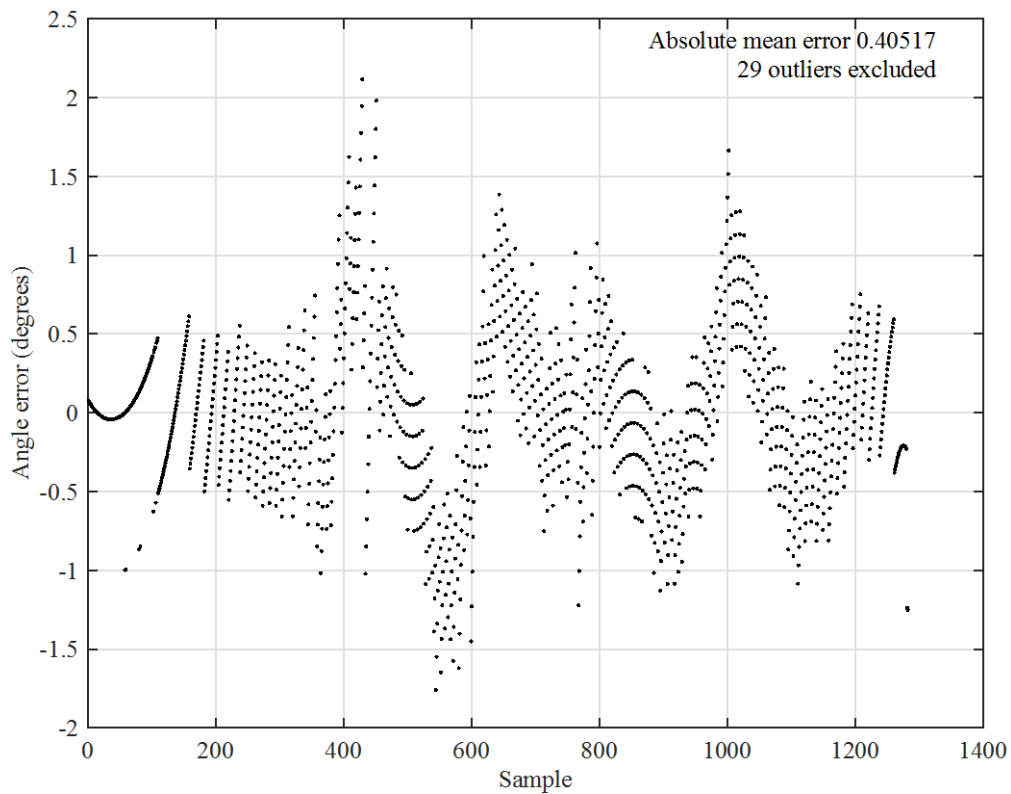
Misclassification was detected in 16 samples out of 1310 total samples, yielding a misclassification rate of 0.0122. The mean angle error after these outliers were removed was computed to 0.377°.

Figure 46.   Curve Fit of One Negative Antenna Sweep (+90° – −90°), Aug. 5, 2015 (network 1)

Note: Test data recorded Aug. 5, 2015, analyzed in network trained with data recorded Aug. 5, 2015 (network 1)

Figure 47.   Residues for One Negative Antenna Sweep (+90° – −90°), Aug. 5, 2015 (network 1)

Note: Test data recorded Aug. 5, 2015, analyzed in network trained with data recorded Aug. 5, 2015 (network 1). Curve fitted to estimate true DOA.

Misclassification was detected in 29 samples out of 1310 total samples, yielding a misclassification rate of 0.0221. The mean angle error after these outliers were removed was computed to 0.40517°.

Figure 48.   Complete Network Output Data for 10 Continuous Antenna
Sweeps in Both Directions, Aug. 5, 2015 (network 2)

Note: Test data recorded Aug. 5, 2015, analyzed in network trained with data recorded
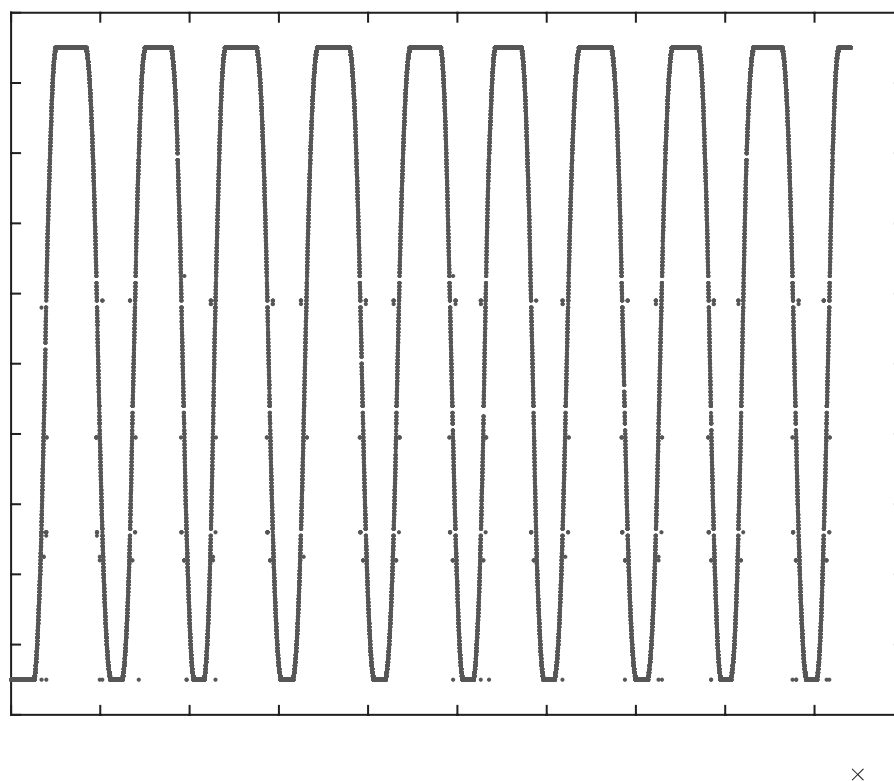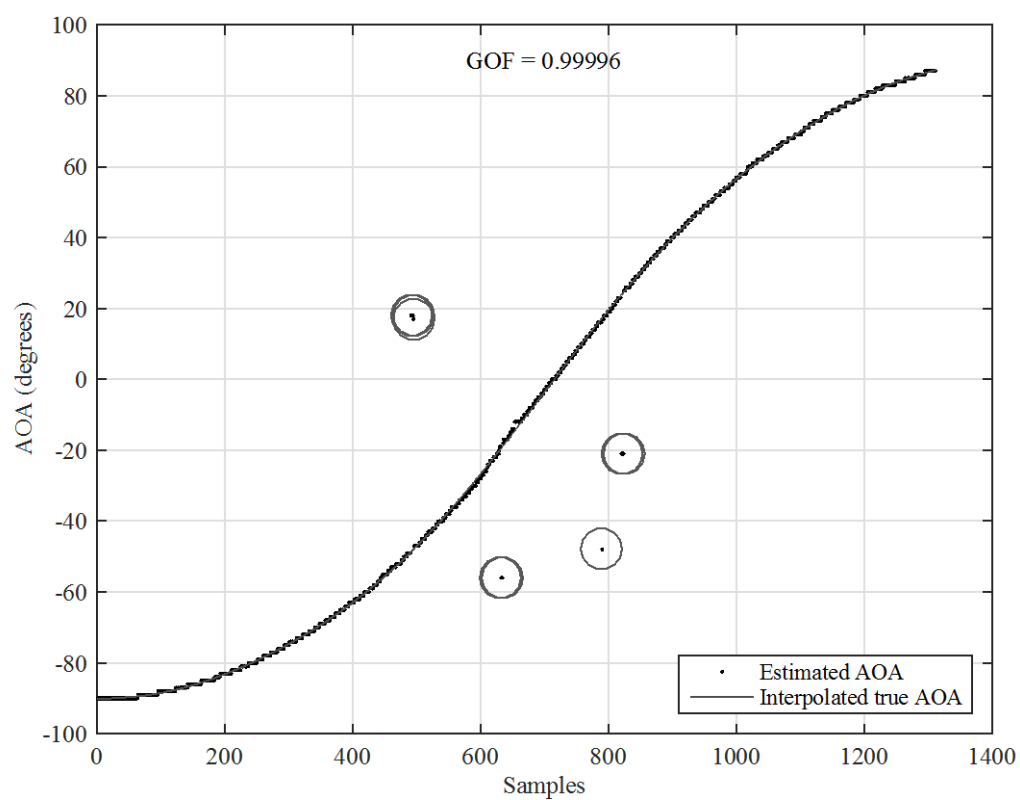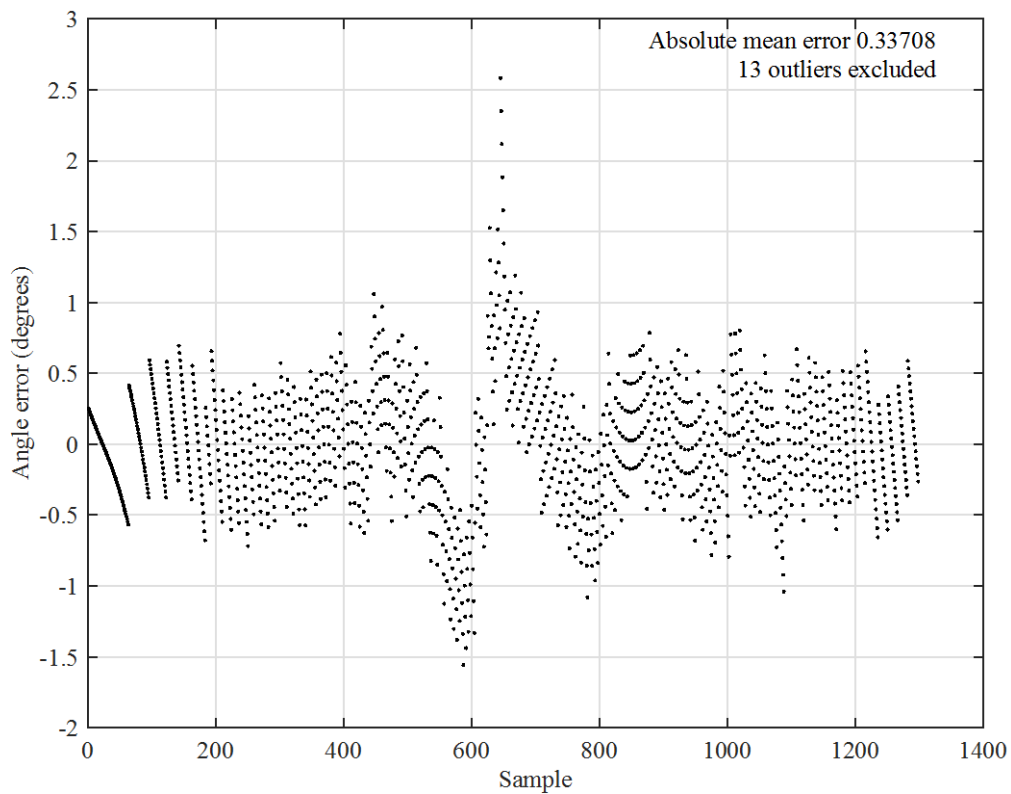Aug. 5, 2015 (network 2)

Figure 49.   Curve Fit of One Positive Antenna Sweep (−90° − +90°), Aug. 5, 2015 (network 2)

Note: Test data recorded Aug. 5, 2015, analyzed in network trained with data recorded Aug. 5, 2015 (network 2)

Figure 50. Residues for One Positive Antenna Sweep (−90° – +90°), Aug. 5, 2015 (network 2)

Note: Test data recorded Aug. 5, 2015, analyzed in network trained with data recorded Aug. 5, 2015 (network 2). Curve fitted to estimate true DOA.

Misclassification was detected in 13 samples out of 1310 total samples, yielding a misclassification rate of 0.0099. The mean angle error after these outliers were removed was computed to 0.33708°.

Figure 51.   Curve Fit of One Negative Antenna Sweep (+90° – −90°), Aug. 5, 2015 (network 2)

Note: Test data recorded Aug. 5, 2015, analyzed in network trained with data recorded Aug. 5, 2015 (network 2)

Figure 52.   Residues for One Negative Antenna Sweep (+90° – −90°), Aug. 5, 2015 (network 2)

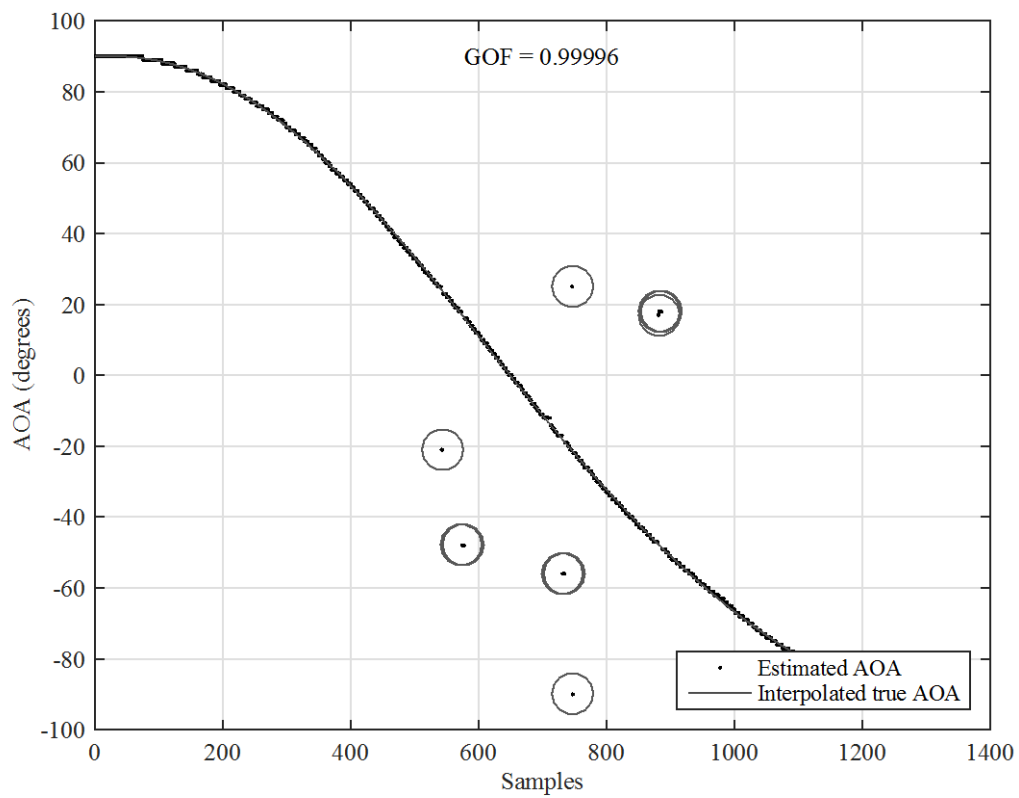Note: Test data recorded Aug. 5, 2015, analyzed in network trained with data recorded Aug. 5, 2015 (network 2). Curve fitted to estimate true DOA.

Misclassification was detected in 18 samples out of 1310 total samples, yielding a misclassification rate of 0.0137. The mean angle error after these outliers were removed was computed to 0.30589°.
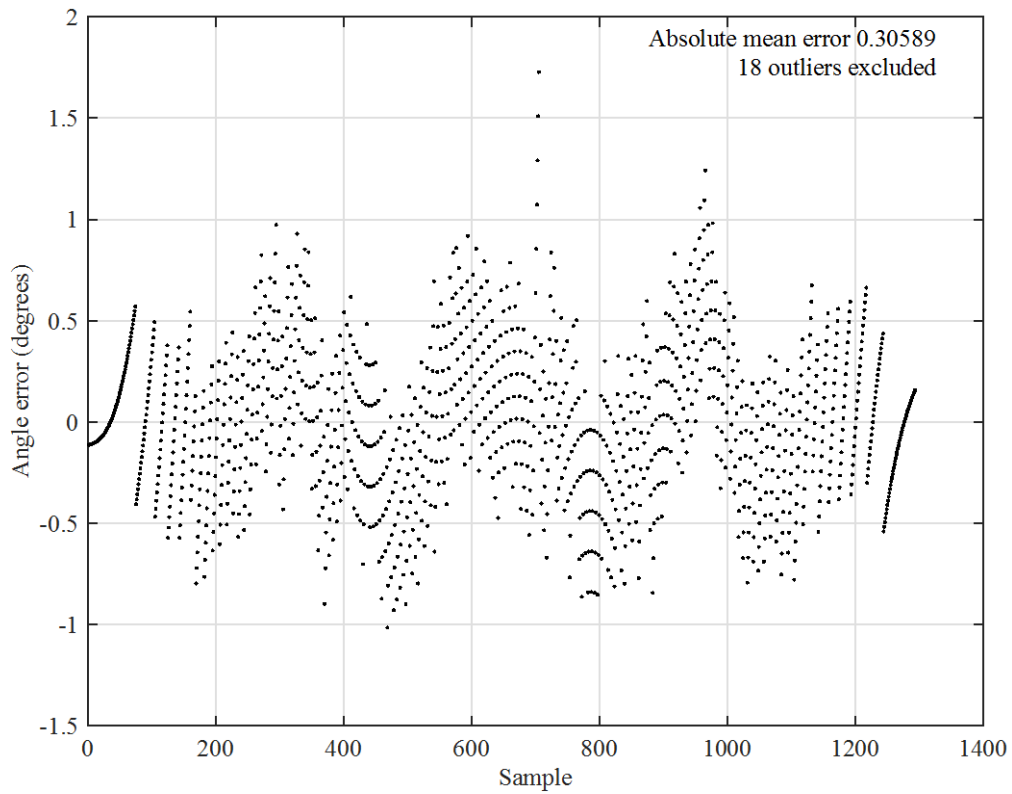
Figure 53.   Complete Network Output Data for 10 Continuous Antenna
Sweeps in Both Directions, Aug. 6, 2015 (network 1)

Note: Test data recorded Aug. 6, 2015, analyzed in network trained with data recorded
Aug. 6, 2015 (network 1)

Figure 54.   Curve Fit of One Positive Antenna Sweep (−90° – +90°), Aug. 6, 2015 (network 1)

Note: Test data recorded Aug. 6, 2015, analyzed in network trained with data recorded Aug. 6, 2015 (network 1)

Figure 55.   Residues for One Positive Antenna Sweep (−90° – +90°), Aug. 6, 2015 (network 1)

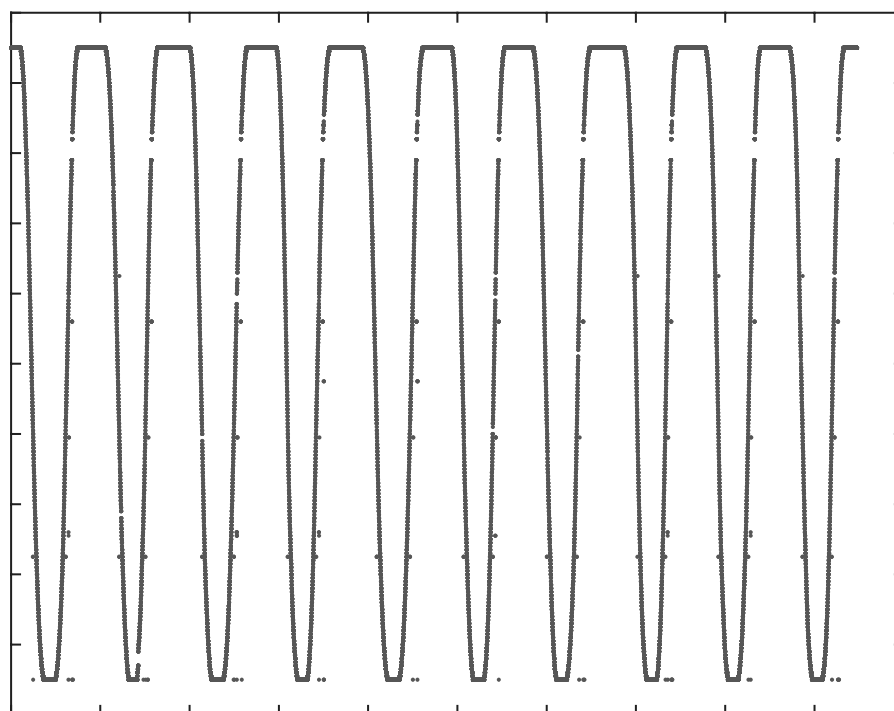Note: Test data recorded Aug. 6, 2015, analyzed in network trained with data recorded Aug. 6, 2015 (network 1). Curve fitted to estimate true DOA.

Misclassification was detected in 17 samples out of 1310 total samples, yielding a misclassification rate of 0.013. The mean angle error after these outliers were removed was computed to 0.32987°.
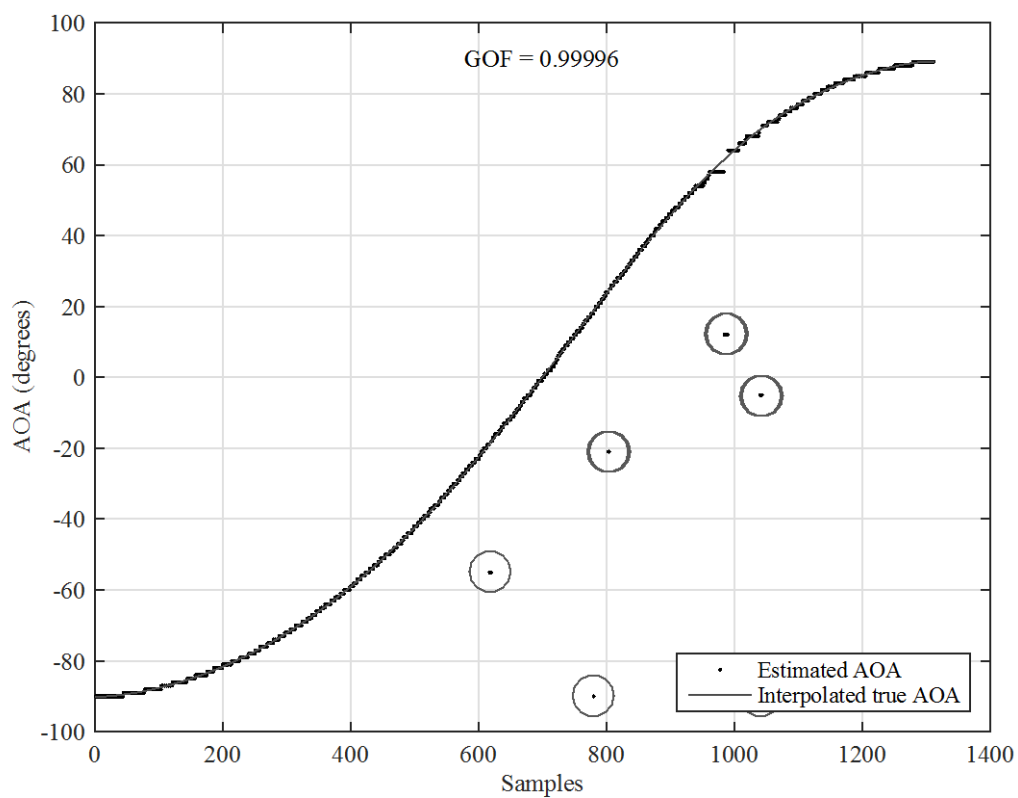
Figure 56.   Curve Fit of One Negative Antenna Sweep (+90° – −90°), Aug. 6, 2015
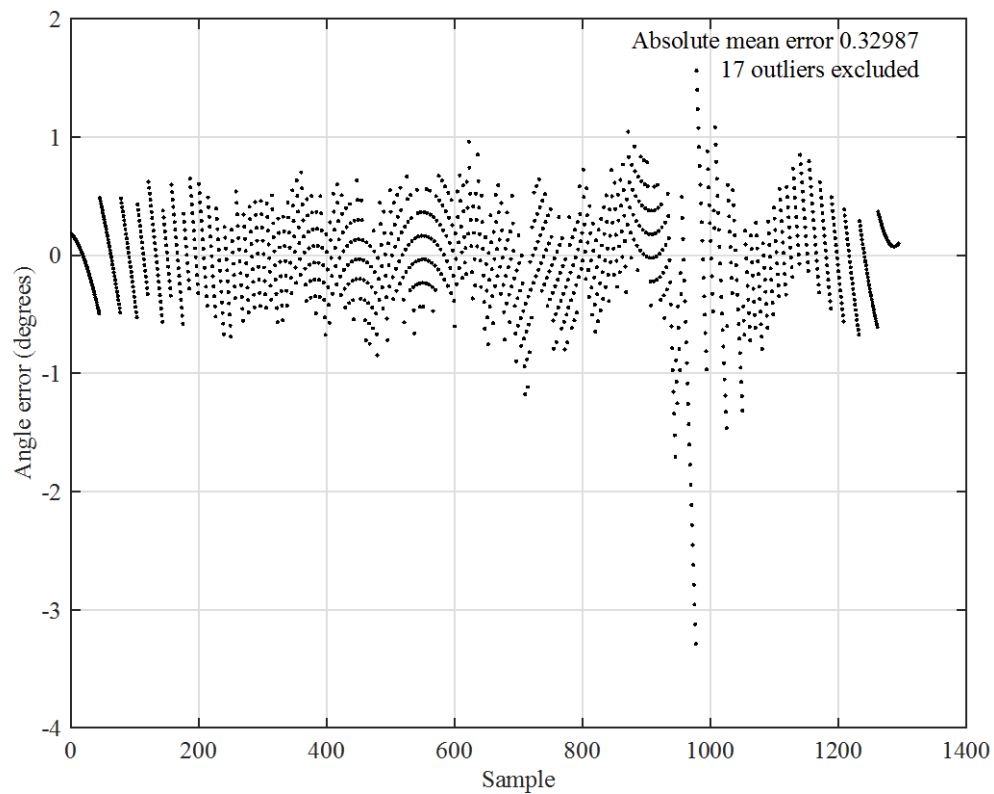

Note: Test data recorded Aug. 6, 2015, analyzed in network trained with data recorded Aug. 6, 2015 (network 1)

Figure 57.   Residues for One Negative Antenna Sweep (+90° – −90°), Aug. 6, 2015

Note: Test data recorded Aug. 6, 2015, analyzed in network trained with data recorded Aug. 6, 2015 (network 1). Curve fitted to estimate true DOA.

Misclassification was detected in three samples out of 1310 total samples, yielding a misclassification rate of 0.0023. The mean angle error after these outliers were removed was computed to 0.36787°.

Figure 58.   Complete Network Output Data for 10 Continuous Antenna
Sweeps in Both Directions, Aug. 6, 2015 (network 2)

Note: Test data recorded Aug. 6, 2015, analyzed in network trained with data recorded
Aug. 6, 2015 (network 2)

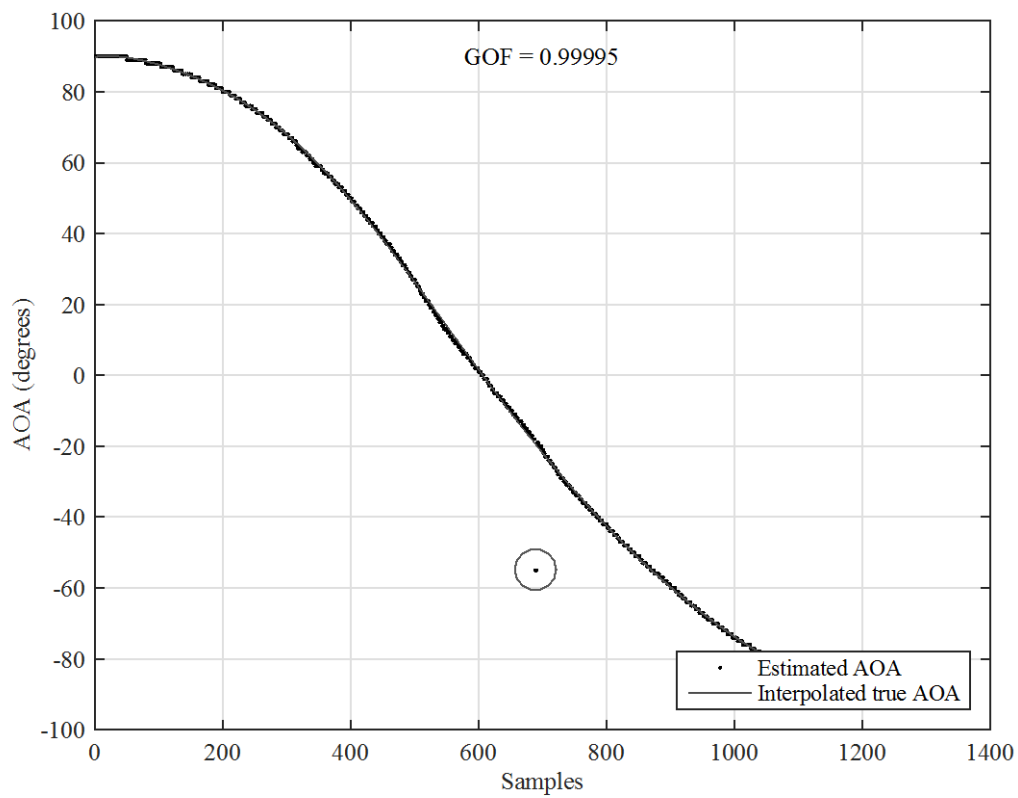Figure 59.   Curve Fit of One Positive Antenna Sweep (−90° – +90°), Aug. 6, 2015 (network 2)
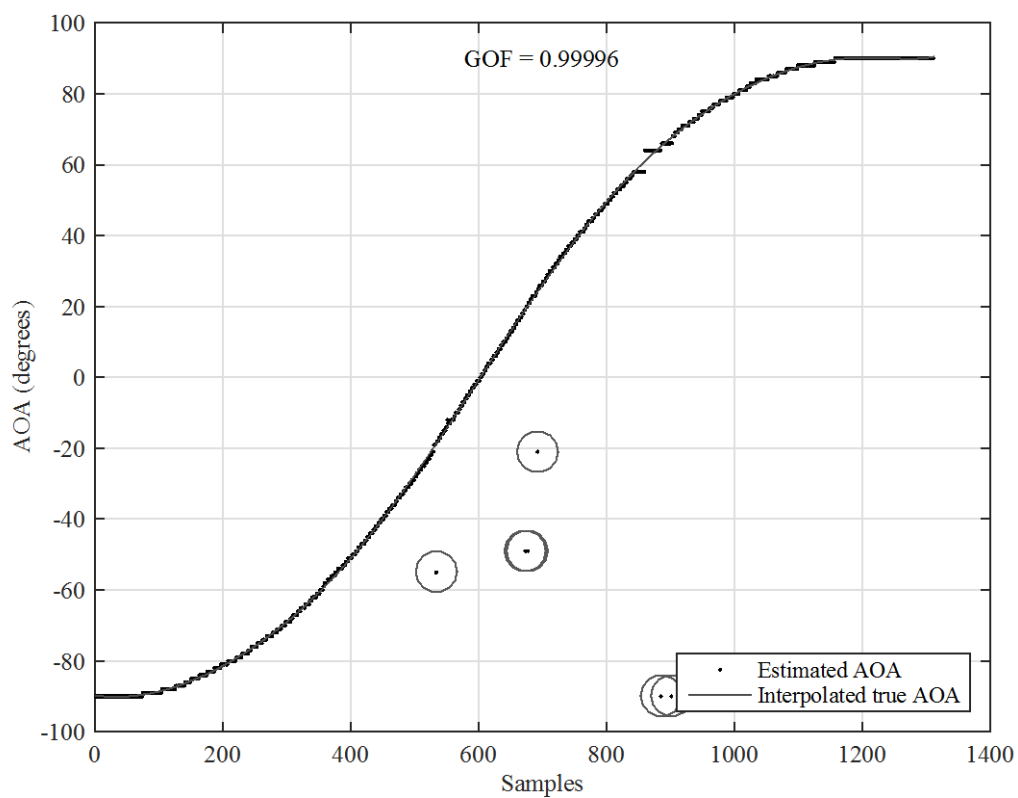
Note: Test data recorded Aug. 6, 2015, analyzed in network trained with data recorded Aug. 6, 2015 (network 2)

Figure 60.   Residues for One Positive Antenna Sweep (−90° – +90°), Aug. 6, 2015 (network 2)
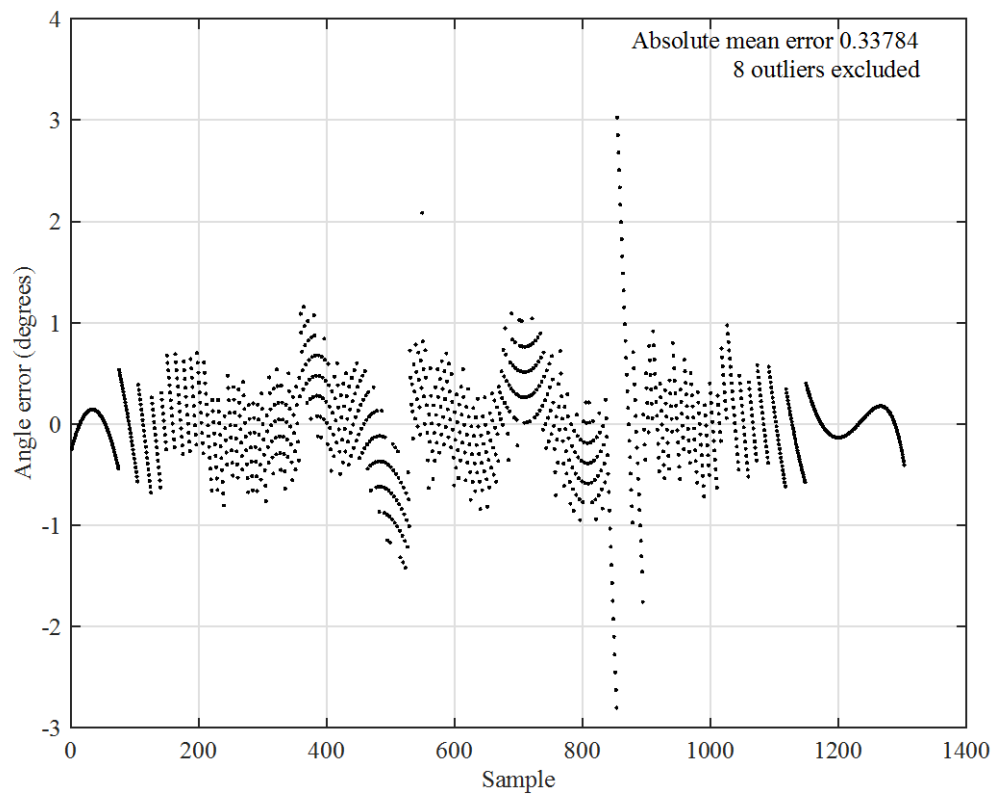
Note: Test data recorded Aug. 6, 2015, analyzed in network trained with data recorded Aug. 6, 2015 (network 2). Curve fitted to estimate true DOA.
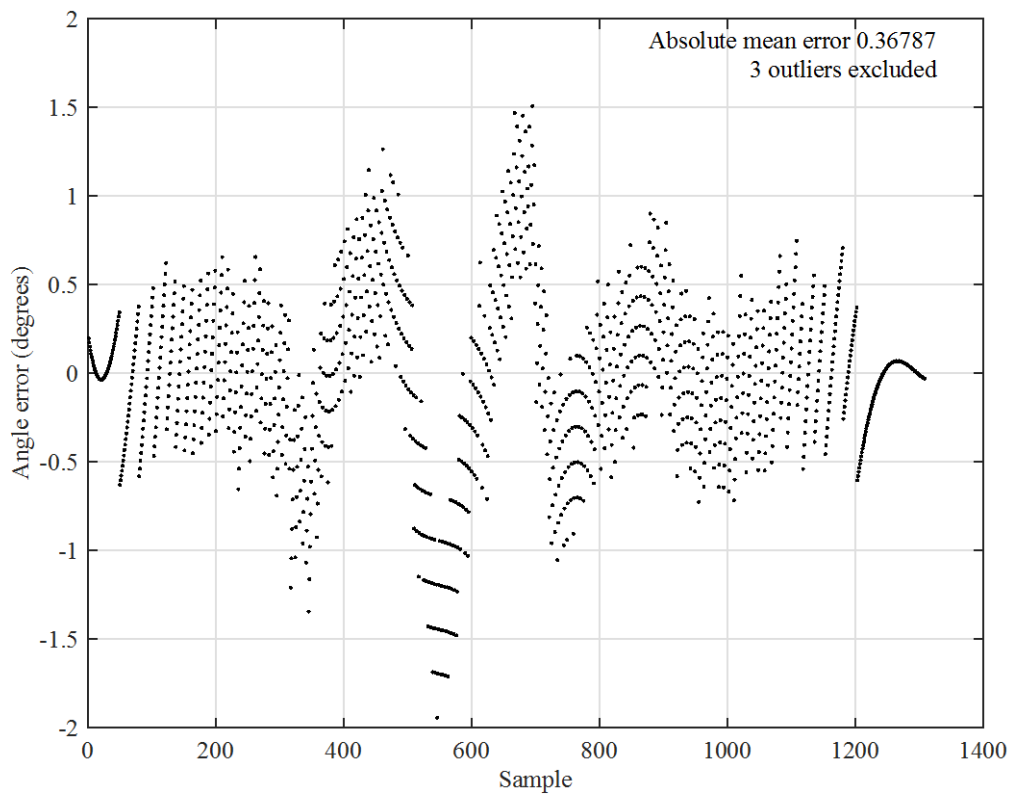
Misclassification was detected in eight samples out of 1310 total samples, yielding a misclassification rate of 0.0061. The mean angle error after these outliers were removed was computed to 0.33784°.

Figure 61.   Curve Fit of One Negative Antenna Sweep (+90° – −90°), Aug. 6, 2015 (network 2)

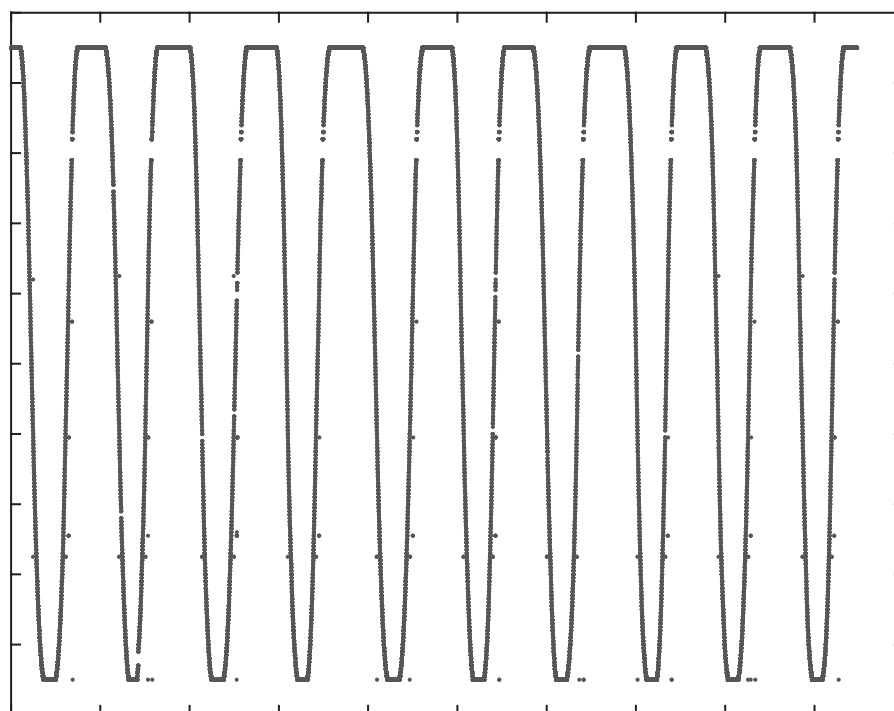Note: Test data recorded Aug. 6, 2015, analyzed in network trained with data recorded Aug. 6, 2015 (network 2)

Figure 62.   Residues for One Negative Antenna Sweep (+90° – −90°), Aug. 6, 2015 (network 2)
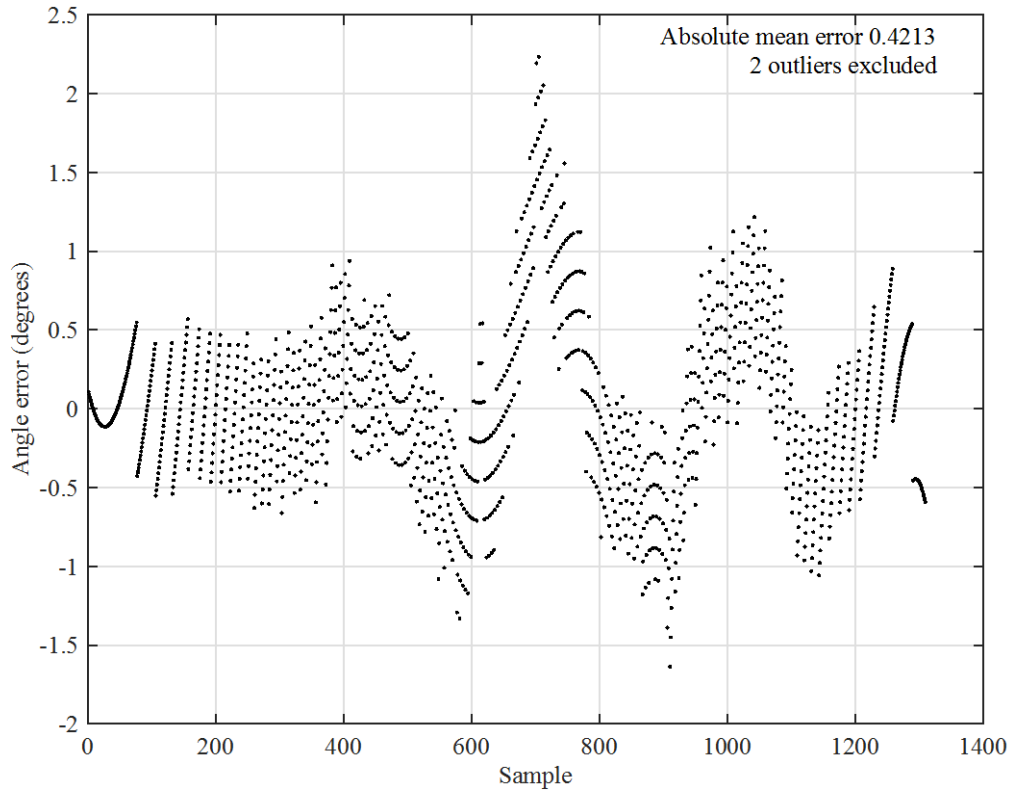
Note: Test data recorded Aug. 6, 2015, analyzed in network trained with data recorded Aug. 6, 2015 (network 2). Curve fitted to estimate true DOA.

Misclassification was detected in two samples out of 1310 total samples, yielding a misclassification rate of 0.0015. The mean angle error after these outliers were removed was computed to 0.4213°.
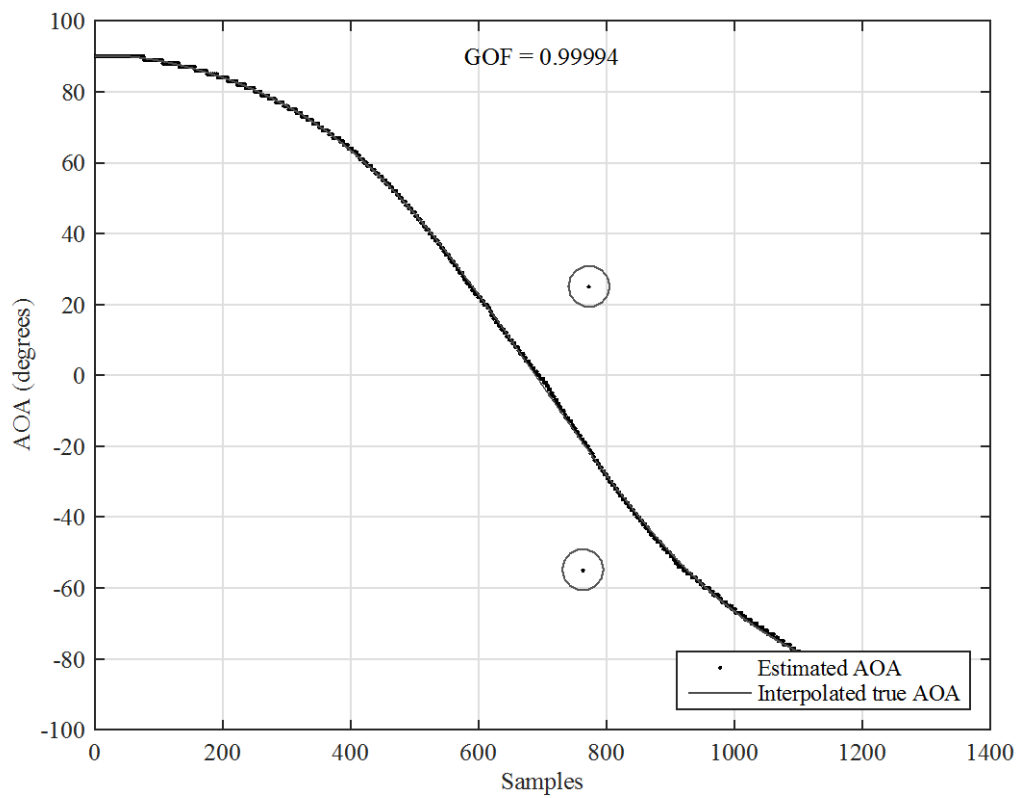
C.   TRAINING DATA AND TEST DATA FROM DIFFERENT DAYS

This section contains results from test data and networks trained on data recorded one and two days in between each other. Results in Figures 63–67 show how the system performed when training was approximately 24 hours old, while Figures 68–72 show performance for training 48 hours old. The complete output consists of results for 20 continuous antenna sweeps, 10 in either direction. For each test set, one antenna sweep in

either direction was further analyzed. Sweeps analyzed in detail were those considered worst cases; this was done in order to determine maximum angle error for the system.

Each test result consists of five plots, the first showing the full resulting dataset, the second and third showing performance for a positive antenna sweep, and the fourth and fifth showing performance for a negative antenna sweep. Residues with errors greater than 90° were considered as outliers and removed from mean error calculations. The number of removed outliers and absolute mean error are shown in each residue plot, and these outliers are shown as circles in the curve fit plots. A total number of 1310 samples were used for each detailed analysis.

When the previous results for same-day testing were computed, outliers were considered to differ 10° or more from the interpolated DOA. Due to the different limits used for the removal of outliers, the results are not fully comparable between the two tests. Results show how performance degrades as the training gets older.

Figure 63. Complete Network Output Data for 10 Continuous Antenna
Sweeps in Both Directions, One Day between Training and Testing
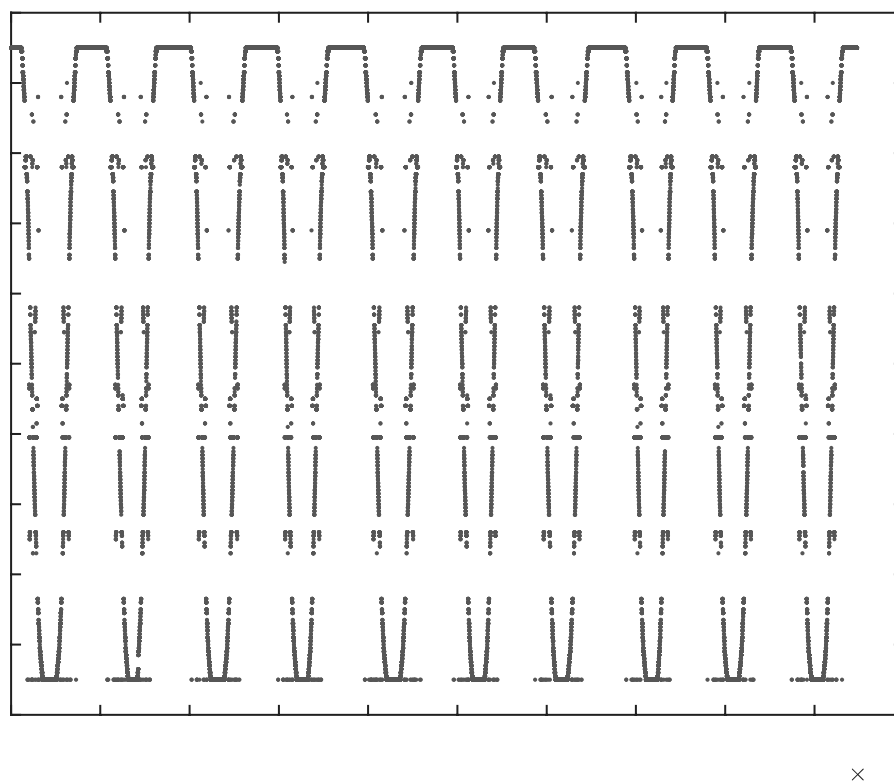
Note: Test data recorded Aug. 6, 2015, analyzed in network trained with data recorded
Aug. 5, 2015

Figure 64.   Curve Fit of One Positive Antenna Sweep (−90° – +90°), One Day
between Training and Testing
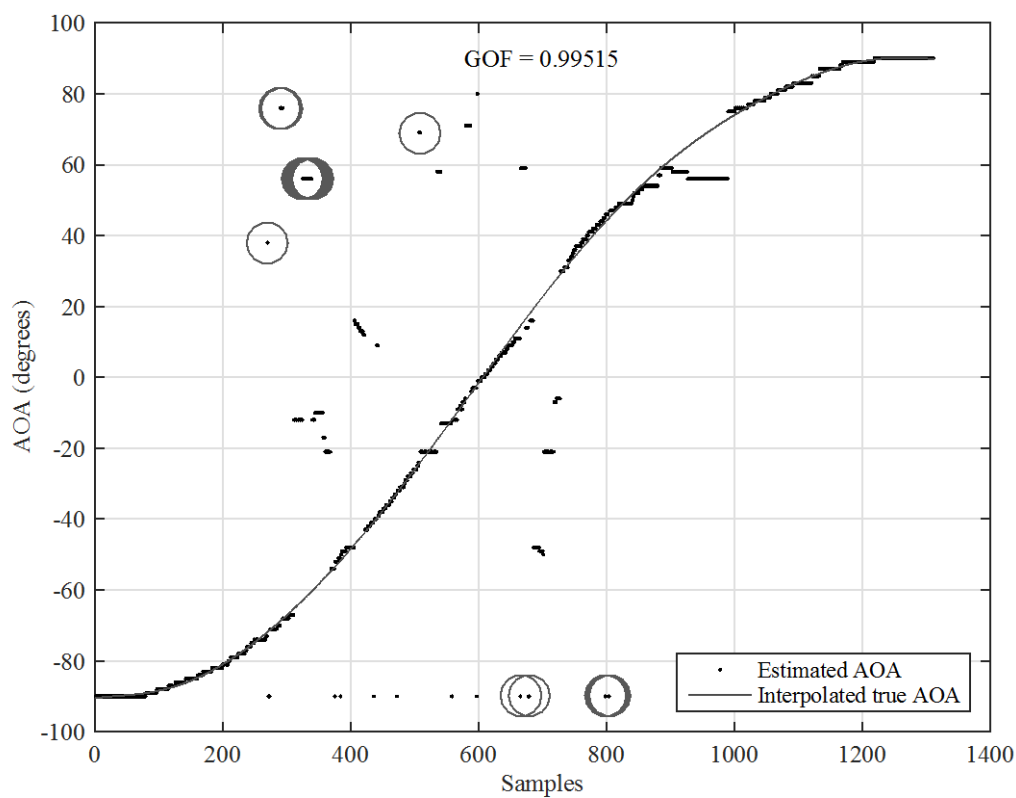
Note: Test data recorded Aug. 6, 2015, analyzed in network trained with data recorded
Aug. 5, 2015

Figure 65.   Residues for One Positive Antenna Sweep (−90° – +90°), One Day
between Training and Testing

Note: Test data recorded Aug. 6, 2015, analyzed in network trained with data recorded
Aug. 5, 2015. Curve fitted to estimate true DOA.

Misclassification was detected in 28 samples out of 1310 total samples, yielding a misclassification rate of 0.0214. The mean angle error after these outliers were removed was computed to 6.8761°.

Figure 66.   Curve Fit of One Negative Antenna Sweep (+90° − −90°), One
Day between Training and Testing

Note: Test data recorded Aug. 6, 2015, analyzed in network trained with data recorded
Aug. 5, 2015

Figure 67.   Residues for One Negative Antenna Sweep (+90° − −90°), One
Day between Training and Testing
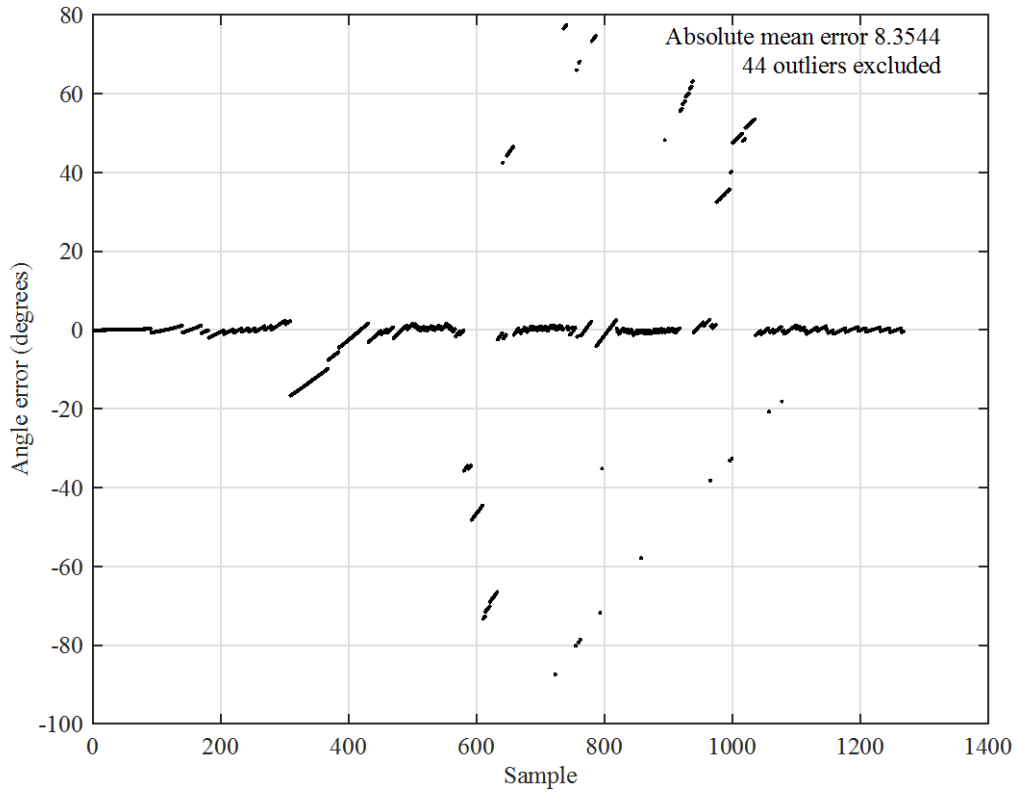
Note: Test data recorded Aug. 6, 2015, analyzed in network trained with data recorded
Aug. 5, 2015. Curve fitted to estimate true DOA.

Misclassification was detected in 44 samples out of 1310 total samples, yielding a
misclassification rate of 0.0336. The mean angle error after these outliers were removed
was computed to 8.3544°.

Figure 68.   Complete Network Output Data for 10 Continuous Antenna
Sweeps in Both Directions, Two Days between Training and Testing
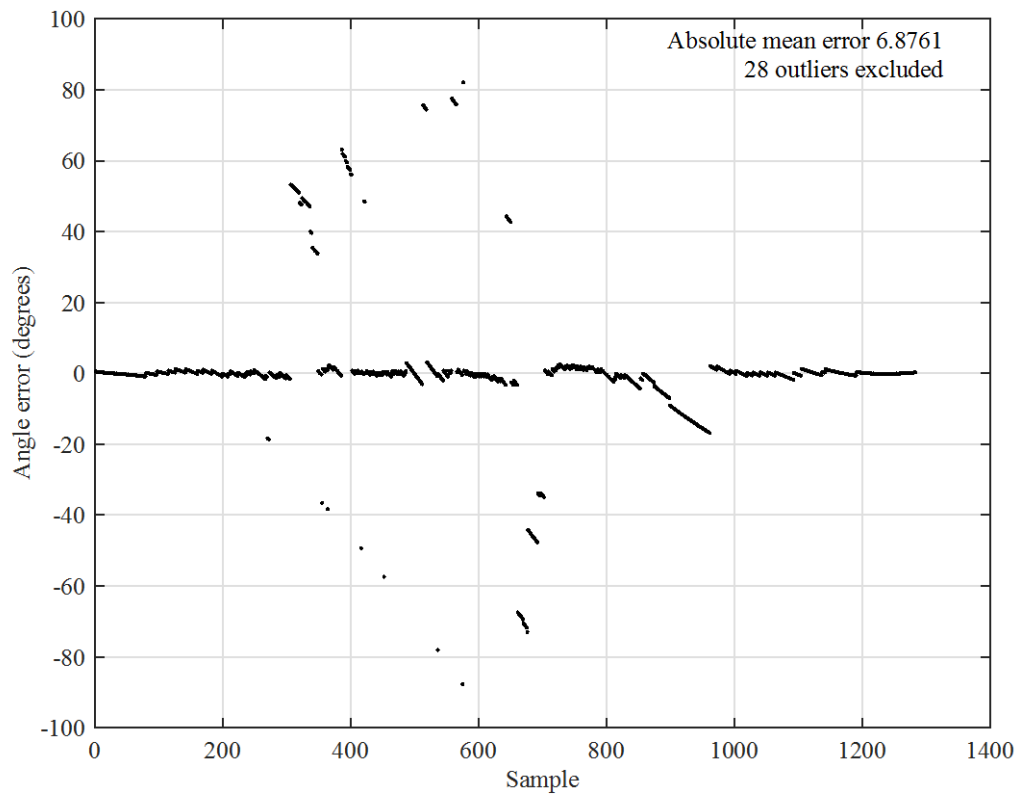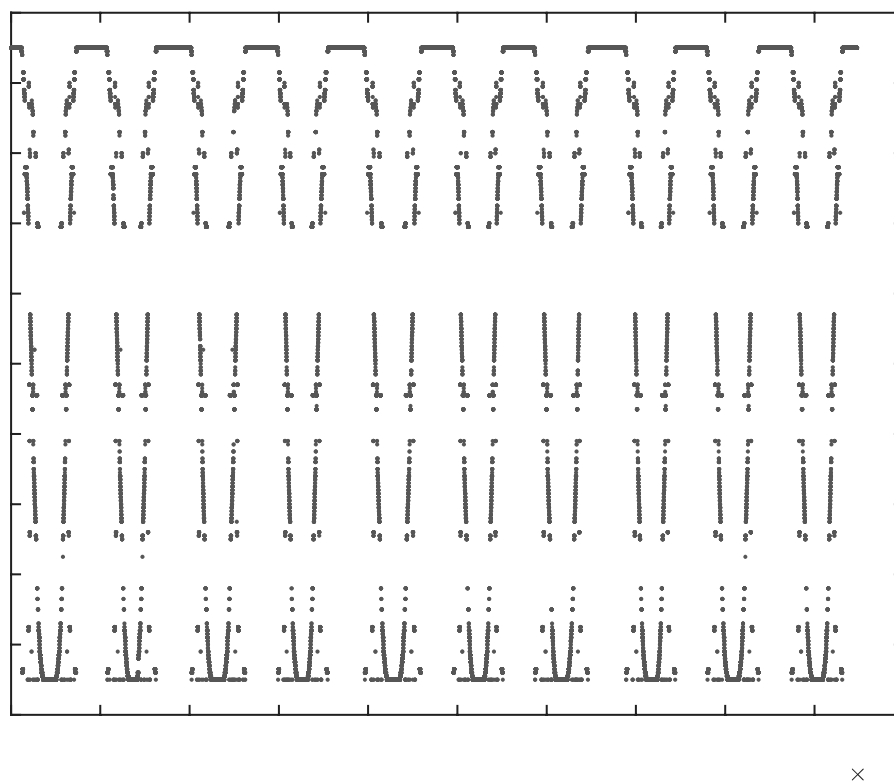

Note: Test data recorded Aug. 6, 2015, analyzed in network trained with data recorded
Aug. 4, 2015

Figure 69. Curve Fit of One Positive Antenna Sweep (−90° – +90°), Two
Days between Training and Testing
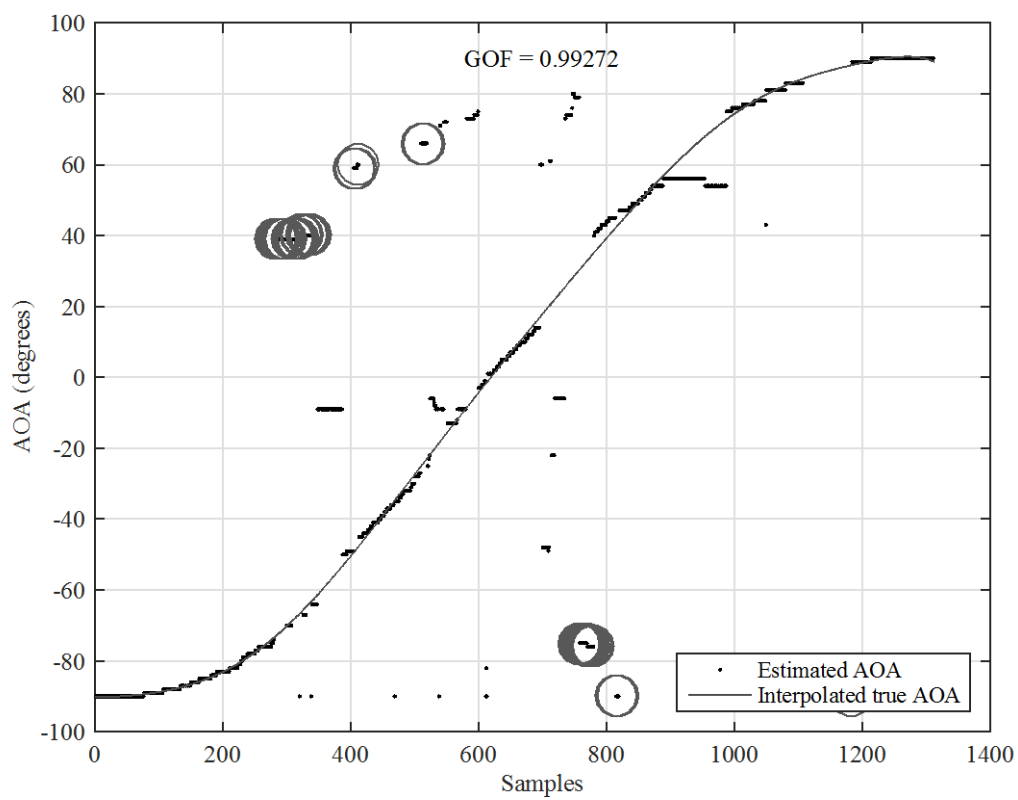
Note: Test data recorded Aug. 6, 2015, analyzed in network trained with data recorded
Aug. 4, 2015

Figure 70.   Residues for One Positive Antenna Sweep (−90° – +90°), Two
Days between Training and Testing
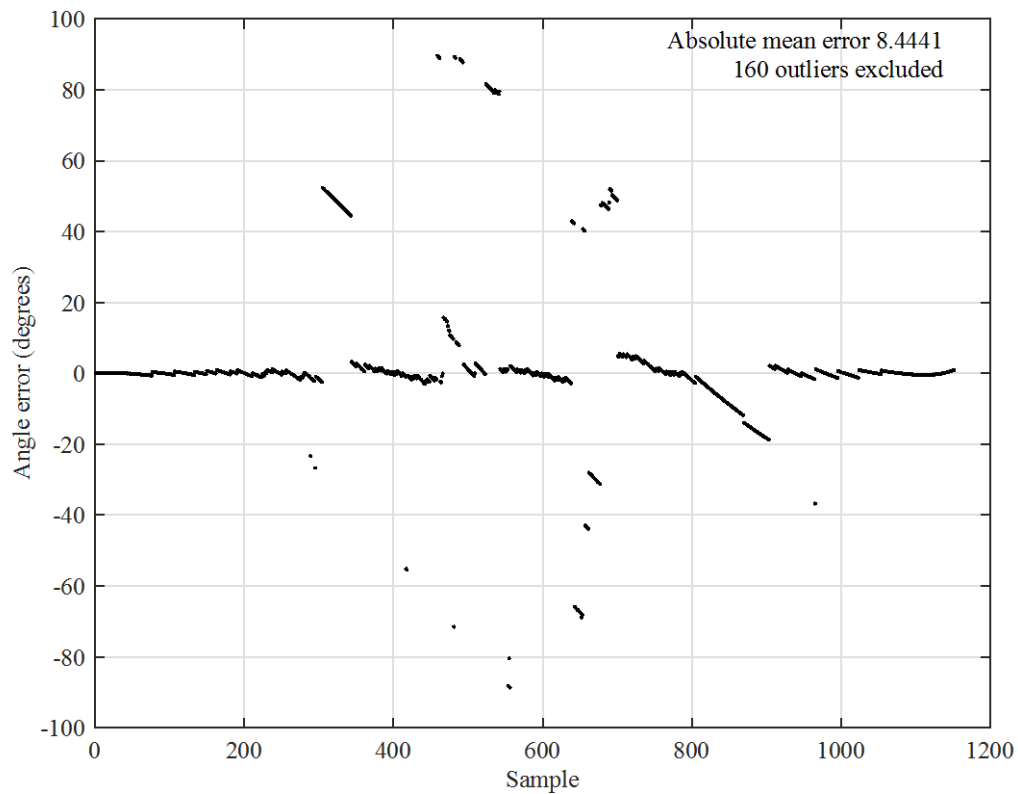
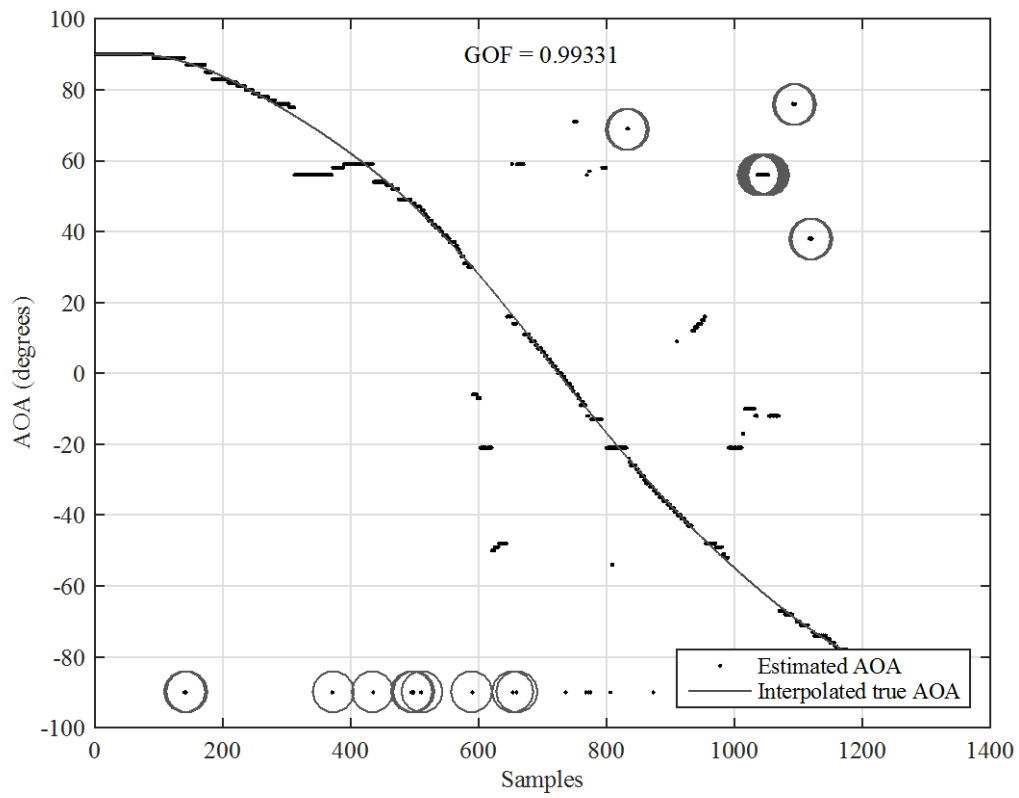Note: Test data recorded Aug. 6, 2015, analyzed in network trained with data recorded
Aug. 4, 2015. Curve fitted to estimate true DOA.

Misclassification was detected in 160 samples out of 1310 total samples, yielding a misclassification rate of 0.1221. The mean angle error after these outliers were removed was computed to 8.4441°.

Figure 71.   Curve Fit of One Negative Antenna Sweep (+90° – −90°), Two
Days between Training and Testing
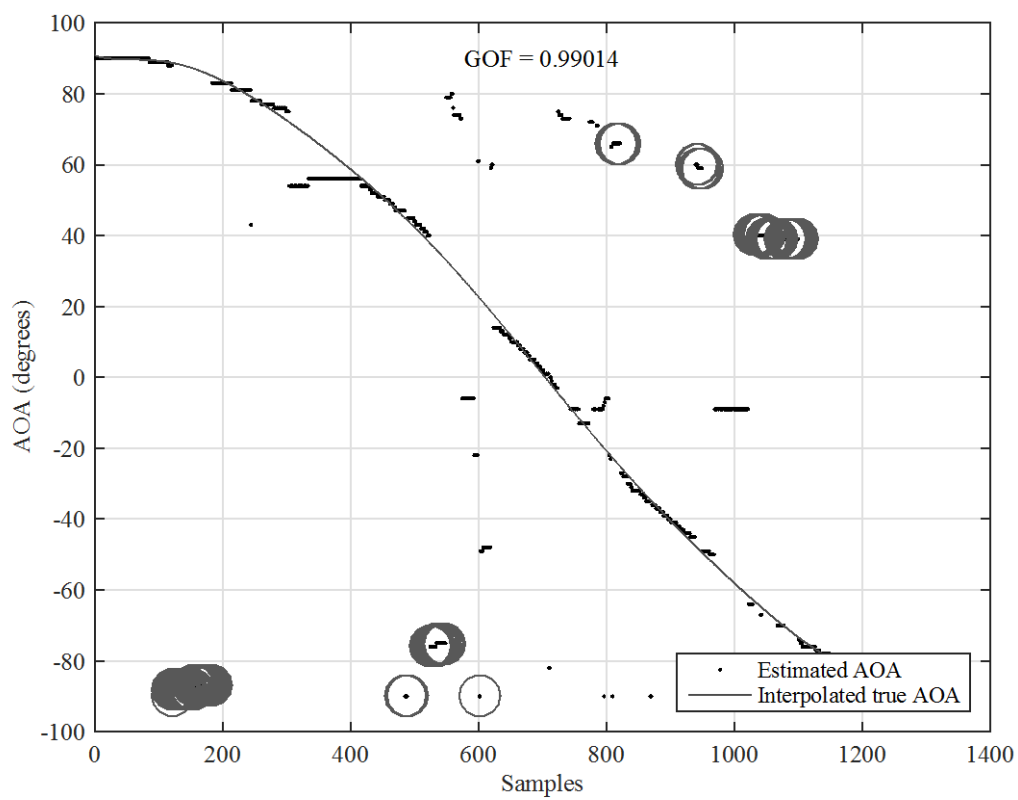
Note: Test data recorded Aug. 6, 2015, analyzed in network trained with data recorded
Aug. 4, 2015

Figure 72. Residues for One Negative Antenna Sweep (+90° − −90°), Two
Days between Training and Testing
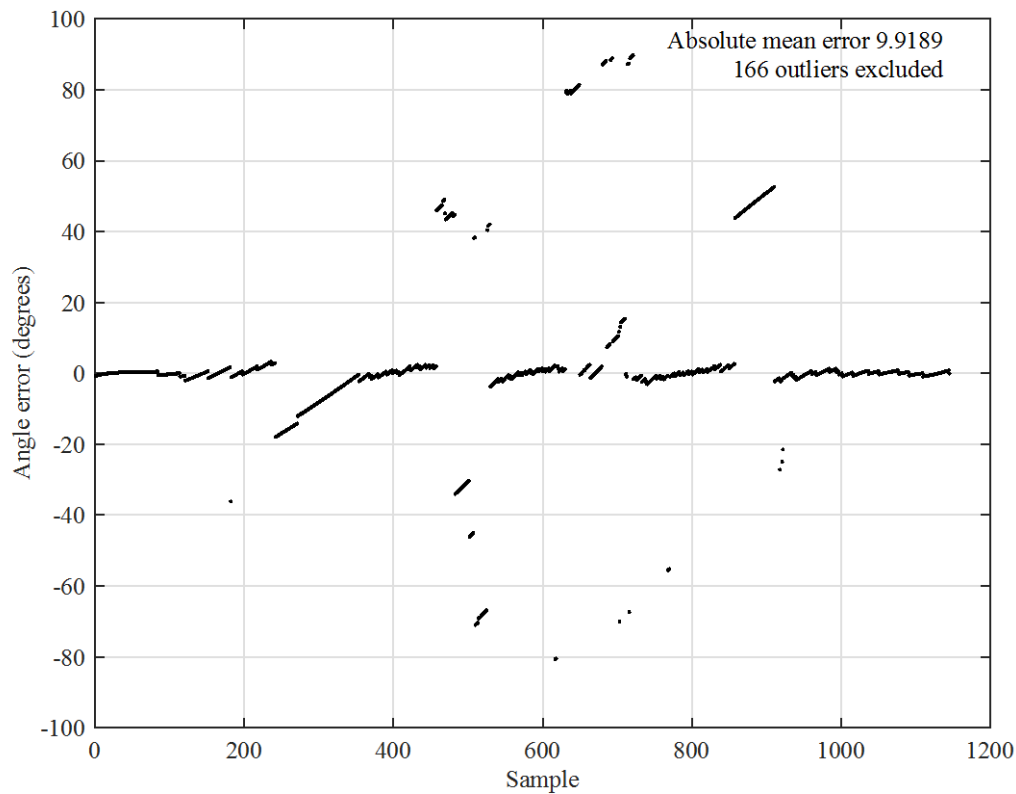
Note: Test data recorded Aug. 6, 2015, analyzed in network trained with data recorded
Aug. 4, 2015. Curve fitted to estimate true DOA.

Misclassification was detected in 166 samples out of 1310 total samples, yielding
a misclassification rate of 0.1267. The mean angle error after these outliers were removed
was computed to 9.9189°.

Results plotted in Figure 63 to Figure 72 clearly show how performance degrades
as the training gets older in relation to the test set. Performance results are shown for
comparison in Table 6.

Table 6.   Performance Comparison between 24- and 48-Hour-Old Training

Dataset	Misclassification rate	Mean error
1 day old network	0.0214	6.8761°
-:-	0.0336	8.3544°
2 days old network	0.1221	8.4441°
-:-	0.1267	9.9189°

Note: Test data from Aug. 6, 2015 was tested on networks trained on data from Aug. 4, 2015, and Aug. 5, 2015.

Retraining appeared to be necessary less than 24 hours apart to preserve performance of the system. The most probable cause for the time varying errors was considered to be related to bias voltage drift in the MZM and could be minimized by adding a bias control circuit to the modulators.

D.   UNALIGNED DATA FROM AUG. 12, 2015

In order to evaluate whether channel alignment played a role in performance, training and test data were recorded without aligning the channels.

This section contains results from test data and networks trained on data recorded within a few hours of each other. Results show how the system performed when fairly recently bias calibrated and trained, as depicted in Figures 73–77. The complete output consists of results for 20 continuous antenna sweeps, 10 in either direction. For each test set, one antenna sweep in either direction was further analyzed. Sweeps analyzed in detail were those considered worst cases; this was done in order to determine the maximum angle error for the system.

Each test result consists of five plots, the first showing the full resulting dataset, the second and third showing performance for a positive antenna sweep, and the fourth

113

and fifth showing performance for a negative antenna sweep. As described earlier, true DOA was not available but interpolated. Residues with errors greater than 10° were considered as outliers and removed from mean error calculations. The number of removed outliers and absolute mean error are shown in each residue plot, and these outliers are shown as circles in the curve fit plots. A total number of 1310 samples were used for each detailed analysis.

Figure 73.　Complete Network Output Data for 10 Continuous Antenna Sweeps in Both Directions, Aug. 12, 2015 (not RSNS-aligned)
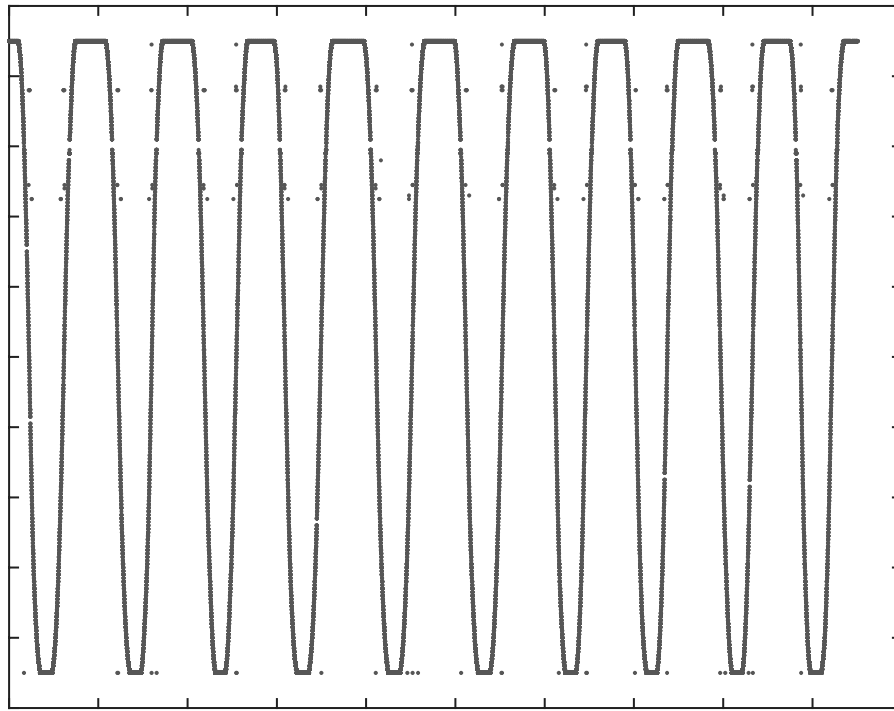
Note: Test data recorded Aug. 12, 2015, analyzed in network trained with data recorded Aug. 12, 2015 (not RSNS-aligned)

114

Figure 74.   Curve Fit of One Positive Antenna Sweep (−90° – +90°), Aug. 12, 2015 (not RSNS-aligned)
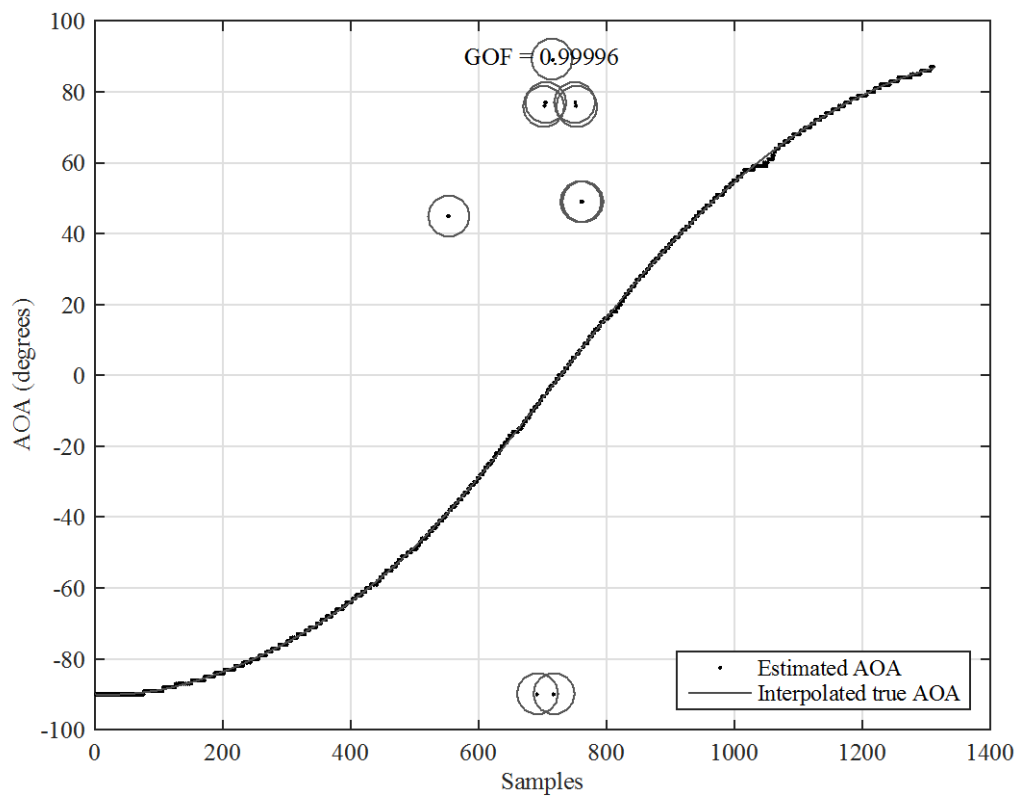
Note: Test data recorded Aug. 12, 2015, analyzed in network trained with data recorded Aug. 12, 2015 (not RSNS-aligned)

Figure 75.   Residues for One Positive Antenna Sweep (−90° – +90°), Aug. 12, 2015 (not RSNS-aligned)
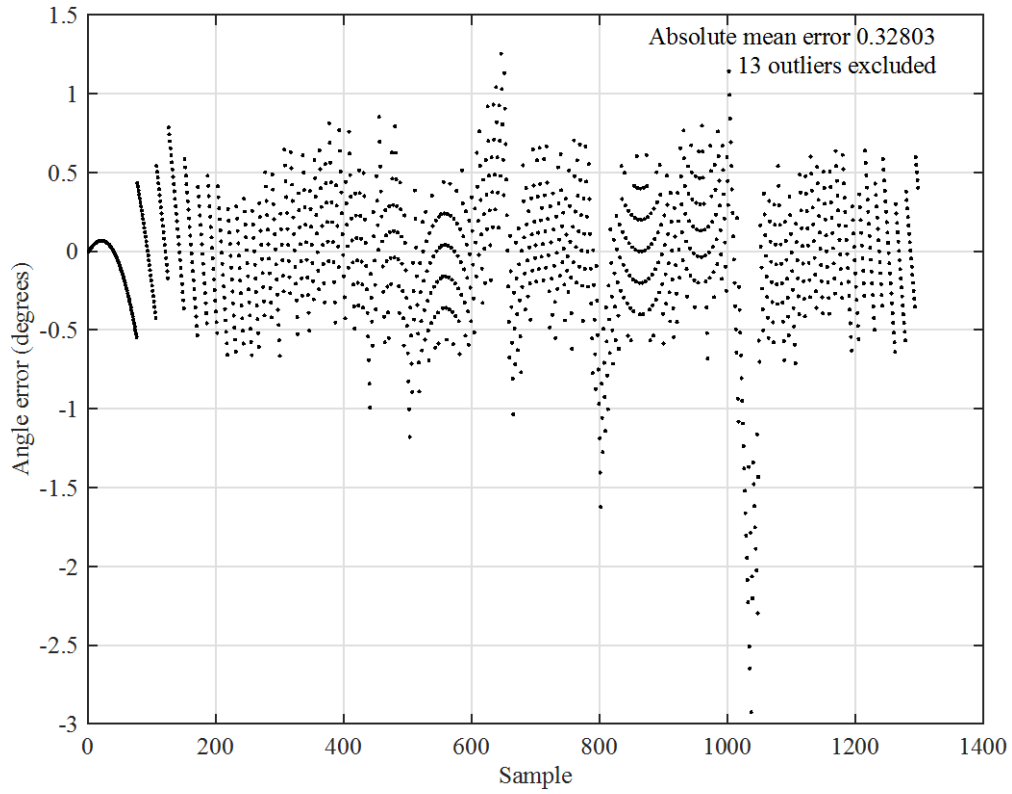
Note: Test data recorded Aug. 12, 2015, analyzed in network trained with data recorded Aug. 12, 2015 (not RSNS-aligned). Curve fitted to estimate true DOA.

Misclassification was detected in 13 samples out of 1310 total samples, yielding a misclassification rate of 0.0099. The mean angle error after these outliers were removed was computed to 0.32803°.

Figure 76.   Curve Fit of One Negative Antenna Sweep (+90° – −90°), Aug.
12, 2015 (not RSNS-aligned)
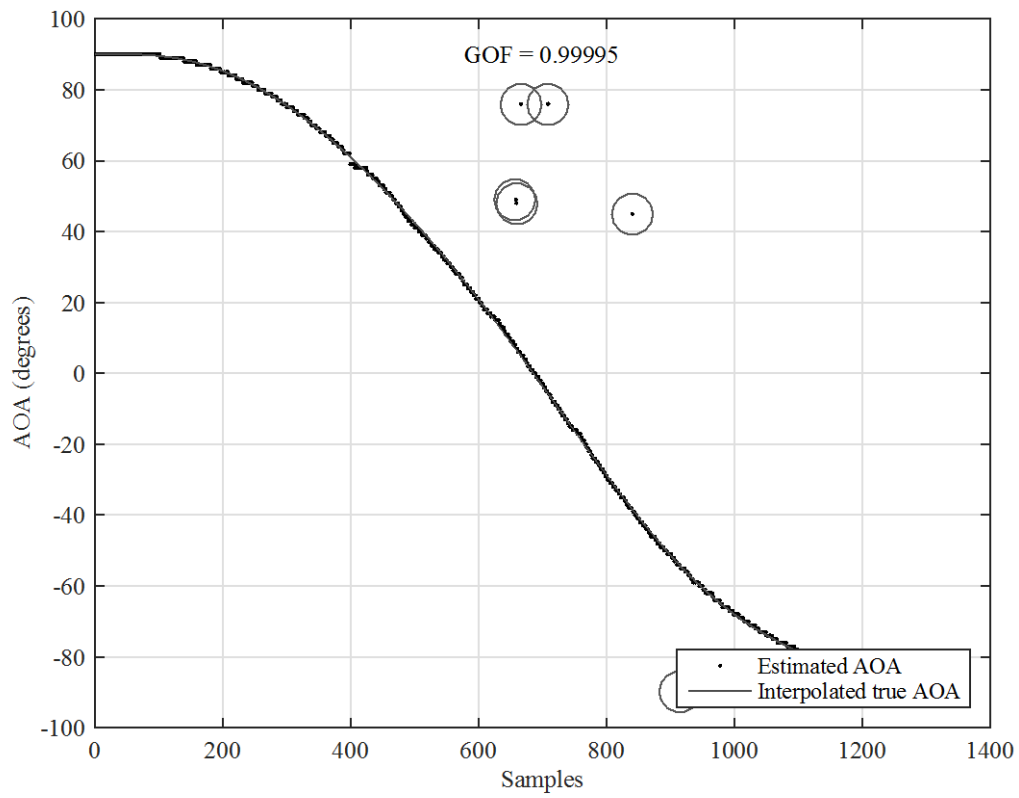
Note: Test data recorded Aug. 12, 2015, analyzed in network trained with data recorded
Aug. 12, 2015 (not RSNS-aligned)

Figure 77.   Residues for One Negative Antenna Sweep (+90° − −90°), Aug. 12, 2015 (not RSNS-aligned)
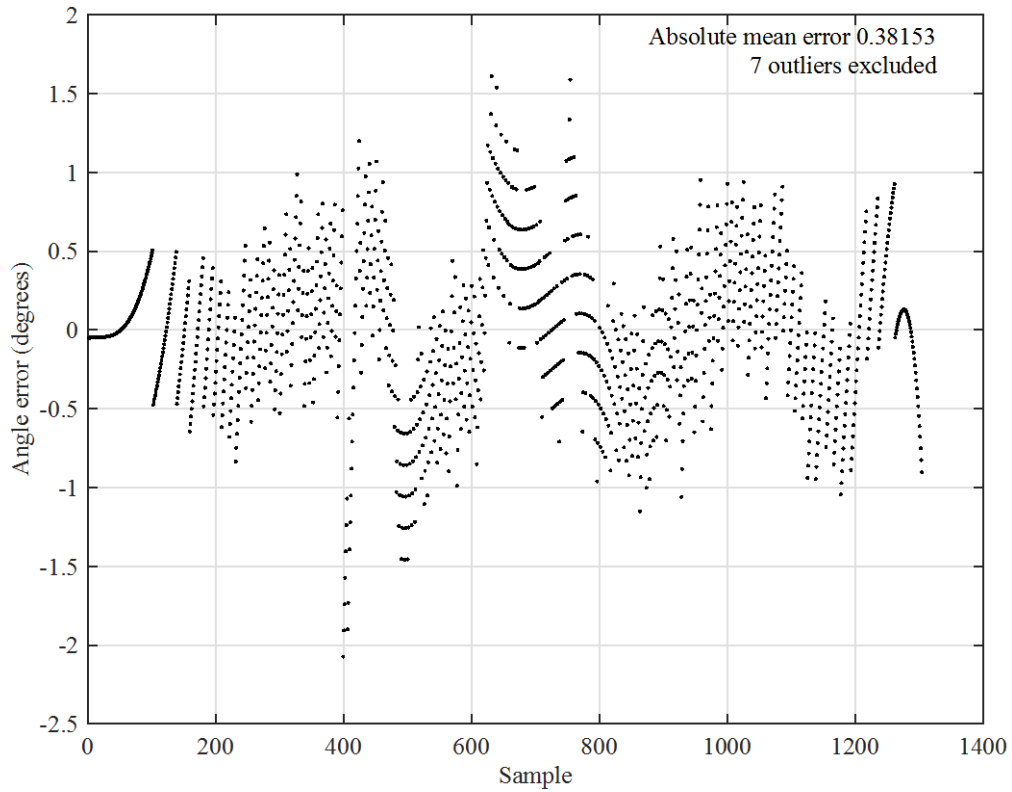
Note: Test data recorded Aug. 12, 2015, analyzed in network trained with data recorded Aug. 12, 2015 (not RSNS-aligned). Curve fitted to estimate true DOA.

Misclassification was detected in seven samples out of 1310 total samples, yielding a misclassification rate of 0.0053. The mean angle error after these outliers were removed was computed to 0.38153°.

E.   COMPARISON OF ALIGNED AND UNALIGNED SYSTEM

A comparison of system performance between the aligned and unaligned system is shown in Table 7.

Table 7.   Performance Comparison between Aligned and Unaligned System

Dataset	Misclassification rate	Mean error
04AUG	0.00076	0.33694°
-:-	0.00760	0.40932°
05AUG network1	0.01220	0.37700°
-:-	0.02210	0.40517°
05AUG network2	0.00990	0.33708°
-:-	0.01370	0.30589°
06AUG network1	0.01300	0.32987°
-:-	0.00230	0.36787°
06AUG network2	0.00610	0.33784°
-:-	0.00150	0.42130°
12AUG	0.00990	0.32803°
-:-	0.00530	0.38153°
Averaged values		
Aligned system	0.00892	0.36283°

Unaligned system	0.00760	0.35478°

Note: Test data from Aug. 4, 2015, to Aug. 6, 2015, were recorded in a system aligned according to [23] and [22], while test data from Aug. 12, 2015, were recorded in an unaligned system.

According to test data, phase alignment of the channels does not appear to play a significant part in system performance.

In this chapter, the results from three different test cases were described. Initially it was shown that a system with channels phase aligned according to [23] and [22] was capable of determining DOA with a mean error better than 0.5°. Thereafter, it was demonstrated that system performance decreased as time between training and testing increased. Lastly, it was shown that the system was able to perform DOA measurement with a mean error better than 0.5° even when the channels were not phase aligned. In the following chapter, the implications of these results are discussed and recommendations for future work are provided.

IX.   CONCLUDING REMARKS AND FUTURE CONSIDERATIONS

Data from experimental tests showed that the system is capable of determining DOA by sampling the envelope values of the optical output amplitude. The design has a mean error less than 0.5°, which is consistent with best possible theoretical performance. Since the resolution is determined by discrete representations of DOA, best theoretical mean error magnitude is half the resolution. In this investigation, a resolution of 1° was chosen, but it should be possible to use finer steps. It is believed that a resolution of 0.25° should be feasible, resulting in a possible mean error of less than 0.125°.

The strength of the pattern recognition approach lies in the use of discrete output values. Even though this approach limits output resolution, it serves the purpose of making output decisions from the network more robust. This robustness eliminates misclassifications, and by doing so, improves system performance. The relatively large number of output nodes limits training speed, but also greatly contributes to network classification performance. In this paper, it was shown that in more than 99% of the samples, DOA is determined with an average error better than 0.5°. The very few misclassifications for the correctly trained system should be easy to remove through spatial filtering in later stages of data processing.

Once the network is trained, it can easily be applied to classify DOA in real-time. The training of the network can be relatively time consuming (~10 minutes), but applying it to data is almost instantaneous. A possible future approach would be to implement the network on an FPGA in a system operating on data in near real-time.

The full duration of training the system was less than 10 minutes, and it is clear that performance is consistent for at least several hours from training. It was shown that performance was severely degraded when the trained system was used to estimate DOA 24 hours or more after it was trained. The effects of this can probably be limited if an MZM bias control circuit is added to the design, since most of these errors are believed to stem from MZM bias point drift.

The results shown in Figure 73 to Figure 77 demonstrate that the MLP pattern recognition system is insensitive to how the channels are phase-aligned before training. This is a very important advantage in an interferometric DF system, since this means that no front-end calibration of phase is necessary and the phase shifters could be left out of future designs. All compensation for phase unbalance in the receiving system is performed in the training of the MLP, reducing complexity and cost in future systems.

To fully determine true DOA accuracy, testing should be performed with a pedestal control system providing true DOA readings. These errors do not substantially affect the performance measurement for the $1°$ resolution system tested here, but will be necessary if better resolution systems are developed and tested.

In this investigation, we used a single, continuous signal with fixed frequency. It should be possible to make the system wide-band capable by adding a fourth input to the network representing signal frequency. This should make the system capable of determining DOA over a wide range of frequencies but might increase training complexity.

For future work, different antenna arrays should be investigated to determine optimal antenna element spacing.

APPENDIX. OVERVIEW OF ROBUST SYMMETRICAL PROCESSING

Symmetrical folding waveforms are fundamental parts of engineering sciences, where sinusoidal waves are among the more commonly recognized examples. Electromagnetic transmission at RF consists of sinusoidal waveforms, either modulated or un-modulated. Performance of electronic warfare (EW) systems is strongly dependent on the systems' ability to detect these waveforms and extract information from them.

Symmetrical number systems are powerful for analyzing folding waveforms. Several forms of symmetrical number systems have been formulated to meet various analyzing needs and research questions, including the symmetric number system (SNS), the optimum symmetric number system (OSNS), and the robust symmetrical number system (RSNS).

The RSNS is a number system based on modules with $N \geq 2$ sequences of integers. Each of these sequences is formed as [43].

$$\{x'_m\} = [0, 1, 2, ..., m-1, m, m-1, ..., 2, 1]$$ (13)

The N-sequence RSNS is formed through repeating each term in Equation 13, yielding the integers in a folding period to be

$$\{x_m\} = [0, ..., 0, 1, ..., 1, ..., m-1, ..., m-1, m, ..., m, m-1, ..., m-1, ..., 1, ..., 1]$$ (14)

The resulting sequence has a period of $P_m = 2Nm$ [44], and to form the number system, each sequence is shifted either left or right by shift values $s_i = i - 1$ where $i \in \{1, 2, ..., N\}$. These shift values must meet the criteria of together forming a complete modulo N residue system. The incremental shift of each sequence gives the system an integer Gray code property, a characteristic that makes it unique when compared to the SNS and OSNS [43]. A three-sequence RSNS for moduli $m_i = \{3, 4, 5\}$ is shown in Figure 78.

Figure 78.   Plot of Three-Sequence RSNS for Moduli $m_i = \{3,4,5\}$
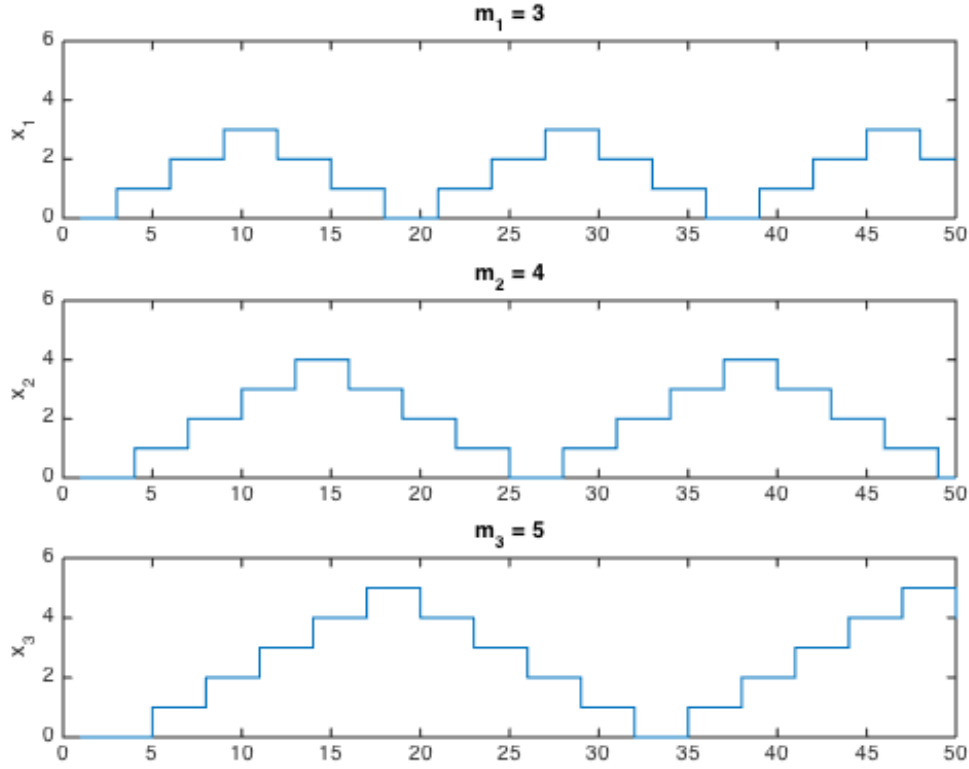
The full N-sequence RSNS is periodic and has a fundamental period calculated after [45] as

$$P_f = 2N\prod_{i=1}^{N} m_i \qquad (15)$$

Ambiguous combinations of the sequence values exist in several positions of the fundamental period. These ambiguities limit the maximum unambiguous range $\widehat{M}_{RSNS}$, *the system dynamic range,* of the RSNS. Several closed-form expressions for the size and location of the dynamic range have been formulated in [44] and [45]–[47]. For a system where $N = 3$ and $m_i = \{m-1, m, m+1\}$ with m even and $m > 3$, the closed form expression is

$$\widehat{M}_{RSNS} = \frac{3}{2}m^2 + \frac{15}{2}m + 7 \qquad (16)$$

The dynamic range can exist in one or several places of the fundamental period and its location for a system with $m_i = \{7,8,9\}$ was computed by [23] after [44] to start at 733 and end at 865 with a total length of 133. The RSNS sequence used in [23] and [22] is shown in Figure 79.

Figure 79.　　Example of RSNS System Dynamic Range for $m_i = \{7,8,9\}$
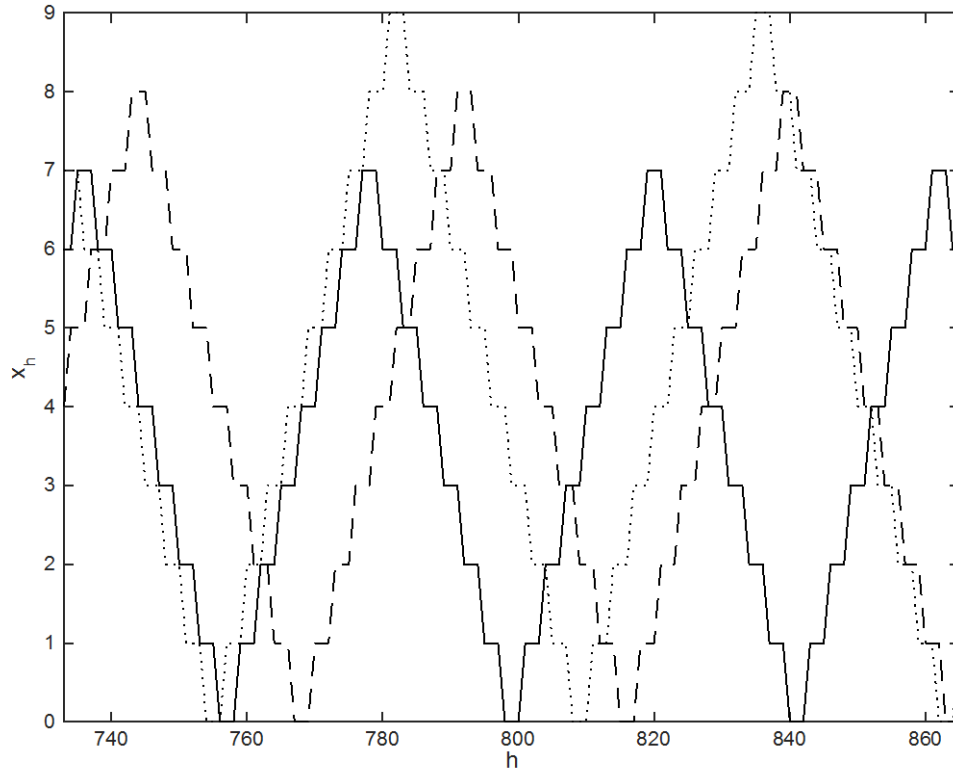
THIS PAGE INTENTIONALLY LEFT BLANK

LIST OF REFERENCES

[1]   P. Hajiani et al., "Accuracy in wideband direction of arrival system," in *4th Int. Symp. Electromagnetic Compatibility Proc.,* Qingdao, China, 2007, pp. 394–397.

[2]   G. V. Borgiotti, "Maximum theoretical angular accuracy of planar and linear arrays of sensors," *IEEE Trans. on Aerosp. Electron. Syst.* vol. AES-13, no. 2, pp. 208–216, 1977.

[3]   X. Yang and C. Zhan-zhong, "Two-dimensional circular array real-time phase interferometer algorithm and its correction," in *Int. Conf. on Image Signal Process. (CISP),* Tianjin, China, 2009, pp. 1–5.

[4]   L. Schmieder et al., "Signal direction finding for low complexity radar," in *Int. Waveform Diversity and Design Conf.,* Kissimmee, FL, 2009, pp. 8–12.

[5]   H.-W. Wei and Y.-G. Shi, "Performance analysis and comparison of correlative interferometers for direction finding," in *IEEE 10th Int. Conf. Signal Process.*, Beijing, China, 2010, pp. 393–396.

[6]   C.-S. Park and D.-Y. Kim, "The fast correlative interferometer direction finder using I/Q demodulator," in *Asia-Pacific Conf. on Commun.*, Busan, Korea, 2006, pp. 1–5.

[7]   X.-P. Deng et al., "Passive location method and accuracy analysis with phase difference rate measurements," *IEEE Proc. Radar, Sonar Navigation*, vol. 148, no. 5, pp. 302–307, Oct. 2001.

[8]   R. Shar, "Simulation of polarizer impact on circular interferometer performance," in *11th IEEE Int. Conf. Computational Sci. Eng.*, Sao Paulo, Brazil, 2008, pp. 334–339.

[9]   S. Wang et al., "An exact formula for the probability density of the phase error of a digital interferometer," in *Communications 25th Biennial Symp. on Commun. (QBSC)*, Kingston, Canada, 2010, pp. 201–204.

[10]   S. Wang et al., "Probability density of the phase error of a digital interferometer with overlapped FFT processing," in *53rd IEEE Int. Midwest Symp. on Circuits Syst. (MWSCAS)*, Seattle, WA, 2010, pp. 849–852.

[11]   R. L. Musselman and J. D. Norgard, "Frequency invariant interferometry," in *IEEE Antennas and Propagation Soc. Int. Symp., 1992,* Chicago, IL, 1992, pp. 2101–2104.

[12]   K. W. Kwai et al., "Robust symmetrical number system direction finding arrays with virtual spacing," in *IEEE Antennas and Propagation Soc. Int. Symp.*, San Diego, CA, 2008, pp. 1–4.

[13]   M. D. Blech et al., "2-dimensional ultra-wideband monopulse based direction finding," in *IEEE MTT-S Int. Microwave Symposium Digest*, Atlanta, GA, 2008, pp. 1159–1162.

[14]   Y.-W. Wu et al., "Direction of arrival estimation via extended phase interferometry," *IEEE Trans. on Aerosp. and Electron. Syst.*, vol. 31, no. 1, pp. 375–381, 1995.

[15]   E. M. Warrington and T. B. Jones, "Measurements of the direction of arrival of HF sky wave signals and single site location using a seven element wide aperture (294 m) interferometer array," *IEEE Proc. on Microwaves, Antennas and Propagation*, vol. 138, no. 2, pp. 121–130, 1991.

[16]   B. Friedlander and A. J. Weiss, "Direction finding for wide-band signals using an interpolated array," *IEEE Trans. on Signal Process.*, vol. 41, no. 4, pp. 1618–1634, 1993.

[17]   H. L. Levitt et al., "Superresolution precision direction-finding techniques and measurements," *SPIE Proc. Transition Optical Processors into Systems*, vol. 2489, June 1995.

[18]   Z. Stankovic et al., "Antenna array signal processing with neural networks for direction of arrival estimation," in *11th Int. Conf. Telecommun. in Modern Satellite, Cable and Broadcast. Services (TELSIKS)*, Nis, Serbia, 2013, pp. 526–529.

[19]   P. C. J. Hill and P. D. Wells, "Antenna beamforming for EW using adaptive layered networks," in *IEEE Colloquium Signal Process. Electron. Warfare*, London, England, 1994, pp. 2/1–2/5.

[20]   A. Faye et al., "LVQ Based DOA Estimation," in *Fifth Int. Conf. Computational Intell., Commun. Systems and Networks (CICSyN),* Madrid, Spain, 2013, pp. 245–250.

[21]   E. Alpaydin, *Introduction to Machine Learning*, 3rd ed. Cambridge, MA: MIT Press, 2014.

[22]   T. W. Tedesso et al., "Wideband direction finding using a photonic robust symmetrical number system technique," *Optical Engineering Journal,* vol. 53, no. 11, pp. 1–13, Nov. 2014.

[23]   H. W. Lim, "FPGA implementation of robust symmetrical number system in high-speed folding analog-to-digital converters," M.S. thesis, Dept. Elect. Compu. Eng. Naval Postgraduate School, Monterey, CA, Dec. 2010.

[24]   L. Mach, "Über einen interferenzrefraktor" (On an interference refractor), *Instrumentenkunde* (Instrument tuition), vol. 12, pp. 89–93, 1892.

[25]   L. Zehnder, "Ein neuer Interferenzrefraktor" (A new interference refractor), *Zeitschrift für Instrumentenkunde* (Journal for instrument tuition), pp. 276–285, 1891.

[26]   A. Chen and E. J. Murphy, *Broadband Optical Modulators; Science, Technology, and Applications*. Boca Raton, FL: CRC Press, 2012.

[27]   P. J. Winzer and R.-J. Essiambre, "Advanced optical modulation formats," *Proc. IEEE*, vol. 94, no. 5, pp. 952–985, May 2006.

[28]   JDS Uniphase Corporation. (2008, April). JDS Uniphase. [Online] . Available: http://www.jdsu.com/noindexliterature/biascontrolextmodddt_an_cc_ae.pdf

[29]   Y. Fu et al., "Mach-Zehnder: A review of bias control techniques for Mach-Zender modulators in photonic analog links," *IEEE Microwave Magazine,* vol. 14, issue 7, pp. 102–107, Nov./Dec. 2013.

[30]   W. L. Stutzman and G. A. Thiele, *Antenna Theory and Design*, 3rd ed. Hoboken, NJ: John Wiley & Sons, 2012.

[31]   B. S. Blanchard, *System Engineering Management*, 4th ed. Hoboken, NJ: John Wiley & Sons, 2008.

[32]   P. E. Pace et al., "High-resolution phase sampled interferometry using symmetrical number systems," *IEEE Trans. on Antennas and Propag.*, no. 49, pp. 1411–1423, Oct. 2001.

[33] W. D. Stanley and J. M. Jeffords, *Electronic Communications: Principles and Systems*. Clifton Park, NY: Delmar, 2006.

[34] Conductivity and resistivity values for aluminum & alloys. (2002, March). The Collaboration for NDT Education, NDT Education Resource Center, Iowa State University. [Online] . Available: https://www.nde-ed.org/GeneralResources/MaterialProperties/ET/Conductivity_Al.pdf

[35] Conductivity and resistivity values for iron & alloys. (2002, March). The Collaboration for NDT Education, NDT Education Resource Center, Iowa State University. [Online] . Available: https://www.nde-ed.org/GeneralResources/MaterialProperties/ET/Conductivity_Iron.pdf

[36] LNA series 2200–3200MHz low noise amplifier. (2006, Jan.) RF BAY, Inc. [Online]. Available: http://rfbayinc.com/products_pdf/product_109.pdf

[37] Coaxial cable 141 model series 141–3SM+. (n.d.). Mini-Circuits. [Online] . Available: http://www.minicircuits.com/pdfs/141-3SM+.pdf. Accessed Jun. 25, 2015.

[38] Coaxial voltage variable attenuator ZX73-2500+. (n.d.). Mini-Circuits. [Online] . Available: http://www.minicircuits.com/pdfs/ZX73-2500+.pdf. Accessed Jun. 25, 2015.

[39] Surface mount phase shifter SPHSA-242+. (n.d.). Mini-Circuits. [Online] . Available: http://www.minicircuits.com/pdfs/SPHSA-242+.pdf. Accessed Jun. 25, 2015.

[40] DC pass power splitter/combiner ZB4PD-462W+. (n.d.) Mini-Circuits. [Online] . Available: http://www.minicircuits.com/pdfs/ZB4PD-462W+.pdf. Accessed Jun. 25, 2015.

[41] LPA series DC-4000MHz RF amplifier. (n.d.) RF Bay, Inc. [Online] . Available: http://rfbayinc.com/products_pdf/product_140.pdf. Accessed Jun. 25, 2015.

[42] Coaxial bias-tee ZFBT-352-FT+. (n.d.) Mini-Circuits. [Online] . Available: http://www.minicircuits.com/pdfs/ZFBT-352-FT+.pdf. Accessed Jun. 25, 2015.

[43]   P. E. Pace et al., "Extended closed-form expressions for the robust symmetrical number system dynamic range and an efficient algorithm for its computation," *IEEE Trans. Inf. Theory*, vol. 60, no. 3, pp. 1742–1752, 2014.

[44]   B. L. Luke and P. E. Pace, "N-sequence RSNS ambiguity analysis," *IEEE Trans. on Infor. Theory,* vol. 53, no. 5, pp. 1759–1766, May 2007.

[45]   P. E. Pace et al., "A folding ADC preprocessing architecture employing a robust symmetrical number system with Gray-code properties," *IEEE Trans. on Circuits Syst. II, Analog and Digital Signal Process.*, vol. 47, no. 5, May 2000.

[46]   P. E. Pace et al., "High-resolution phase sampled interferometry using symmetrical number systems," *IEEE Trans. on Antennas and Propag.*, vol. 49, pp. 1411–1423, Oct. 2001.

[47]   P. E. Pace and D. D. Styer, "High-resolution encoding process for an integrated optical analog-to-digital converter," *Optical Engineering Journal*, pp. 2638–2645, Aug. 1994.

THIS PAGE INTENTIONALLY LEFT BLANK

INITIAL DISTRIBUTION LIST

1.   Defense Technical Information Center
        Ft. Belvoir, Virginia

2.   Dudley Knox Library
        Naval Postgraduate School
        Monterey, California